Fabrication and Characterization

of Metallic Cavity Nanolasers

by

Kang Ding

A Dissertation Presented in Partial Fulfillment
of the Requirements for the Degree
Doctor of Philosophy

Approved April 2014 by the
Graduate Supervisory Committee:

Cun-Zheng Ning, Chair
Hongbin Yu
Joseph Palais
Yong-Hang Zhang

ARIZONA STATE UNIVERSITY

May 2014

ABSTRACT

Nanolasers represents the research frontier in both the areas of photonics and nanotechnology for its interesting properties in low dimension physics, its appealing prospects in integrated photonics, and other on-chip applications. In this thesis, I present my research work on fabrication and characterization of a new type of nanolasers: metallic cavity nanolasers.

The last ten years witnessed a dramatic paradigm shift from pure dielectric cavity to metallic cavity in the research of nanolasers. By using low loss metals such as silver, which is highly reflective at near infrared, light can be confined in an ultra small cavity or waveguide with sub-wavelength dimensions, thus enabling sub-wavelength cavity lasers. Based on this idea, I fabricated two different kinds of metallic cavity nanolasers with rectangular and circular geometries with InGaAs as the gain material and silver as the metallic shell. The lasing wavelength is around 1.55 μm, intended for optical communication applications. Continuous wave (CW) lasing at cryogenic temperature under current injection was achieved on devices with a deep sub-wavelength physical cavity volume smaller than 0.2 λ^3. Improving device fabrication process is one of the main challenges in the development of metallic cavity nanolasers due to its ultra-small size. With improved fabrication process and device design, CW lasing at room temperature was demonstrated as well on a sub-wavelength rectangular device with a physical cavity volume of 0.67 λ^3. Experiments verified that a small circular nanolasers supporting TE_{01} mode can generate an azimuthal polarized laser beam, providing a compact such source under electrical injection. Sources with such polarizations could have many special applications. Study of digital modulation of circular nanolasers

showed that laser noise is an important factor that will affect the data rate of the nanolaser when used as the light source in optical interconnects.

For future development, improving device fabrication processes is required to improve device performance. In addition, techniques need to be developed to realize nanolaser/Si waveguide integration. In essence, resolving these two critical issues will finally pave the way for these nanolasers to be used in various practical applications.

DEDICATION

To my parents

ACKNOWLEDGMENTS

I wish to use this chance to express my gratitude to everyone who helped and encouraged me to perform a job for my PhD research.

I must first thank my advisor Dr. Cun-Zheng Ning, who generously supported my entire PhD study and offered me this great opportunity to be part of researches in the nanophotonics group, who guides and inspires me with his broad and rich knowledge, intensive passion to the scientific research.

I should thank Dr. Martin Hill who constantly offered help, advice and collaboration in the metallic cavity nanolaser project since 2008. Dr. Hill hosted my twice visits to TU/e and assisted me to use the advanced fabrication facility there. Thanks to Dr. Hill's collaboration, we achieved great success in the nanolaser project and have the one of the best results in this area.

I also thank Dr. Hua Wang and Dr. Ruibin Liu who trained me to do fabrication and laser measurement when I first came to ASU. Those skills I learned from them have been of great use for my research.

All the group members in Dr. Ning’s group, it is been great pleasure working with you all. Thank you for the help you have kindly offered.

Leijun, Zhicheng, Fan and Minghua, thank you for your hard work in the optical lab to measure the small lasers and sorry for all the troubles I have made there.

Debin, thank you for the useful discussion and help on all the theoretical and simulation work.

At last I will my parents. I could not be close to what I have achieved today without their love and support.

TABLE OF CONTENTS

Page

LIST OF TABLES ... viii
LIST OF FIGURES ... ix
CHAPTER
1 INTRODUCTION ... 1
1.1 Metals in optics ... 1
1.2 A brief history of metallic cavity nanolaser ... 2
1.3 Metallic waveguides and cavities ... 5
1.3.1 Waveguide confinement ... 5
1.3.2 Cavity Q factor ... 8
1.3.3 Cross talk ... 9
1.3.4 Heat dissipation ... 10
1.4 Optical process in nano-cavities ... 12
1.5 Objective and methods ... 13
1.6 Structure of this thesis ... 17
2 METALLIC WAVEGUIDES ... 19
2.1 Introduction ... 19
2.2 Optical properties of metals ... 19
2.3 Surface Plasmon Polariton Waveguides ... 21
2.3.1 Metal/semiconductor waveguide ... 21
2.3.2 Metal-semiconductor-air waveguide ... 28
2.3.3 Metal-semiconductor-metal waveguide ... 32
2.4 TE modes in Metal-Semiconductor waveguides ... 36
2.5 Effective waveguide width ... 41
2.6 Confinement factor and gain compensation of various waveguides ... 43
2.7 Summary ... 45
3 PROCESSING ... 47
3.1 Introduction ... 47
3.2 Device structure ... 47
3.3 Wafer design ... 48
3.4 Device fabrication ... 49
3.4.1 Wafer preparation: Fig. 3.2a-c ... 53
3.4.2 Device definition: Fig. 3.2d-e ... 53

CHAPTER Page

3.4.3 Etching and cleaning: Fig. 3.2f-i ... 54
3.4.4 Silver deposition: Fig. 3.2j-q ... 56
3.4.5 Contact formation: Fig. 3.2 r-u ... 58
3.5 Packaging ... 58
3.6 Critical steps in nanolaser fabrication ... 60
3.6.1 EBL ... 61
3.6.2 Pillar etching ... 62
3.6.3 Surface cleaning and passivation ... 65
3.6.4 Silver deposition ... 68
3.7 Summary ... 72
4 RECTANGULAR NANOLASERS ... 73
4.1 Introduction ... 73
4.2 Waveguiding in MISIM structure ... 73
4.3 Metallic nanocavity based on MISIM waveguide ... 78
4.4 Device measurement setup ... 79
4.5 Characterization for devices based on MISIM waveguides ... 80
4.5.1 Mode and polarization ... 81
4.5.2 Multimode lasing ... 83
4.5.3 Small lasers ... 86
4.6 Room temperature operation ... 90
4.6.1 Strategy to improve operation temperature ... 90
4.6.2 Endeavors to RT CW Operation ... 92
4.6.3 Record performance of RT CW nanolaser ... 94
4.7 Summary ... 99
5 CIRCULAR NANOLASERS ... 101
5.1 Introduction ... 101
5.2 Modes in circular metallic nanocavity ... 101
5.3 First generation with thick SiN layer ... 104
5.3.1 Optimizing SiN thickness ... 104
5.3.2 Azimuthal polarization of TE_{01} mode device ... 106
5.3.3 Characterization of circular nanolaser ... 108
5.4 Second generation with thin SiN ... 112
5.5 Summary ... 116
6 NANOLASER MODULATION ... 118
6.1 Introduction ... 118

CHAPTER Page
6.2 Spontaneous and simulated emission in a nanocavity in near infrared 118
6.3 Models 122
6.3.1 Rate Equation model 122
6.3.2 Nanolaser model 123
6.4 Laser modulation 126
6.4.1 Analog and digital modulation, and the energy consumption 126
6.4.2 Calculation results 131
6.5 Summary and discussion 134
7 SUMMARY AND DISCUSSION 136
7.1 Introduction 136
7.2 Advantages of metallic cavity nanolasers 136
7.3 Key results in this thesis 136
7.4 Fabrication challenges 137
7.5 Future research and nanolaser-waveguide integration 138
APPENDIX 141
REFERENCES 143

LIST OF TABLES

Table Page

1.1 Fitting parameters for silver dielectric constant in the MEEP.. 17

3.1 Stacking layer structure of the wafer for nanolaser fabrication 49

4.1 Definitions of parameters in rate equations 89

5.1 Mode resonance wavelength and Q factor for a circular nanolaser with 540nm radius from simulation and measurement. 114

LIST OF FIGURES

Figure Page

1.1 (a) Electric field of TE_0 mode at 1.55 μm in the 2D infinite air-dielectric (ε=12, ε is relative dielectric constant)/air slab waveguide. (b) Electric field of TM_0 mode at 1.55 μm in the 2D infinite silver-dielectric (ε=12)-silver slab waveguide. (c) Confinement factor of these two kinds of waveguide as a function of waveguide core width 7

1.2 (a) Electric field from simulation of whispering gallery mode in microdisk cavities. (b) Electric field from simulation of whispering gallery mode in metallic-coated microdisk cavities. m is the folds of rotational symmetry............9

1.3 Figure 1.3 Electric field (Ez) of two R = 340 nm metallic disks (black solid line) and two R = 350 nm dielectric disks (red dashed line), along the line connecting the centers of the two cavities. The pink dash-dotted line shows the superposition of the electric field of the two dielectric disks. The separation between two disk centers is 1.3 μm. Blue vertical lines (solid lines for metallic disk and dashed lines for dielectric disk) mark the boundaries of disk.. 10

1.4 Schematic of (a) cylindrical metallic cavity nanolaser and (b) dielectric nanolaser under this thermal study. (c) Output power (black lines) and active region temperature (red lines) calculated by rate equations for these

Figure Page

two lasers (solid lines for metallic cavity nanolasers, and dashed lines for dielectric cavity nanolaser)... 11

1.5 Silver dielectric constant from Johnson and Christy26 and its Lorentzian fitting result. (a) Real part and (b) Imaginary par. 16

1.6 Figure 1.6 Silver dielectric constant from Dold et al37 and Winsemiu et al38 and the Lorentzian fitting result for a combination of these two sets of data. (a) Real part and (b) Imaginary par................ 17

2.1 Silver dielectric constant from Johnson and Christy26 (○) and Drude model (−) fitting result. (a) Real part and (b) Imaginary part..............................21

2.2 Schematic of a single metal-semiconductor interface waveguide supporting a SP wave propagating in Z direction along the interface of a metal and a semiconductor. Red arrows show the electric field. +, − signs show the charge density oscillations in metal................. 22

2.3 Propagation constant of SPP mode in a single silver-dielectric waveguide with different dielectric constants of dielectrics (a) real part and (c) imaginary part. (b) and (d) show the corresponding mode effective refractive index and propagation loss..25

2.4 (a) Electric field (Ex) and (b) its energy density of SPP mode in a silver-semiconductor waveguide (εs = 12) of different wavelengths. (c)

Effective mode width and energy confinement factor of this mode at different wavelengths. The outer left Y axis shows the effective mode width in terms of wavelength in semiconductor (λ/n_r)......................................26

2.5 Schematic of a SPP wave propagating in a MSA waveguide 28

2.6 Propagation constant of SPP mode in a silver-semiconductor (h = 100 nm, εs = 12) -air waveguide. (a) Real part (b) Imaginary part. Solid lines are from perturbation calculation; hollow circles are from COMSOL simulation without any approximation...30

2.7 (a) Electric field (Ex) and (b) its energy density of SPP modes at different wavelengths in a silver-semiconductor silver-semiconductor (h = 100 nm, εs = 12)-air waveguide. (c) Energy confinement factor of this waveguide as a function of wavelength. 31

2.8 Schematic of (a) even and (b) odd SPP mode in a metal-semiconductor-metal waveguide. 32

2.9 (a) (c) Real and (b) (d) imaginary part of propagation constant of SPP mode in a silver-semiconductor-silver waveguide. Solid lines are from perturbation calculation, and hollow circles are from COMSOL simulation. 35

Figure Page

2.10 Electric field (Ex) and its energy density of SPP modes at different wavelengths in a silver-semiconductor (d = 50 nm, εs = 12) silver waveguide. (a) (b) Symmetric mode and (c) (d) Anti-symmetric mode.............36

2.11 (a) Real and (b) imaginary part of propagation constant of TEz mode in a silver-semiconductor (h = 200 nm, εs = 12)-air waveguide. Solid lines are from perturbation calculation. Hollow circles are from COMSOL simulation...38

2.12 (a) Real and (b) imaginary part of propagation constant of TEz mode in a silver-semiconductor (d = 100 nm, εs = 12)-silver waveguide. Solid lines are from perturbation calculation, hollow circles are from COMSOL simulation...40

2.13 Electric field (Ey) of TEz modes at different wavelengths in (a) MSA and (b) MSM waveguide with 200 nm semiconductor layer. 40

2.14 (a) Effective mode width calculated by (2.17) for the SPP mode in a MS waveguide and MSM waveguide with 200 nm thick semiconductor core layer. (b) Effective waveguide width calculated by (2.39). Solid lines are for SPP mode in MS, MSM with a 100 nm semiconductor layer (MSM100) and a 200 nm semiconductor layer (MSM200). Dashed lines are for SPP mode in MSA with a 100 nm semiconductor layer (MSA100) and a 200

Figure Page

nm semiconductor layer (MSA200). Circled lines are for TE mode in MSM (MSM 200TE) and MSA (MSA 200TE) with a 200 nm semiconductor layer. 42

2.15 (a) Propagation loss, (b) confinement factor in semiconductor, and (c) waveguide threshold material gain for MS, 100 nm MSM, 100 nm MSA, 200 nm MSM, 200 nm MSA waveguide. Legends here are the same as in Fig. 2.14. 45

3.1 Schematic structure of metallic cavity nanolasers. Semiconductor pillar with a (a) rectangular or (b) circular cross section is encapsulated in silver to form a metallic cavity. 48

3.2 Device fabrication procedures. 50

3.3 HPR-504/HSQ pattern fabricated after EBL exposure, development and RIE etching. 54

3.4 SEM image of a cleaned InP/InGaAs/InP pillar. 55

3.5 SEM image of a pillar with SiN coated on the side and top contact metal. 57

3.6 (a) Schematic of silver deposition. The wafer holder can be rotated in two directions freely in order to deposit silver uniformly. (b) SEM image of a pillar coated with silver after annealing. The silver grain size can be up to 1 μm. 58

Figure Page

3.7 (a) Schematic of a sample bar containing 5 individual devices. (b) A sample bar flipped over and mounted to ceramic package by a copper block and gold wires. 59

3.8 Picture of a device bar mounted on a ceramic package by copper block and gold wires. 60

3.9 400nm wide strip pattern made by EBL with (a) PMMA resist and metal lift-off and (b) HPR-504/HSQ bilayer resist and RIE 62

3.10 (a) Schematic of a device with tilted sidewall. (b) Cavity Q (TE01 mode in a circular device with radius of 200nm, Johnson and Christy silver used) as a function of sidewall angle θ. 63

3.11 Optical field (|E|2) of TE01 mode in cavities with (a) straight sidewall and (b) tilted sidewall 64

3.12 SEM image of an InP/InGaAs/InP pillar etched by ICP RIE with optimized processing parameters....64

3.13 (a) InP/InGaAs/InP grating structure used in PL measurement and (b) its SEM image....67

3.14 PL intensity of test grating structure after different process steps. 1) Un-etched. 2) Dry etched. 3) O2 plasma treated. 4) Dilute H3PO4 treated. 5) SiN deposited on surface. 6) Thermally annealed. 68

Figure Page

3.15 SEM images of InP/InGaAs/InP pillar after cleaning (a) under room light, (b) in dark. 68

3.16 Measured dielectric constant of silver: (a) real part and (b) imaginary part from different sources: Dold and Mecke, Winsemius et al, Johnson and Christy, Weber 71

3.17 Device cavity Q obtained in the simulation using different silver dielectric constants. Cavity radius is set to 230 nm, supporting TE01 mode. Hollow square □ is inversed electron damping rate γ for different silver data extracted by fitting with Drude model 71

4.1 Structure of a rectangular metallic cavity nanolaser. Dimensions of the rectangular pillar, width (W, in X direction), height (H, in Y direction) and length (L, in Z direction), are indicated. 74

4.2 Schmetic of metal-dielectric-semiconductor-dielectric-metal (MISIM) waveguide in XY plane. 75

4.3 Mode |E| patterns of **(a)** TE-like mode, E_y dominant and **(b)** TM-like mode or plasmonic gap mode, E_x dominant. 76

4.4 (a) Mode effective index and propagation loss for TE-like (black symbols) and TM-like (red symbols) modes in MISIM waveguide at 1.55μm wavelength plotted as a function of waveguide core width. TE-like mode

has a cut-off width below the diffraction limit ($\lambda/2n_r$) while TM-like mode shows no cut-off. (b) Confinement factor defined by (1.1) and waveguide threshold material gain defined by (2.41) for this two modes as a function of waveguide core width..77

4.5 Standing wave in a metallic nanocavity based on MISIM waveguide. $|E|^2$ is plotted...79

4.6 Schematic of the optical measurement setup for nanolaser measurement 80

4.7 (a) Multimode observed in a device with physical volume of 280 nm (W) $\times$ 6 μm (L) $\times$ 1.53 μm (H) at 100 K before threshold. (b) Polarization result for TE1 mode and TM2 mode. TE1 mode is linearly polarized about 20° away for device's length direction (90°) and TM2 mode is linearly polarized perpendicular to device length direction (0°). 82

4.8 (a) Lasing spectrum of this device at 429 μA. (b) L-I curve for the laisng TE1 mode and a TM1+TM2. The TE1 mode had a threshold around 90 μA while TM1+TM2 saturated after threshold. 83

4.9 Spectra of a device with physical volume of 280 nm (W) $\times$ 6 μm (L) $\times$ 1.53 μm (H) at 220 K under different injection currents. Double mode lasing is observed. 84

Figure Page

4.10 (a) Spectra for this device at a low current 1186 μA below the threshold of final dominant lasing mode M2. M1-M3, M5 are equally spaced longitudinal mode. (b) L-I curve for mode M2 and M3. M2 becomes the final lasing mode after the threshold current at 1650 μA. Mode M3 also shows lower a lasing threshold around 1200 μA but saturates afterwards, giving ways to mode M2. 84

4.11 Group index calculated for M1-M3 and M5 using (4.2) 85

4.12 Dispersion of the TE-like mode in a MISIM waveguide with a 280 nm core width and 15 nm SiN layer with an InGaAs dispersion shown in (4.3). 86

4.13 (a) Lasing spectra of a device with physical volume of 400 nm (W) $\times$900 nm (L) $\times$1.5 μm (H) at 100 K under different injection currents. (b) L-I curve shows a lasing threshold around 80 μA. The spontaneous saturates after threshold. Linewidth narrows from 5.8 nm when below threshold to 0.6 nm when above threshold. 87

4.14 Blue shift of lasing mode as current increases 88

4.15 Cavity quality factors of 2D rectangular Silver-SiN-InGaAs cavities of different length/width ratios but same total area of 0.8 λ^2. Inset is the simulation geometry. 92

Figure Page

4.16 Spectra of two devices under similar current injection at room temperature. (a) 280 nm (W) $\times 6$ μm (L) $\times 1.53$ μm (H), current is 2964 μA. (b) 1.1 μm (W) $\times 2.1$ μm (L) $\times 1.5$ μm (H), current is 2276 μA. 94

4.17 Light intensity and FWHM as functions of DC current at 293K. Inset: spectrum with arrows and numbers indicating positions where light intensity is taken: lasing mode (● circles, 1), nonlasing mode (♦ diamonds, 2), and spontaneous emission at 1460 nm (▲ triangles, 3). The threshold is estimated ~1000 μA. 94

4.18 CW Laser characteristics at room temperature of a device with physical volume of 1.15 μm (W) $\times 1.39$ μm (L) $\times 1.7$ μm (H). **(a)** L-I and FWHM-I curve at 294K under DC current injection of the laser. ■: integrated lasing mode intensity; ●: integrated spontaneous emission intensity. **(b)** Spectra (offset for clarity) of this device at different currents. 96

4.19 (a) $|E|^2$ patterns of E_{106} mode. (b) Polarization resolved measurement result, where Z-direction corresponds to 0 and 180 degrees. 97

4.20 L-I curve plotted on a log-log scale and its slope from experimental result (red solid circle ●) and from rate equation (RE) calculation (solid line), with slopes given for three regions 99

Figure Page

5.1 Structure of a rectangular metallic cavity nanolaser. Dimensions of the rectangular pillar, radius (R), height (H, in Z direction), are labeled. 102

5.2 Mode optical field $|E|^2$ of (a) HE_{11} mode, R = 100 nm (b) TM_{01} mode, R = 2145 nm and (c) TE_{01} mode R = 240 nm. The bottom part of the each figure shows the $|E|^2$ pattern at the cross section plane at the center of InGaAs gain layer. 103

5.3 Resonance wavelengths of HE_{11}, TM_{01} and TE_{01} modes in a metallic cavity nanolaser as a function of semiconductor pillar radius. Thickness of SiN layer is 30 nm. Shaded gray region indicates roughly the gain bandwidth of InGaAs material. 104

5.4 Cavity Q factor and energy confinement factor (upper panel) and Γ_EQ product (lower panel) as a function of SiN thickness for the TE_{01} mode. In FDTD simulation, semiconductor radius is modified accordingly to keep the resonance wavelength around 1.55 μm. 106

5.5 (a) $|E|^2$ field of TE_{01} mode in Z-r plane. Cavity boundary is marked by white dashed rectangle. (b) Azimuthal component of the electric field of TE_{01} mode beneath the cavity bottom aperture at the vertical location in r-φ plane, indicated by the white long dashed line in (a). 107

5.6 Schmetic of the optical setup for nanolaser measurement 109

Figure Page

5.7 Lasing characteristics of a circular nanolaser with pillar radius at 175 nm, total cavity volume of 0.146 λ^3 (λ = 1416 nm), including SiN layer. (a) Lasing spectrum. Inset is the lasing spectra under different currents (μA). (b) Integrated intensity of lasing mode (red circle) and spontaneous emission (black square) of this device as a function of injection current. (c) Linear dependence of resonance wavelength on diameter from 1.37 μm to 1.53 μm. The slope is 2.7..109

5.8 (a) Laser output images taken by a NIR camera behind a linear polarizer in four different orientations, as indicated by the white arrow. The dark line splitting the image along the polarizer direction confirms the azimuthal polarization of the laser output. (b) Schematic illustration of the dark line in (a). Electric field (red lines) at the circle axis (the shaded double arrow) is be blocked by the polarizer, leaving a dark line in the beam image...............110

5.9 CW lasing spectrum from a device with a radius of 255 nm supporting TM_{02} mode under DC current injection at 200 K. The total volume of this device is 0.283 λ^3 (λ = 1.342 μm)..112

5.10 Emission spectrum from a device with radius of 540 nm at 200K under DC current injection 113

Figure Page

5.11 Mode patterns $|E|^2$ of a circular device with a radius at 540 nm and SIN thickness at 30 nm **(a)** TM_{51} mode **(b)** HE13 mode and **(c)** EH_{22}. The bottom part of the each figure shows the $|E|^2$ pattern at the cross section plane at the center of InGaAs gain layer. 114

5.12 Linear dependence of resonance wavelength on diameter in large circular nanolasers 115

5.13 L-I curve of a device with radius of 700nm at room temperature (296K) under pulse current injection (30ns pulse width/1MHz repetition rate). The current is normalized. The inset shows the spectra at different currents of 2.13mA (black), 3.07mA (red) and 3.83mA (blue). 116

6.1 (a) Schematic of the high Q cylindrical metallic cavity nanolaser studied in this paper. (b) Q factors (black ■) and energy confinement factor (red ●) of TE_{01}, TE_{02}, TE_{03}, and TE_{04} mode. 124

6.2 (a) Calculated L-I curve and linewidth for a 460 nm diameter laser. (b) Spectrum of spontaneous emission coupled to lasing mode ($R_{sp,m}$) in this laser under a 25 μA injection current and spontaneous emission in bulk InGaAs ($R_{sp,fs0}$) with the same carrier density. (c) Calculated threshold and threshold current density and (d) spontaneous emission factor β for TE_{0x} mode. 126

Figure Page

6.3 (a) Calculation example of photon number variation of a semiconductor laser under a 1 ns wide current pulse excitation from threshold current to 5 times threshold current. (b) Calculation example of output noise power spectral density of a laser 128

6.4 Contour plot of (a) Small signal 3dB bandwidth and (b) PBR.. 132

6.5 Contour plot of (a) inversed laser delay time ($1/\tau_d$) under digital modulation and (b) D_n 133

6.6 Contour plots of (a) laser data rate:*DR* and (b) *EBR*. 133

7.1 Structure of a nanolaser/silicon waveguide integration.....................................140

7.2 A proposed membrane transferring process for III-V/silicon waveguide integration 140

CHAPTER 1

INTRODUCTION

1.1 Metals in optics

Metals are widely used in different optical applications due to their unique optical properties compared to dielectric materials. We can imagine a light beam incident on a smooth metal surface. Due to the screening effect of the free electron gas in metal, in most cases light beam is reflected back with only tens of nanometers penetration in to metal. One of the most common applications for metal is its use as mirrors from everyday life to scientific research. As discussed in more details in Chapter 2, if light wavelength and polarization match with metal, optical field strongly couples with the electron gas oscillation in metal, forming so-called surface plasmon polariton (SPP) wave, which is tightly confined near the metal surface. In this case metal is a plasmonic wave-guiding media which guides optical wave on metal surface in a deep sub-wavelength scale, and even below the half wavelength diffraction limit when near SPP resonance. Metal nanostructures, such as nano-tips and nano-particles, exhibit optical phenomena including optical field enhancement, scattering, light trapping, which are used in applications such as nano-antenna[1], plamonic enhanced solar cell[2], surface enhanced Raman spectroscopy[3], particle trapping[4], and high resolution lithography[5]. Metallic plamonic nano-gratings are also used in different kinds of light manipulations such as plasmon coupling[6], focusing[7], and polarization control[8].

In this thesis, I present my research on another optoelectronics application of metals: metallic cavity nanolaser. In this new type of laser, metal is used to confine light in an ultra-small cavity so as to make a laser with a total volume smaller than vacuum wavelength cubed. In this chapter, historic developments, advantages, and properties of such lasers will be presented and discussed.

1.2 A brief history of metallic cavity nanolaser

The development of semiconductor lasers in the last 50 years has been constantly driven by new materials and new designs used, from the earliest p-n junction lasers to the double hetero-junctions (DH) lasers, from DH lasers to quantum well and quantum dot lasers, from Fabry-Perot (FP) lasers to distributed feedback (DFB) lasers. Device miniaturization is always one of the major topics in such development. Representative examples include vertical cavity surface emitting lasers (VCSELs), photonic crystal lasers and various micro-cavity lasers. However, the size of a semiconductor laser with a pure dielectric cavity is fundamentally limited by the wavelength involved, which makes the realization of a deep sub-wavelength laser with pure dielectric materials extremely challenging, if not impossible. New waveguiding and confining mechanisms are needed for further laser size reduction.

Due to their high reflectivity over a large wavelength range from visible to infrared, metals are widely used in passive optic devices such as mirrors and gratings. Actually, the first demonstrated ruby laser by Maiman in 1960 used silver coatings as mirrors at the two

ends of the ruby tube. In 1991, Yamamoto *et al*[9] theoretically studied the enhanced spontaneous emission in a gold coated AlAs/GaAs micro-cavity laser. However, for a long time, it was presumed without careful investigations that loss in metal is too high so that it is unfeasible to build a laser with metallic micro/nano-cavities.

In 2007, Maslov and Ning[10] studied the modal loss and gain compensation in a semiconductor-metal core-shell structure and their results suggested that metallic nano-cavity lasers are actually practical for photon energies from 0.8 to 2 eV. In the same year, lasing from a metallic nano-cavity at 1.4 μm wavelength was demonstrated by Hill *et al*[11], removing any remaining doubt about the feasibility of metallic cavity nanolasers. A semiconductor-insulator-metal core-shell structure, similar to what Maslov and Ning proposed, was fabricated using standard III-V advanced nanofabrication techniques. An InP/InGaAs/InP DHS epi-layer grown on InP substrate was first etched into cylindrical pillars of diameters 200 nm~300 nm and then the semiconductor pillars were coated by thin SiN layers and gold to form semiconductor-dielectric-metal core-shell nano-cavities. Such nano-cavities with metallic coating can support hybrid HE_{11} mode with a reasonable Q factor at the cryogenic temperature. Lasing at 1.4 μm wavelength was demonstrated at 77 K under DC current injection in a device with a 260 nm diameter semiconductor pillar, slightly larger than the half wavelength diffraction limit ($\lambda/2n_r$, λ is vacuum wavelength, n_r is refractive index). Hill and Ning's group later on collaborated to investigate a metallic-semiconductor structure with a rectangular cross section to study the possibility of squeezing light below diffraction limit in one direction. In 2009, they demonstrated

lasing in metal-insulator-semiconductor-insulator-metal (MISIM) plasmonic waveguide at 77 K with electrical injection[12]. The thinnest waveguide core was only 90 nm, with the total thickness about one quarter of the lasing wavelength in active media or one half of the diffraction limit.

Since then, various metallic cavity nanolasers, mostly under optical pumping, have been demonstrated by many other groups worldwide. Nezhad *et al*[13] demonstrated room temperature pulse lasing under optical pumping from a circular metallo-dielectric nano-cavity laser. An InGaAs nano-disk is embedded in a SiO_2/Al shell with optimized dielectric layer thickness for minimum optical loss. Later Lee *et al*[14] modified this structure and enabled electrical injection. Recently, coaxial metallic nano-ring structures were fabricated by Khajavikhan *et al*[15]. Emission with a narrowing linewidth down to 1.6 nm under increasing pumping was observed at 4.5 K. Perahia *et al*[16] demonstrated optical pumped lasing at room temperature on micro-disks with one side covered by metal. Kwon and his collaborators demonstrated lasing from an InGaAsP nano-disks placed inside a silver plasmonic nano-pan[17]. Yu *et al* demonstrated lasing from metal-semiconductor-metal sandwich structures or so-called nanopatch lasers[18]. Lakhani *et al* fabricated 1D plasmonic crystal and demonstrated lasing[19]. In terms of electrical injection, Lu *et al*[20] coated a micro-VCSEL with a silver shell for improved light confinement and demonstrated continuous wave (CW) operation at room temperature. The dimensions of their devices were, however, over several lasing wavelengths. Marell *et al*[21] incorporated metallic DFB structure in their metallic nanolasers and successfully

demonstrated CW lasing under electrical injection.

The lasing wavelengths of all the examples above are in the region of near infrared where the noble metals (such as silver or gold) serve more as perfect reflecting mirrors[18] than as plasmonic media. At visible range, which is close to SPP resonance for typical noble metals such as gold and silver, optical field is more strongly localized at the dielectric-metal interface. Therefore device size reduction can be much more significant at this wavelength range. Plasmonic lasing[22,23] was reported with optical pumping in a CdS nanowire[22] or nanobelt[23] placed on a silver plate covered by a thin MgF_2 dielectric film. The gap between CdS and metal film can be as small as 5 nm. Noginov and his collaborators studied the idea of spaser[24]. They demonstrated narrow emission at 531 nm wavelength in nanoparticles with a 14 nm-diameter gold core and dye doped silica shell under optical pumping[25]. The diameter of the nanoparticles is only 44 nm and the localized surface plasmon oscillation of the gold nanoparticle was sustained by the optical gain in dye molecules and out-coupled to photonic mode to be detected. These demonstrations showed important potentials for deep sub-wavelength lasing even close to SPP resonance.

1.3 Metallic waveguides and cavities

1.3.1 Waveguide confinement

As mentioned above, the size of a pure dielectric cavity laser is fundamentally limited by the wavelength involved. Diffraction limit states that a light beam cannot be well confined

in an area with a size smaller than half of its wavelength in the medium. In a pure dielectric waveguide or cavity, as the size shrinks to deep sub-wavelength scale, optical mode will leak severely into outer space, leading to weak confinement. In contrast, due to metal's large negative real part of dielectric constant in optical frequency, optical mode can be well confined in a metallic waveguide even in deep sub-wavelength scale. A comparison of confining light in deep sub-wavelength scale in pure dielectric structures and metallic structures is can be illustrated in the following example.

Figure 1.1a shows the electric field profile of TE_0 mode at 1.55 μm in the 2D infinite dielectric slab waveguide in air with different width w. The dielectric constant of the slab is set to be 12, a common value for silicon and general III-V semiconductors such as InP and GaAs. When the slab width is 4 times or twice the diffraction limit ($\lambda/2n_r$), the optical mode is well confined in the slab core. But optical field spreads out significantly once the slab width is smaller than $\lambda/2n_r$. The situation is quite different in a metal-dielectric-metal MDM waveguide. As shown in Fig. 1.1b, the optical field is always well confined in the dielectric layer with marginal penetration into the metal. Here the metal in this waveguide is chosen to be silver, whose dielectric constant is -126 + 3.3i at 1.55 μm (ref. 26). The waveguide confinement factor can be calculated by[27]

$$\Gamma = \frac{n_r c \varepsilon_0 \iint |E(x,y)|^2 \, dxdy}{\iint_\infty \mathrm{Re}[E(x,y) \times H(x,y)^*] \cdot \hat{z} dxdy} \tag{1.1}$$

where E and H are the electric field and magnetic field of the mode, c is speed of light in vacuum, ε_0 is vacuum permittivity and mode is propagating in Z direction.

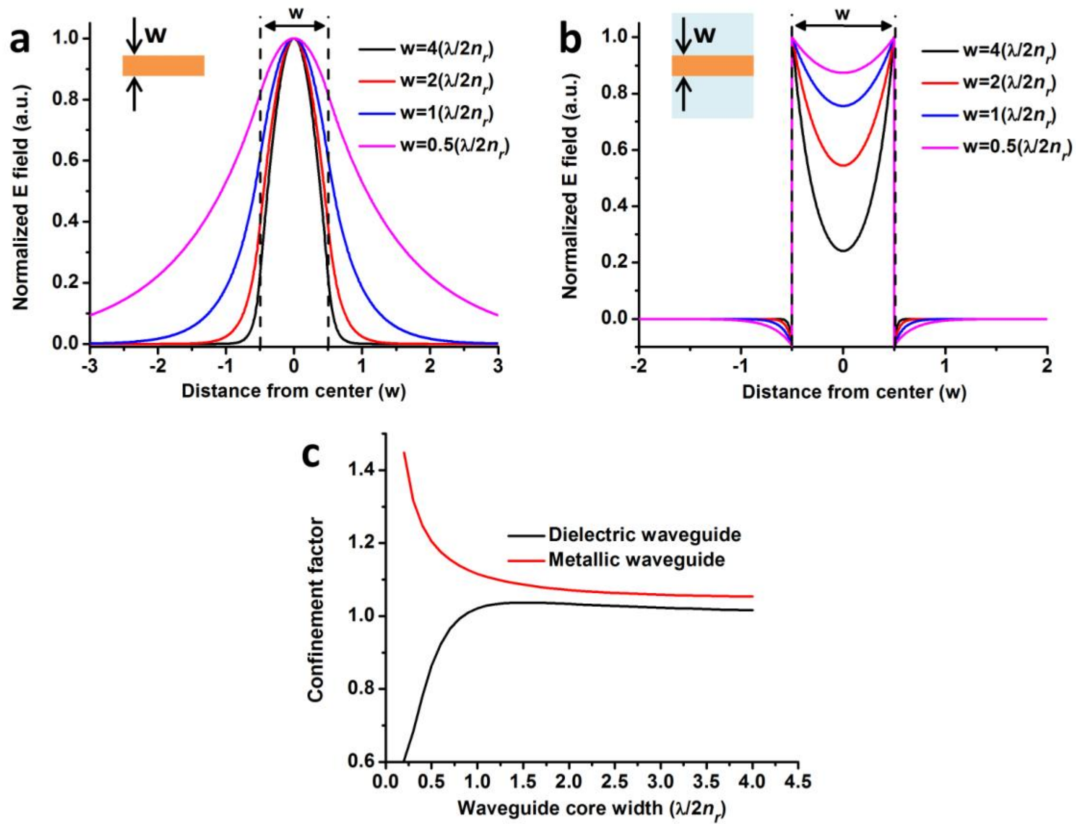

Figure 1.1 **(a)** Electric field of TE_0 mode at 1.55 μm in the 2D infinite air-dielectric (ε=12, ε is relative dielectric constant)/air slab waveguide. **(b)** Electric field of TM_0 mode at 1.55 μm in the 2D infinite silver-dielectric (ε=12)-silver slab waveguide. **(c)** Confinement factor of these two kinds of waveguide as a function of waveguide core width.

As shown in Fig. 1.1c, the confinement factor in a metallic waveguide is always larger than one while it drops rapidly in a dielectric waveguide when the core width is below the diffraction limit. Interestingly, confinement factor can be larger than one in both waveguides instead of always smaller than one. This confinement behavior will be discussed in more detail in Chapter 2.

1.3.2 Cavity Q[*] factor

A common type of dielectric micro-cavity lasers is micro-disk lasers supporting the whispering gallery modes. Figure 1.2a shows the simulated electric field of whispering gallery modes for three 2D micro-disk ($\varepsilon = 12$) cavities with resonances around 1.55 μm. The Q factor of whispering gallery mode in a large micro-disk (R = 700 nm, R is the radius of the disk) can be very high (52884). However, Q factor drops dramatically when the radius gets smaller. The Q factor for a micro-disk with 350 nm radius is only 92, which makes the threshold gain unachievable for most III-V semiconductors at room temperature. If we coat the dielectric micro-disk with silver as shown in Fig. 1.2b, the cavity Q factor from simulation is maintained at a reasonable value (326) even when its radius reduces to 150 nm. With the reasonable Q factor, lasing is achievable at room temperature in such metallic cavities.

[*] Here I use empty cavity Q, which assumes no gain or absorption in semiconductor. Intrinsic metal loss is included by taking into account the imaginary part metal dielectric constant.

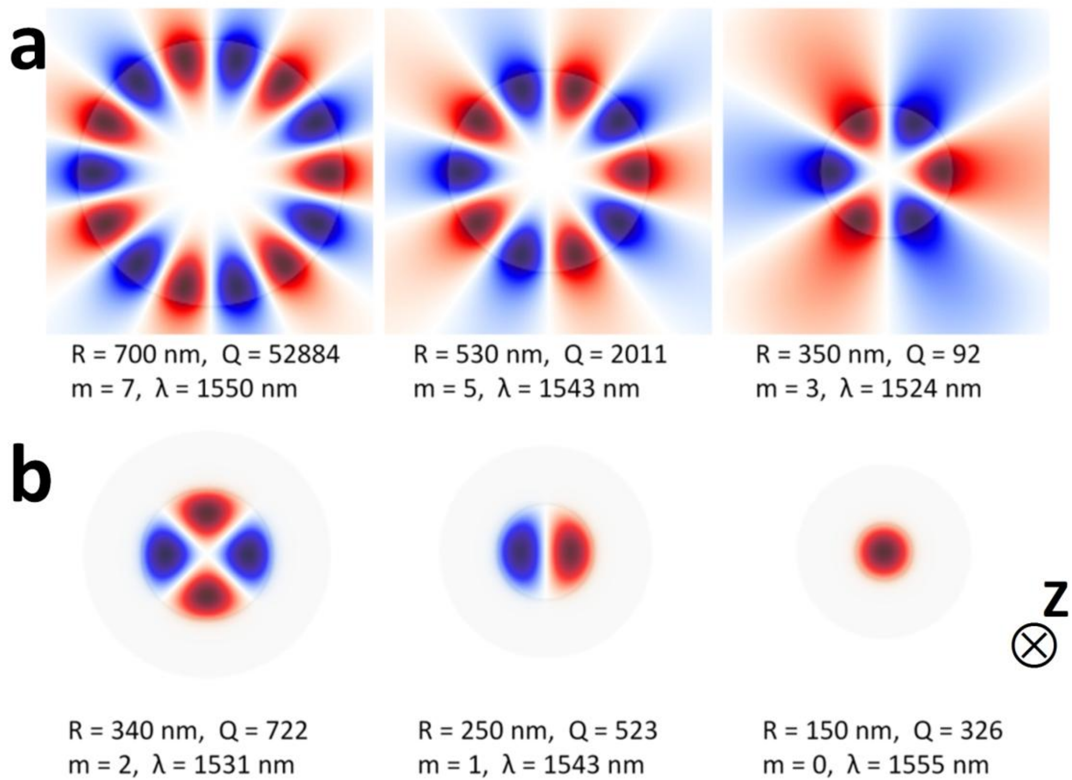

Figure 1.2 **(a)** Electric field from simulation of whispering gallery mode in microdisk cavities. **(b)** Electric field from simulation of whispering gallery mode in metallic-coated microdisk cavities. m is the folds of rotational symmetry.

1.3.3 Cross talk

Two dielectric optical components, such as lasers and waveguides, can be coupled through their evanescent fields when they are placed closely. Cross talk induced by this evanescent coupling is an important factor affecting high density integration of photonic devices. Figure 1.3 shows the overlay of the electric field of two R = 340 nm metallic disks and two R = 350 nm dielectric disks (whose mode patterns are shown in Fig. 1.2a and b). The centers of two disks are separated by 1.3 μm. Electrical field is plotted along the line connecting the centers. The dielectric disk has a strong evanescent field outside the cavity and there is a significant overlap of their optical field which will lead to a

strong coupling between these two disks. In contrast, metallic disk can confine the field inside the cavity with only a few tens of nanometers penetration into metal. Therefore, two metallic microdisks can be placed as close as physically possible without significant crosstalk, thus enabling high-density integration.

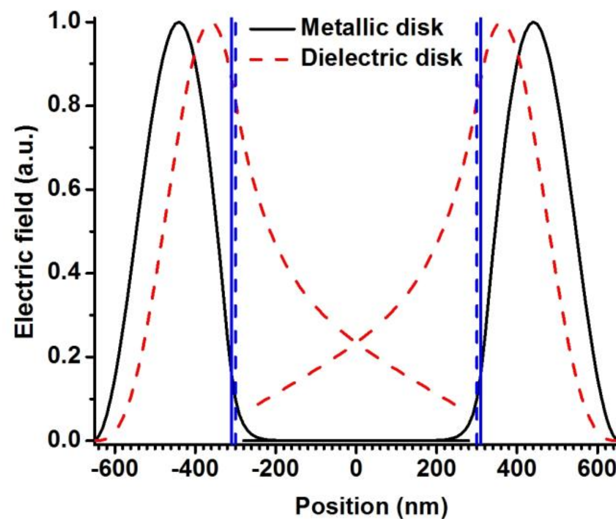

Figure 1.3 Electric field (E_z) of two R = 340 nm metallic disks (black solid line) and two R = 350 nm dielectric disks (red dashed line), along the line connecting the centers of the two cavities. The separation between two disk centers is 1.3 μm. Blue vertical lines (solid lines for metallic disk and dashed lines for dielectric disk) mark the boundaries of disks.

1.3.4 Heat dissipation

A series issue for modern very large scale integration (VLSI) circuits is that the power density consumed by the chip increases dramatically as the integration density increases. The heat dissipation becomes another roadblock in the process of increasing speed and functionality. The same problem can happen in future integrated photonic systems as well and could be even worse since self-heating is well-known for many optoelectronic devices, such lasers and detectors[28]. Metals, as good thermal conductors, can remove heat

efficiently. To compare the heat dissipation in metallic cavity nanolasers and dielectric nanolasers, I perform rate equation calculation including thermal effect for a cylindrical metallic cavity nanolaser with a diameter of 920 nm (Fig. 1.4a) coated with silver and a cylindrical dielectric cavity nanolaser with same semiconductor pillar but no metal coating (Fig. 1.4b). They have similar Q factors, 280 for the metallic laser and 421 for the dielectric laser. Chapter 5 will cover the design, fabrication and characterization the circular metallic cavity nanolasers. Figure 1.4c shows the calculated output power and active region temperature of these two lasers. The metallic nanolaser shows minimal self-heating at the active region and it can be operated far above threshold without heat roll-over. The dielectric laser though shows higher output power initially, but it temperature rises quickly due to inefficient heat dissipation and heat roll-over occurs when the laser is pumped to 3 times of threshold.

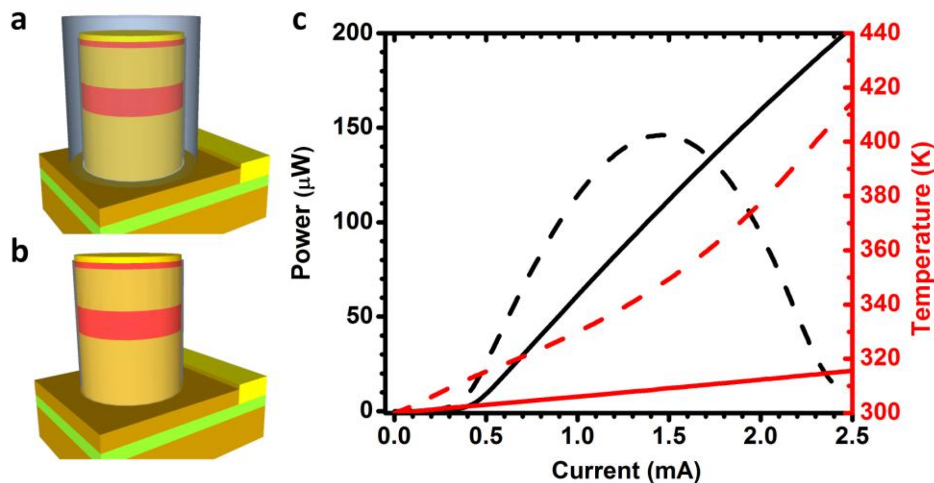

Figure 1.4 Schematic of **(a)** cylindrical metallic cavity nanolaser and **(b)** dielectric nanolaser under this thermal study. **(c)** Output power (black lines) and active region temperature (red lines) calculated by rate equations for these two lasers (solid lines for metallic cavity nanolasers, and dashed lines for dielectric cavity nanolaser).

From these four examples, it becomes quite clear that a metallic waveguide or cavity effectively confines optical mode in a deep sub-wavelength scale with a maintained cavity Q factor. The metal coating also provides efficient heat removal. All these attributes greatly facilitate further photonic device miniaturization to sub-wavelength scale. Because of this reason, metallic nano-cavity has been recognized as an effective approach for laser size reduction. Actually most nanolasers after 2007 have metallic structures as essential parts of the cavities.

1.4 Optical process in nano-cavities

Besides the advantages discussed above, the small volume and strong confinement in a metallic cavity also affect the optical process in a laser. The spontaneous emission is strongly modified by the presence of laser cavity. A well-known phenomenon is the Purcell effect[29], stating that the spontaneous emission of a dipole will be enhanced by a factor known as Purcell factor

$$F = \frac{6Q(\lambda / 2n_{eff})^3}{\pi^2 V_{eff}} \tag{1.2}$$

when the dipole is placed in a cavity compared with in free space. Here n_{eff} is the effective refractive index of the cavity, V_{eff} is the mode effective volume. This enhancement has been observed in many plasmonic structures[22]. There are also reports that the spontaneous emission of quantum dots can be also suppressed when their emission does not match with the guided mode[30]. As a net result of such modified spontaneous emission, large spontaneous emission factor, β, which is defined as the

portion of spontaneous emission coupled to lasing mode to the total spontaneous emission, has been observed in small lasers[31]. There has been argument that large β can reduce the lasing threshold and it is possible to achieve a thresholdless laser in an ultra-small nanolaser as β approaches one[15]. Such enhanced spontaneous emission and large β are also considered as important factors that influence laser modulation[32-35]. In chapter 6, I will calculate the spontaneous emission and stimulated emission in metallic nano-cavities and examine the cavity effect on the optical process in a laser and their effects on laser performance, such as threshold and modulation speed.

1.5 Objective and methods

My research work mainly focuses on design, fabrication and characterization of metallic cavity nanolasers at telecommunication wavelength based on InP/InGaAs material. I use silver to construct the metallic cavities to take the advantage of its lowest loss among noble metals at this wavelength range. The objective of my research has three aspects:

1) Demonstrate CW lasing at low temperature in devices with a deep sub-wavelength cavity volume, smaller than 0.2 λ^3.
2) Demonstrate CW lasing at room temperature in devices with a physical cavity volume smaller than λ^3.
3) Study new optical property and other fundamental properties of such nanolasers, such as polarization selection, modified spontaneous emission in nanocavities. Study issues related to nanolasers' applications, such as laser modulation.

Through such study, I hope to take the advantage of metallic nano-cavities to fabricate ultra small lasers, thus enabling the studying of new and interesting physics and pave the way of nanolasers to practical applications.

Device fabrication was performed in the cleanroom in Arizona State University (ASU) and Eindhoven University of Technology (TU/e), the Netherlands, using advanced micro/nanofabrication technologies including electron beam lithography, photolithography, plasma dry etching, plasma enhanced chemical vapor deposition, metal deposition and chemical wet etching. Device characterization was performed in the optical lab of Dr. Ning's group in ASU. Detailed results of device fabrication and characterization will be covered in Chapter 3 to 5.

Two software packages were used for optical simulation during device design and optimization. The radio frequency (RF) module in Comsol Multiphysics, a commercial software package based on finite element method (FEM), is suitable for the simulation of a 2D waveguide with an arbitrarily defined geometry. Assuming the mode propagating in the direction perpendicular to the 2D plane, the optical field, propagation wave vector of the waveguide mode at a fixed frequency can be obtained easily through such simulation at a minimum cost of time and computation resource. However, simulation for the Q factor of a 3D cavity in Comsol is not practical in our group. First, our group's Comsol is installed in a PC which does not have enough computation capability for 3D simulation. More importantly, calculating Q factor using FEM requires a frequency scan over certain frequency range to obtain the cavity's frequency response. Since Comsol can only

simulate one frequency in each simulation, it is not suitable for cavity Q simulation.

Another free software package, MEEP, is used to simulate the Q factor of a cavity. It is based on finite difference time domain (FDTD) method. Structures can be excited by a continuous or Gaussian pulse source and then optical field oscillation in time domain is monitored and converted to the frequency domain. In this way, the frequency response and mode Q factor of a structure can be extracted accurately over a certain frequency range depending on the bandwidth of the Gaussian pulse excitation in only one simulation. The major drawback of MEEP is that 3D simulation in MEEP consumes abundant computation resources like memories and processors for parallel computing and the computation time can be very long. Therefore I use the supercomputer cluster in ASU Advanced Computer Center (http://a2c2.asu.edu/) for MEEP simulation.

The relative dielectric constants of the materials in the optical simulation are ε(InP) = 10, ε(InGaAs) = 12.6 and ε(SiN) = 3.9. Since I am primarily interested in optical mode around 1.55 μm within a small bandwidth, material dispersion of dielectrics or semiconductors is not considered unless stated otherwise.

Silver dielectric constant is another important parameter in simulation since it is associated with Ohmic loss in silver which is the major loss source in a metallic waveguide or cavity. In MEEP, metal dielectric constant is modeled by a Lorentzian function[36]:

$$\varepsilon(\omega) = \varepsilon_\infty + \sum_n \frac{\sigma_n \omega_n^2}{\omega_n^2 - \omega^2 - i\omega\gamma_n} \tag{1.3}$$

Measured silver dielectric constant varies largely in literature, which will be discussed in Chapter 3. A widely cited silver dielectric constant data is from Johnson and Christy[26]. Johnson and Christy's data and fitting results are plotted in Fig. 1.5.

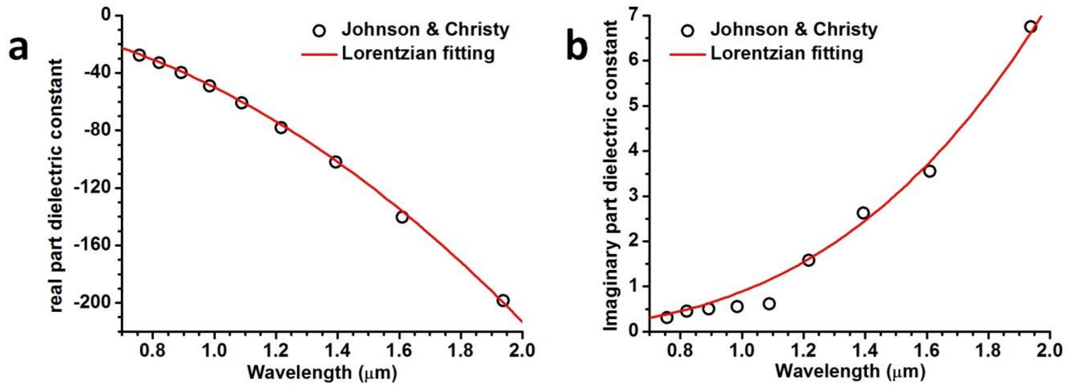

Figure 1.5 Silver dielectric constant from Johnson and Christy[26] and its Lorentzian fitting result. **(a)** Real part and **(b)** Imaginary part.

However, I found that ohmic loss in the deposited silver can be significantly higher than what Johnson and Christy's data predicts since I observed that devices' performance often falls far short of simulation predictions. Instead, I found a Lorentzian fitting of Dold *et al*'s[37] and Winsemius *et al*'s[38] data offered a better match between experiment and simulation. Dold's and Winsemius's silver data and the Lorentzian fitting result are plotted in Fig. 1.6. The fitting parameters for silver dielectric constant in the MEEP are listed in Table 1.1. When matching the simulation results with experimental results, I use silver data from the combination of Dold and Winsemius silver. If the purpose of the simulation is to study some fundamental properties of nanolasers, I use Johnson and Christy silver since it represents the lowest loss that can possibly be. I will mention the use of Johnson and Christy silver particularly in this thesis.

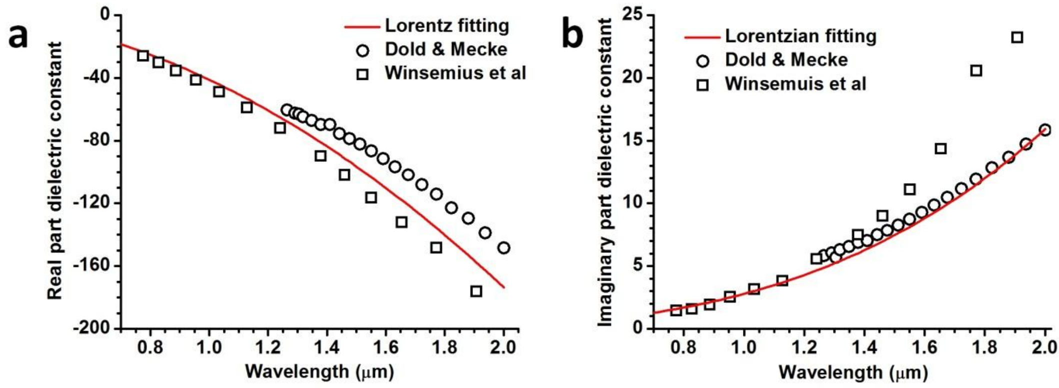

Figure 1.6 Silver dielectric constant from Dold *et al*[37] and Winsemiu *et al*[38] and the Lorentzian fitting result for a combination of these two sets of data. **(a)** Real part and **(b)** Imaginary part.

Table 1.1 Fitting parameters for silver dielectric constant in the MEEP

	Johnson & Christy	Dold & Winsemuis
n	1	2
ε_∞	2.604	1
σ_n	13198	4.4625×10^{41} 7.9247
ω_n	0.06359	1×10^{-20} 0.6582
γ_n	0.01654	0.03872 3.1343

1.6 Structure of this thesis

Materials in this thesis are organized in the following order:

In Chapter 2, I will discuss the optical properties of metals in detail and present the calculation results of characteristics of different metallic waveguides.

In Chapter 3, I will introduce the fabrication process of the nanolaser and discuss the challenges and critical steps in device fabrication.

In Chapter 4 and 5, I will show the modal properties and the characterization results from two types of nanolasers that I have fabricated with rectangular and circular geometries.

In Chapter 6, I will derive a fundamental laser rate equation model with spontaneous emission and stimulated emission rate calculated from Fermi's golden rule. With this model, I examine the performance of nanolasers, the modulation bandwidth, data rate and energy consumption.

In Chapter 7, I will summarize this thesis and give my recommendations for the future development of metallic cavity nanolaser including improvement in fabrication and possible integration design with silicon waveguide.

CHAPTER 2

METALLIC WAVEGUIDES

2.1 Introduction

The purpose of this chapter is to discuss the light confinement and waveguiding in metal -semiconductor structures which are the building blocks for metallic cavity nanolasers. I will first review the optical properties of metals. Then I will discuss optical modes in several different metal-semiconductor waveguides. Their properties, such as dispersion, propagation loss, and confinement factor will be calculated. In such waveguides, optical gain in semiconductors can compensate for metal loss[39, 40] and even achieve net gain to enable lasing in a metallic cavity[10- 12]. Such gain compensation will be discussed as well. Silver dielectric constant data from Johnson and Christy[26] is used through this chapter.

2.2 Optical properties of metals

In optical frequency regime, noble metals such as gold and silver, demonstrate a negative real part of dielectric constant, which can be attributed to the existence of free electron gas, or plasmas, in metal. A classic picture of metal dielectric constant is derived as following[41].

Under the driving of a harmonic electric field $\hat{E}(r,t) = \hat{r}E_0 \exp(-j\omega t)$, the movement of a free electron can be described by Drude model as:

$$m_e \frac{d^2 r}{dt^2} + m_e \gamma \frac{dr}{dt} = -eE_0 \exp(-j\omega t) \tag{2.1}$$

e is the electron charge unit , m_e is the effective mass of the free electron, γ is the electron damping rate. Assuming the solution has the form $r(t) = r_0 \exp(-j\omega t)$, then I have:

$$r_0 = \frac{eE_0}{m_e \omega (j\gamma + \omega)} \tag{2.2}$$

Now I consider the collective effect of all free electrons in a solid, and the complex amplitude of macroscopic polarization per unit volume is:

$$P(r,t) = -ner(t) = \frac{-e^2 n E_0 \exp(-j\omega t)}{m_e \omega (j\gamma + \omega)} \tag{2.3}$$

Here n is the free electron density.

The electric displacement vector is expressed as:

$$D(r,t) = \varepsilon_0 E(r,t) + P(r,t) = \varepsilon_0 \varepsilon E(r,t) \tag{2.4}$$

ε_0 is the vacuum permittivity and ε is the relative dielectric constant.

Then I come to an expression for ε:

$$\varepsilon = 1 - \frac{\omega_p^2}{\omega^2 + j\gamma\omega} \tag{2.5}$$

$\omega_p = \sqrt{ne^2/(m_e \varepsilon_0)}$ is the plasma frequency. In semiconductors, a background term should be added to (2.4) and 1 should be replaced by $1+\varepsilon_b$ in (2.5), where ε_b corresponds to the relative dielectric constant of the background (without free charges).

For silver, the Drude model gives a dielectric constant that fits measured data quite well over a large wavelength range from visible to near infrared as shown in Fig. 2.1.

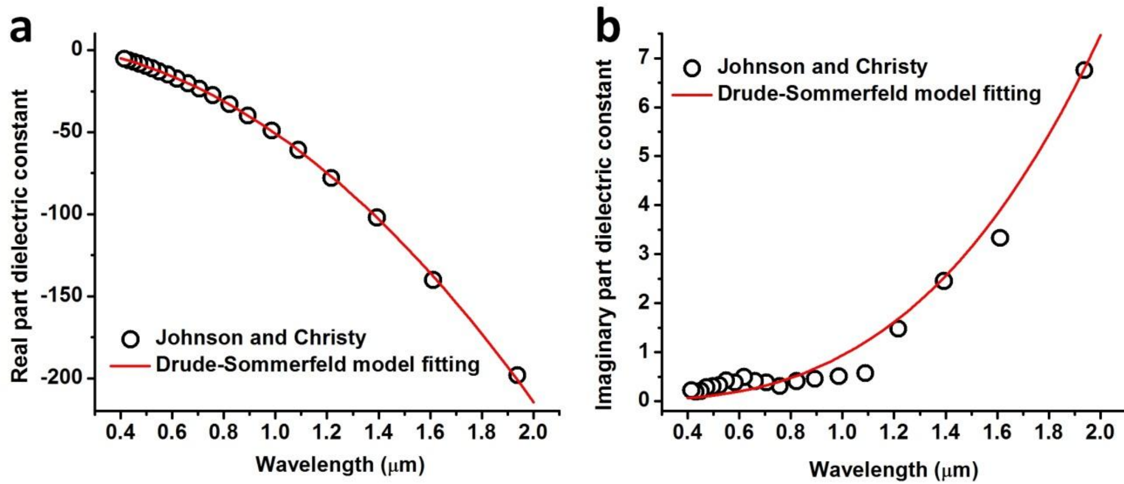

Figure 2.1 Silver dielectric constant from Johnson and Christy[26] (○) and Drude model (−) fitting result. **(a)** Real part and **(b)** Imaginary part.

In higher energy range, Lorentzian model can be introduced to take into account the interband transitions[42] and a more general expression for metal dielectric constant is as:

$$\varepsilon = \varepsilon_\infty - \frac{\omega_p^2}{\omega^2 + j\gamma\omega} + \omega_p^2 \sum_n \frac{f_n}{\omega_n^2 - \omega^2 - j\gamma_n\omega} \tag{2.6}$$

f_n, ω_n, and γ_n are the strength, frequency and damping rate for each oscillator, where ε_∞ is the dielectric constant at high frequency and $\varepsilon_\infty = 1+\varepsilon_b$ for semiconductors.

It is easy to show that (1.3) and (2.6) are equivalent when the frequency of the first oscillator ω_1 in (1.3) approaches to zero.

2.3 Surface Plasmon Polariton waveguide

In general, both dielectric modes and SPP modes can be supported in a metallic waveguide structure. Here I will discuss these two kinds of modes in section 2.3 and 2.4.

2.3.1 Metal/semiconductor waveguide

The simplest metallic waveguide is the single metal-semiconductor (MS) interface. A

SPP wave, which is the coupling between optical field and free electron gas oscillation in metal, can be localized and propagate along the interface of metal and semiconductor as shown in Fig. 2.2.

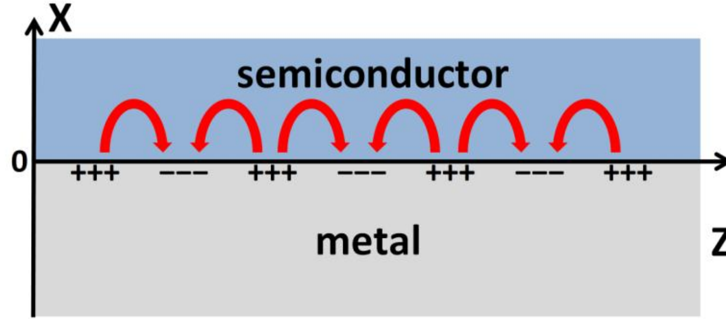

Figure 2.2 Schematic of a single metal-semiconductor interface waveguide supporting a SP wave propagating in Z direction along the interface of a metal and a semiconductor. Red arrows show the electric field. +, − signs show the charge density oscillations in metal.

An analytical solution for this SPP wave can be derived using auxiliary vector potentials method[43]. Components of the electromagnetic (EM) field of TM_z[*]mode are expressed as:

$$
\begin{aligned}
E_x &= -j\frac{1}{\omega\mu_0\varepsilon_0\varepsilon}\frac{\partial^2 A_z}{\partial x\partial z} & H_x &= \frac{1}{\mu_0}\frac{\partial A_z}{\partial y} \\
E_y &= -j\frac{1}{\omega\mu_0\varepsilon_0\varepsilon}\frac{\partial^2 A_z}{\partial y\partial z} & H_y &= -\frac{1}{\mu_0}\frac{\partial A_z}{\partial x} \\
E_z &= -j\frac{1}{\omega\mu_0\varepsilon_0\varepsilon}\left(\frac{\partial^2}{\partial z^2}+\beta^2\right)A_z & H_z &= 0
\end{aligned}
\tag{2.7}
$$

Here A_z is the vector potential associated with electric current source and satisfies:

$$\nabla^2 A_z + \beta^2 A_z = 0 \tag{2.8}$$

[*] The subscript is the direction which the polarization is with respect to. TM_z and TE_z mean no magnetic field or electric field in Z direction respectively.

$b^2 = w^2 m_0 e_0 e_{s,m}$, ε_s, ε_m are the dielectric constant of semiconductor and metal respectively. ∇^2 is the three dimensional Laplacian. Assuming EM field is localized at the metal-semiconductor interface, A_z should exponentially decay from the interface. The medium is uniform in Y direction, so A_z is independent of Y. Then a solution for A_z is

$$A_z = \begin{cases} A_s \exp(-k_s x - j\beta_z z) & x > 0 \text{ in semiconductor} \\ A_m \exp(k_m x - j\beta_z z) & x < 0 \text{ in metal} \end{cases} \tag{2.9}$$

Here $\beta_z - k_{s,m}^2 = \beta_{s,m}^2$. β_z is the propagation constant in propagating Z direction. k_s and k_m are the decay constants in to semiconductor and metal in X direction.

Then the EM field is updated as:

$$\begin{aligned} E_x &= \frac{k_s \beta_z}{\omega \mu_0 \varepsilon_0 \varepsilon_s} A_s \exp(-k_s x - j\beta_z z) & H_x &= 0 \\ E_y &= 0 & H_y &= \frac{k_s}{\mu_0} A_s \exp(-k_s x - j\beta_z z) \\ E_z &= -j \frac{1}{\omega \mu_0 \varepsilon_0 \varepsilon_s} (\beta_s^2 - \beta_z^2) A_s \exp(-k_s x - j\beta_z z) & H_z &= 0 \end{aligned} \tag{2.10}$$

in semiconductor ($x > 0$), and

$$\begin{aligned} E_x &= -\frac{k_m \beta_z}{\omega \mu_0 \varepsilon_0 \varepsilon_m} A_m \exp(k_m x - j\beta_z z) & H_x &= 0 \\ E_y &= 0 & H_y &= -\frac{k_m}{\mu_0} A_m \exp(k_m x - j\beta_z z) \\ E_z &= -j \frac{1}{\omega \mu_0 \varepsilon_0 \varepsilon_m} (\beta_m^2 - \beta_z^2) A_m \exp(k_m x - j\beta_z z) & H_z &= 0 \end{aligned} \tag{2.11}$$

in metal ($x < 0$).

At the interface the boundary conditions

$$\begin{aligned} E_z^{0+} &= E_z^{0-} \\ \varepsilon_s E_x^{0+} &= \varepsilon_m E_x^{0-} \end{aligned} \tag{2.12}$$

lead to

$$k_s / \varepsilon_s + k_m / \varepsilon_m = 0 \tag{2.13}$$

Combining with $\beta_z - k_{s,m}^2 = \beta_{s,m}^2$, I finally get:

$$\beta_z = \beta_0 \sqrt{\frac{\varepsilon_m \varepsilon_s}{\varepsilon_m + \varepsilon_s}} \tag{2.14}$$

where $\beta_0 = \omega\sqrt{\mu_0 \varepsilon_0}$.

I repeat the same process for TE_z mode. The EM field is expressed as:

$$\begin{aligned} E_x &= -\frac{1}{\varepsilon_0 \varepsilon}\frac{\partial F_z}{\partial y} & H_x &= \frac{1}{\mu_0}\frac{\partial F_z}{\partial y} \\ E_y &= \frac{1}{\varepsilon_0 \varepsilon}\frac{\partial F_z}{\partial x} & H_y &= -j\frac{1}{\omega \mu_0 \varepsilon_0 \varepsilon}\frac{\partial^2 F_z}{\partial y \partial z} \\ E_z &= 0 & H_z &= -j\frac{1}{\omega \mu_0 \varepsilon_0 \varepsilon}\left(\frac{\partial^2}{\partial z^2} + \beta^2\right)F_z \end{aligned} \tag{2.15}$$

Here F_z is the vector potential associated with magnetic current source and satisfies:

$$\nabla^2 F_z + \beta^2 F_z = 0 \tag{2.16}$$

It is easy to show that such TE_z mode does not have a solution that satisfies the boundary conditions. Therefore this single-interface metal-semiconductor waveguide can only support the TM_z mode.

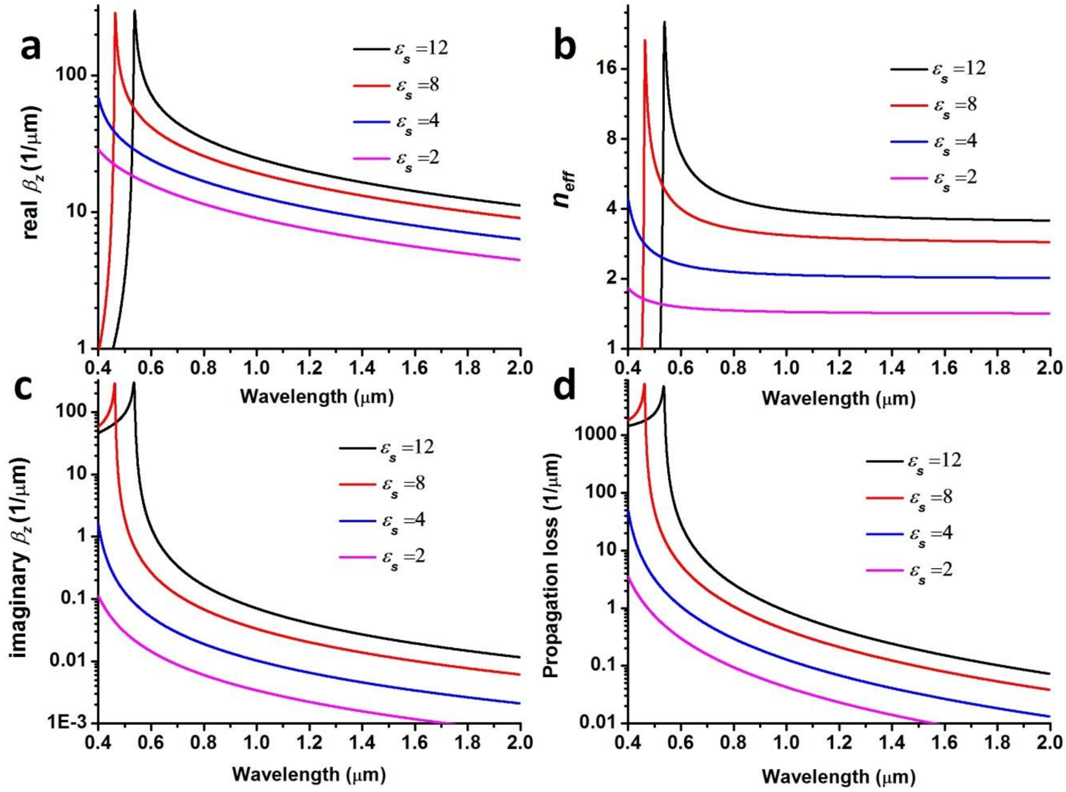

Figure 2.3 Propagation constant of SPP mode in a single silver-dielectric waveguide with different dielectric constants of dielectrics **(a)** real part and **(c)** imaginary part. **(b)** and **(d)** show the corresponding mode effective refractive index and propagation loss.

Figure 2.3a and 2.3c show the real and imaginary part of β_z of the SPP wave propagating along silver-dielectric interface using Drude model. The corresponding effective refractive index $n_{eff} = real(\beta_z)/\beta_0$ and propagation loss $\alpha = 2 \cdot imag(\beta_z)$ are plotted in Fig. 2.3b and 2.3d. A resonance peak exists in all four plots, corresponding to the SPP resonance. As the wavelength changes from near infrared to visible or ultra-violet, the real part of silver dielectric constant will increase to approaching zero. At a certain wavelength (as known as SPP resonance), the real part of silver dielectric constant and semiconductor dielectric constant cancel out in the denominator of (2.14),

leading to a peak in β_z as shown in Fig. 2.3a and 2.3c. As the semiconductor dielectric constant decreases, this resonance will shift to shorter wavelength. Figure 2.4a and b show the electric field (E_x) and its energy density of SPP wave at different wavelengths in a silver-semiconductor ($\varepsilon_s = 12$) interface. As the wavelength approaches the SPP resonance from 1.55 μm to 0.55 μm, the electric field is more and more strongly localized at the interface, and also more and more symmetric. As a result, more and more energy is located at the metal side.

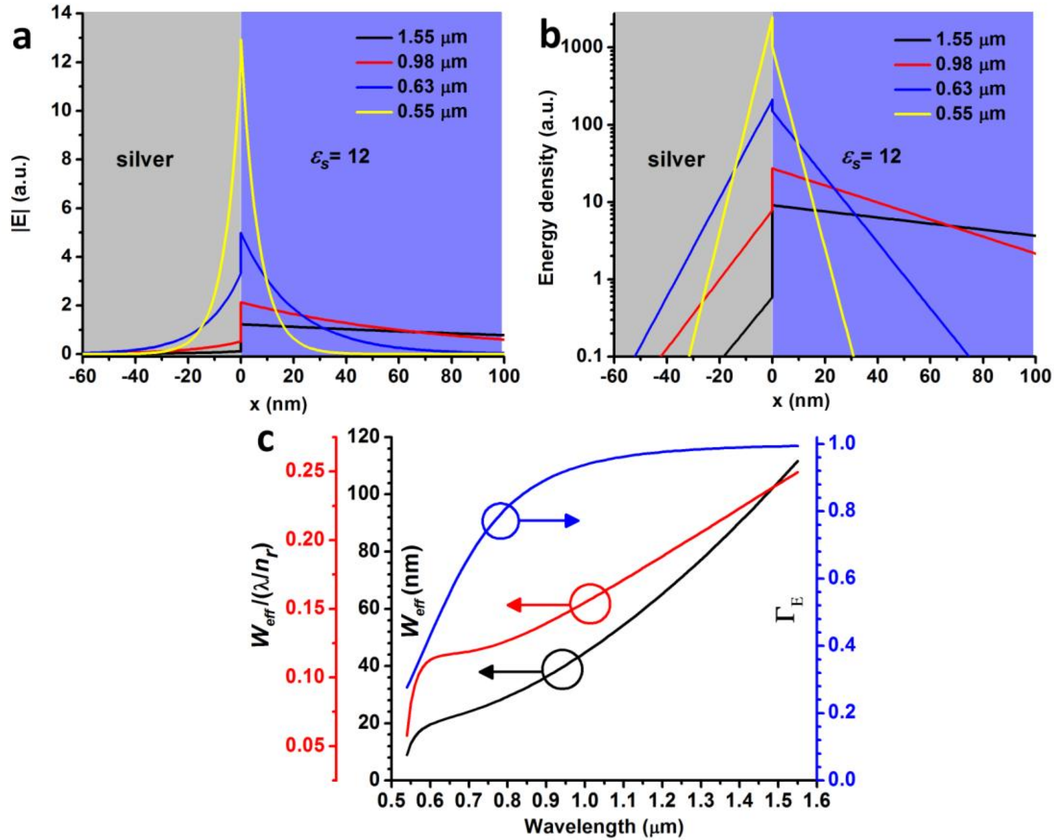

Figure 2.4 **(a)** Electric field (Ex) and **(b)** its energy density of SPP mode in a silver-semiconductor waveguide ($\varepsilon_s = 12$) of different wavelengths. **(c)** Effective mode width and energy confinement factor of this mode at different wavelengths. The outer left Y axis shows the effective mode width in terms of wavelength in semiconductor (λ/n_r).

To quantify the wave confinement in a MS waveguide, similar to effective mode area[30], I define an effective mode width as:

$$W_{eff} = \frac{\int_{semi} \varepsilon_0 \varepsilon_s |E|^2 \, dx + \int_{met} \frac{d(\omega \varepsilon_0 \varepsilon_m)}{d\omega} |E|^2 \, dx}{\varepsilon_0 \varepsilon(x_{max}) |E_{max}|^2} \tag{2.17}$$

As can be seen in Fig. 2.4c, when far away from the SPP resonance in the near infrared, W_{eff} is quite large, over tens of nanometers and one fifth of the wavelength in semiconductor (λ/n_r), since wave is loosely bounded to the interface. Near the resonance, W_{eff} is dropped to under 20 nm and $0.1(\lambda/n_r)$, indicating a strong confinement to the interface. This is also consistent with the strongly increased effective index shown in Fig. 2.3b, where the effective index increased from ~4 far away from resonance to >20 near resonance. The drawback of this strong confinement near resonance is the huge propagation loss associated as shown in Fig. 2.3d. In Fig. 2.4c, I also plot the energy confinement factor for semiconductor as:

$$\Gamma_E = \frac{\int_{semi} \varepsilon_0 \varepsilon_s |E|^2 \, dx}{\int_{semi} \varepsilon_0 \varepsilon_s |E|^2 \, dx + \int_{met} \frac{d(\omega \varepsilon_0 \varepsilon_m)}{d\omega} |E|^2 \, dx} \tag{2.18}$$

Near SPP resonance, energy confinement factor for semiconductor is reduced, which means more and more energy is stored in metal and dissipating due to ohmic loss in metal. Therefore propagation loss will increase when the wavelength is approaching the SPP resonance. Another reason for this increased loss is that near resonance, SPP wave is significantly slowed down and suffers more energy loss per unit length[44].

Through the above discussion, it can be seen that there is a trade-off between mode confinement and loss in the single-interface MS waveguide. Wave is strong confined near the resonance at visible but with a huge propagation loss. At near infrared far away from the resonance, the loss is relatively low but wave confinement is poor. Thus a single such interface would not be a good waveguide for visible or infrared wavelengths.

2.3.2 Metal-semiconductor-air waveguide

In the treatment of the single-interface metal-semiconductor SPP waveguide, the thicknesses of the semiconductor and metal layers, which should be finite in practice, are both assumed to be infinite. Such assumption is reasonable for metal, since the optical field penetration depth into metal is only tens of nanometers, thinner than the metal thickness usually used. However, the finite thickness of semiconductor layer needs to be taken into account in a real waveguide, especially when the mode is loosely confined the semiconductor layer in near infrared as shown in Fig. 2.4a. I here consider a metal-semiconductor-air (MSA) structure shown is shown in Fig. 2.5 with a finite semiconductor layer thickness.

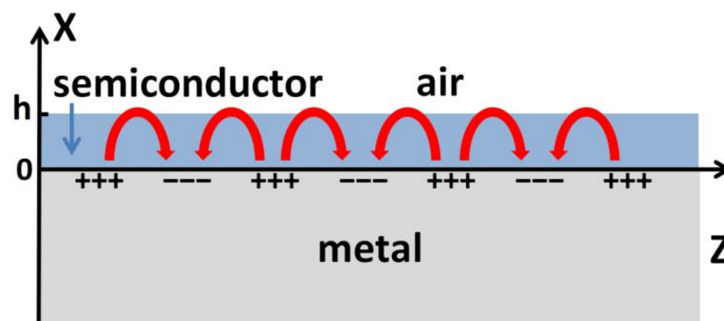

Figure 2.5 Schematic of a SPP wave propagating in a MSA waveguide

Using the same vector potential method, the EM field of the SPP mode in a MSA waveguide can be expressed as:

$$\left.\begin{aligned}
E_x &= -A_m \frac{\beta_z k_m}{\omega\mu_0\varepsilon_0\varepsilon_m}\exp(k_m x)\exp(-j\beta_z) \\
E_z &= jA_m \frac{{k_m}^2}{\omega\mu_0\varepsilon_0\varepsilon_m}\exp(k_m x)\exp(-j\beta_z) \\
H_y &= -A_m \frac{k_m}{\mu_0}\exp(k_m x)\exp(-j\beta_z)
\end{aligned}\right\} \text{ in metal} \qquad (2.19)$$

$$\left.\begin{aligned}
E_x &= -\frac{\beta_z k_s}{\omega\mu_0\varepsilon_0\varepsilon_s}(A_s\exp(k_s x) - B_s\exp(-k_s x))\exp(-j\beta_z) \\
E_z &= j\frac{{k_s}^2}{\omega\mu_0\varepsilon_0\varepsilon_s}(A_s\exp(k_s x) + B_s\exp(-k_s x))\exp(-j\beta_z) \\
H_y &= -\frac{k_s}{\mu_0}(A_s\exp(k_s x) - B_s\exp(-k_s x))\exp(-j\beta_z)
\end{aligned}\right\} \text{in semiconductor} \qquad (2.20)$$

$$\left.\begin{aligned}
E_x &= A_a \frac{\beta_z k_a}{\omega\mu_0\varepsilon_0\varepsilon_m}\exp(-k_a x)\exp(-j\beta_z) \\
E_z &= jA_a \frac{k_a^2}{\omega\mu_0\varepsilon_0\varepsilon_m}\exp(-k_a x)\exp(-j\beta_z) \\
H_y &= A_a \frac{k_a}{\mu_0}\exp(-k_a x)\exp(-j\beta_z)
\end{aligned}\right\} \text{ in air} \qquad (2.21)$$

The application of the boundary conditions at the two interfaces leads to the following equation:

$$\begin{vmatrix}
k_m & -k_s & k_s & 0 \\
0 & k_s\exp(k_s h) & -k_s\exp(-k_s h) & k_a\exp(-k_a h) \\
k_m^2/\varepsilon_m & -k_s^2/\varepsilon_s & -k_s^2/\varepsilon_s & 0 \\
0 & k_s^2\exp(k_s h)/\varepsilon_s & -k_s^2\exp(k_s h)/\varepsilon_s & -k_a^2\exp(k_a h)
\end{vmatrix} = 0 \qquad (2.22)$$

Here since the ε_m is a complex number as $\varepsilon_m = \varepsilon_{mr} + j\varepsilon_{mi}$, so β_z, k_m, k_s and k_a are all

complex numbers, which makes solving this equation, even numerically, very difficult and time-consuming. For the wavelengths longer than 600 nm (ranging from near red to infrared), $/\varepsilon_{mi}/$ is much smaller than $|\varepsilon_{mr}/$, such that this equation can be solved first only with ε_{mr} to obtain the real parts of β_z, k_m, k_s and k_a and then use $j\varepsilon_{mi}$ as a perturbation to calculate their imaginary parts. The details of such perturbation calculation are described in the appendix.

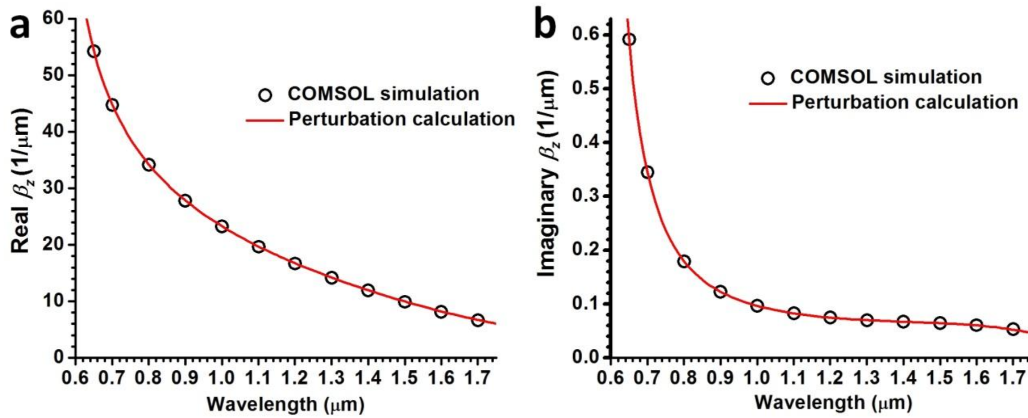

Figure 2.6 Propagation constant of SPP mode in a silver-semiconductor (h = 100 nm, ε_s = 12) -air waveguide. **(a)** Real part **(b)** Imaginary part. Solid lines are from perturbation calculation; hollow circles are from COMSOL simulation without any approximation.

The calculated β_z for a MSA waveguide with h = 100 nm and ε_s = 12 is plotted in Fig. 2.6. To check the accuracy of the perturbation calculation, the simulation result from COMSOL without any approximation is also plotted as a comparison. The perturbation calculation generates both real and imaginary parts of β_z quite accurately from 650 nm to longer wavelengths.

Figure 2.7 shows the electric field and its energy density of SPP modes at different wavelengths in a MSA waveguide with a semiconductor layer of 100 nm. The electric

field is strongly confined in the metal layer when near the SPP resonance. When wavelength is far away from the resonance (e.g.1550 nm), most of the electric field spreads out in the air other than confined in semiconductor layer. Only at a moderate wavelength, optical field is mostly confined in semiconductor layer. As a net result, the energy confinement factor in Fig. 2.7c shows a maximum around 1.2 μm wavelength.

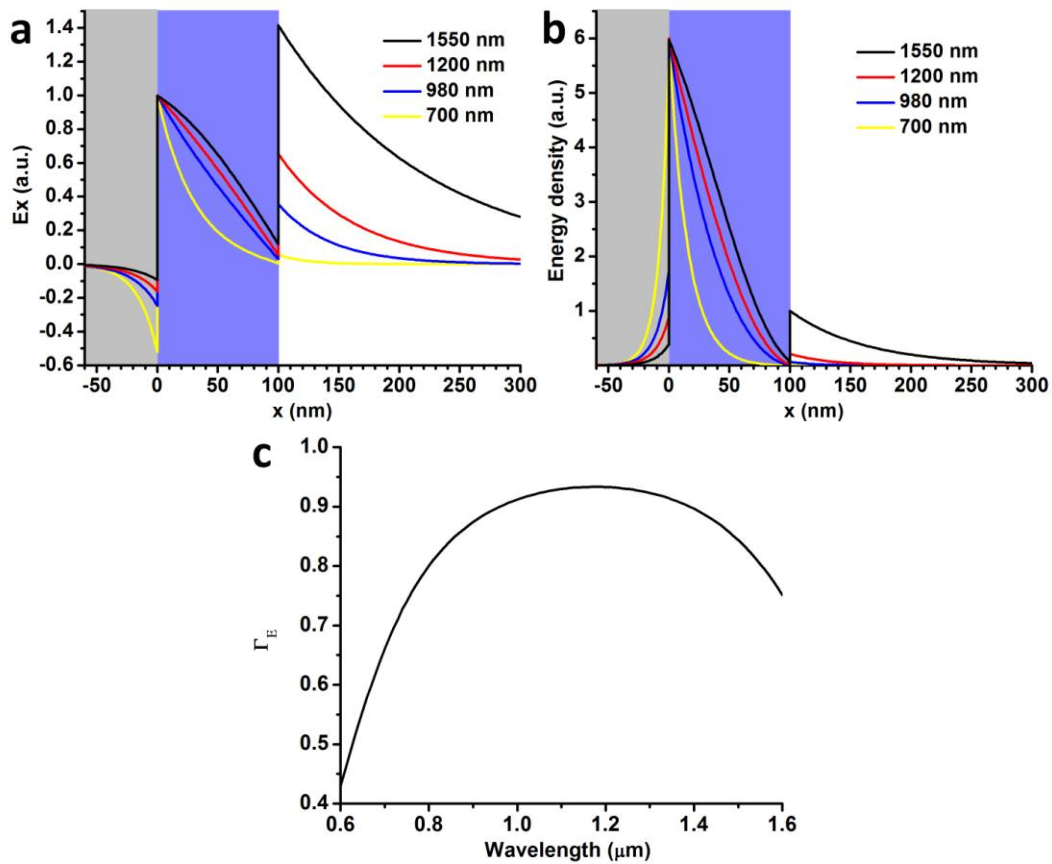

Figure 2.7 **(a)** Electric field (Ex) and **(b)** its energy density of SPP modes at different wavelengths in a silver-semiconductor silver-semiconductor (h = 100 nm, ε_s = 12)-air waveguide. **(c)** Energy confinement factor of this waveguide as a function of wavelength.

2.3.3 Metal-semiconductor-metal waveguide

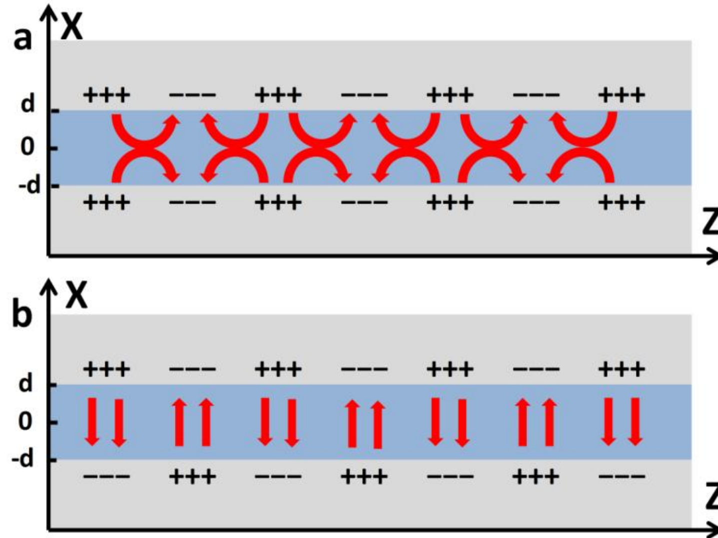

Figure 2.8 Schematic of **(a)** even and **(b)** odd SPP mode in a metal-semiconductor-metal waveguide.

In both MS and MSA waveguide, SPP mode at the near infrared is loosely bound to the metal-semiconductor interface, and the confinement is weak. To improve the confinement for the long wavelength waves, a second metal film can be introduced on top of the semiconductor. The structure of this metal-semiconductor-metal (MSM) waveguide is shown in Fig. 2.8. In this MSM waveguide, the charge oscillation in metal can be either symmetric (Fig. 2.8a) or anti-symmetric (Fig. 2.8b). Please notice that the mode electric field associated with symmetric charge oscillation is actually anti-symmetric (Fig. 2.8a) and likewise for the symmetric mode in Fig. 2.8b.

The expression for EM field is derived as following.

Anti-symmetric mode (Fig. 2.8a)

$$\left.\begin{aligned}
E_x &= -A_m \frac{\beta_z k_m}{\omega\mu_0\varepsilon_0\varepsilon_m}\exp(k_m(x+d))\exp(-j\beta_z) \\
E_z &= jA_m \frac{k_m^2}{\omega\mu_0\varepsilon_0\varepsilon_m}\exp(k_m(x+d))\exp(-j\beta_z) \\
H_y &= -A_m \frac{k_m}{\mu_0}\exp(k_m(x+d))\exp(-j\beta_z)
\end{aligned}\right\} \text{in the bottom metal} \quad (2.23)$$

$$\left.\begin{aligned}
E_x &= -A_s \frac{\beta_z k_s}{\omega\mu_0\varepsilon_0\varepsilon_s}(\exp(k_s x)-\exp(-k_s x))\exp(-j\beta_z) \\
E_z &= jA_s \frac{k_s^2}{\omega\mu_0\varepsilon_0\varepsilon_s}(\exp(k_s x)+\exp(-k_s x))\exp(-j\beta_z) \\
H_y &= -A_s \frac{k_s}{\mu_0}(\exp(k_s x)-\exp(-k_s x))\exp(-j\beta_z)
\end{aligned}\right\} \text{in semiconductor} \quad (2.24)$$

$$\left.\begin{aligned}
E_x &= A_m \frac{\beta_z k_m}{\omega\mu_0\varepsilon_0\varepsilon_m}\exp(-k_m(x-d))\exp(-j\beta_z) \\
E_z &= jA_m \frac{k_m^2}{\omega\mu_0\varepsilon_0\varepsilon_m}\exp(-k_m(x-d))\exp(-j\beta_z) \\
H_y &= A_m \frac{k_m}{\mu_0}\exp(-k_m(x-d))\exp(-j\beta_z)
\end{aligned}\right\} \text{in the top metal} \quad (2.25)$$

Symmetric mode (Fig. 2.8b)

$$\left.\begin{aligned}
E_x &= A_m \frac{\beta_z k_m}{\omega\mu_0\varepsilon_0\varepsilon_m}\exp(k_m(x+d))\exp(-j\beta_z) \\
E_z &= jA_m \frac{k_m^2}{\omega\mu_0\varepsilon_0\varepsilon_m}\exp(k_m(x+d))\exp(-j\beta_z) \\
H_y &= A_m \frac{k_m}{\mu_0}\exp(k_m(x+d))\exp(-j\beta_z)
\end{aligned}\right\} \text{in the bottom metal} \quad (2.26)$$

$$\left.\begin{aligned}
E_x &= -A_s \frac{\beta_z k_s}{\omega\mu_0\varepsilon_0\varepsilon_s}(\exp(k_s x)+\exp(-k_s x))\exp(-j\beta_z) \\
E_z &= jA_s \frac{k_s^2}{\omega\mu_0\varepsilon_0\varepsilon_s}(\exp(k_s x)-\exp(-k_s x))\exp(-j\beta_z) \\
H_y &= -A_s \frac{k_s}{\mu_0}(\exp(k_s x)+\exp(-k_s x))\exp(-j\beta_z)
\end{aligned}\right\} \text{in semiconductor} \quad (2.27)$$

$$\left.\begin{aligned} E_x &= A_m \frac{\beta_z k_m}{\omega\mu_0\varepsilon_0\varepsilon_m}\exp(-k_m(x-d))\exp(-j\beta_z) \\ E_z &= jA_m \frac{k_m^2}{\omega\mu_0\varepsilon_0\varepsilon_m}\exp(-k_m(x-d))\exp(-j\beta_z) \\ H_y &= A_m \frac{k_m}{\mu_0}\exp(-k_m(x-d))\exp(-j\beta_z) \end{aligned}\right\}\text{in the top metal} \qquad (2.28)$$

Applying the boundary conditions at both interfaces for both modes, it comes to two transcendental equations that define the dispersion relations of the modes in this MSM waveguide.

For symmetric mode: $\frac{k_s}{\varepsilon_s}\tanh(k_s d) + \frac{k_m}{\varepsilon_m} = 0$ (2.29)

For anti-symmetric mode: $\frac{k_s}{\varepsilon_s}\coth(k_s d) + \frac{k_m}{\varepsilon_m} = 0$ (2.30)

Perturbation method as described in section 2.3.2 and in appendix is used to solve these two equations. The calculated β_z for a MSM waveguide with d = 50 nm and $\varepsilon_s = 12$ is plotted in Fig. 2.9. The anti-symmetric mode shows a cut-off around 1 μm wavelength while the symmetric mode does not have such cut-off. Also the anti-symmetric mode has a large imaginary part of β_z than the symmetric mode, which means larger propagation loss. Comparing with simulation results from COMSOL, the perturbation calculation is quite accurate as in the previous case. In the symmetric mode, the imaginary part of β_z reduces with longer wavelength, indicating less propagation loss when far away from the SPP resonance in the MSM waveguide.

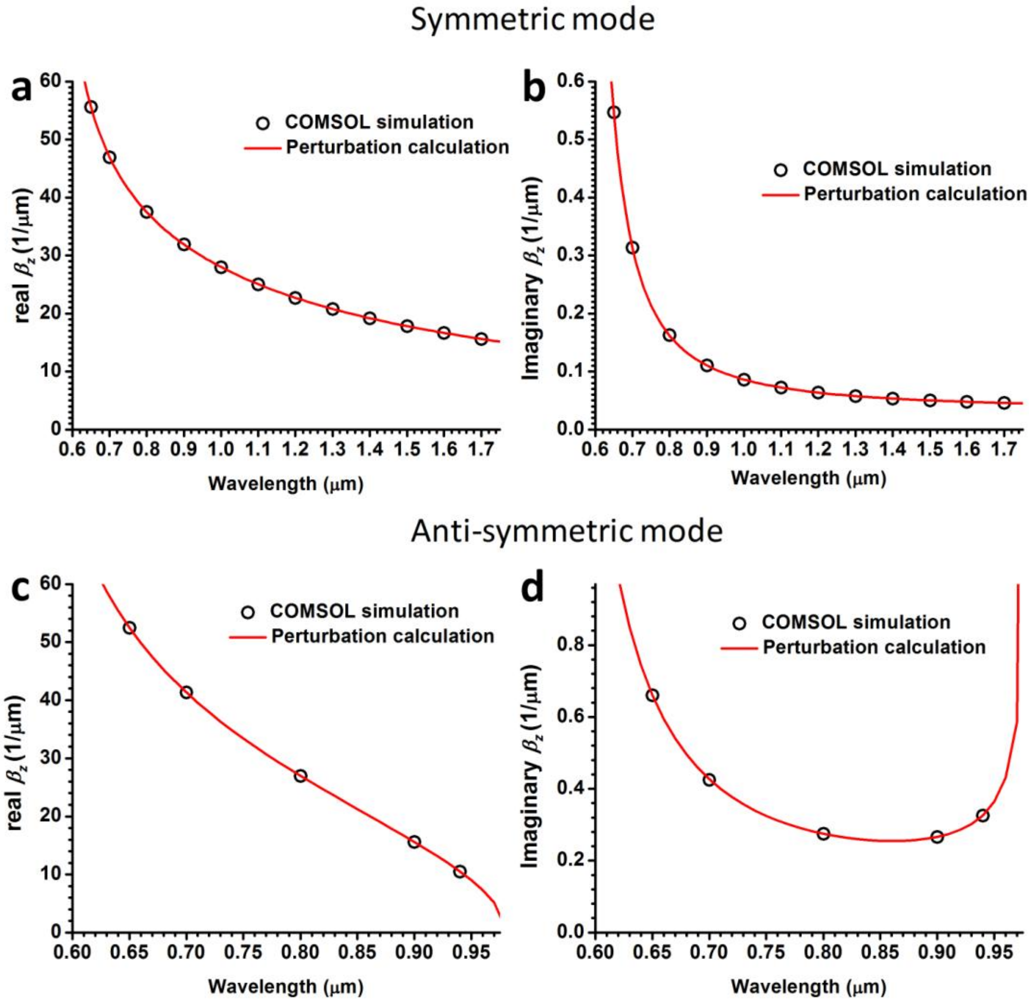

Figure 2.9 **(a)** **(c)** Real and **(b)** **(d)** imaginary part of propagation constant of SPP mode in a silver-semiconductor-silver waveguide. Solid lines are from perturbation calculation, and hollow circles are from COMSOL simulation.

Figure 2.10 shows the electric field and its energy density for both symmetric (Fig. 2.10a, b) and anti-symmetric (Fig. 2.10c, d) modes in a MSM waveguide with a semiconductor layer of 100 nm at different wavelengths. Electric field is always tightly confinement between the two metal plates, even at 1.55 μm wavelength. If the wavelength is close to the SPP resonance in the MS structure, the electric field becomes more and more localized at the semiconductor-metal interface.

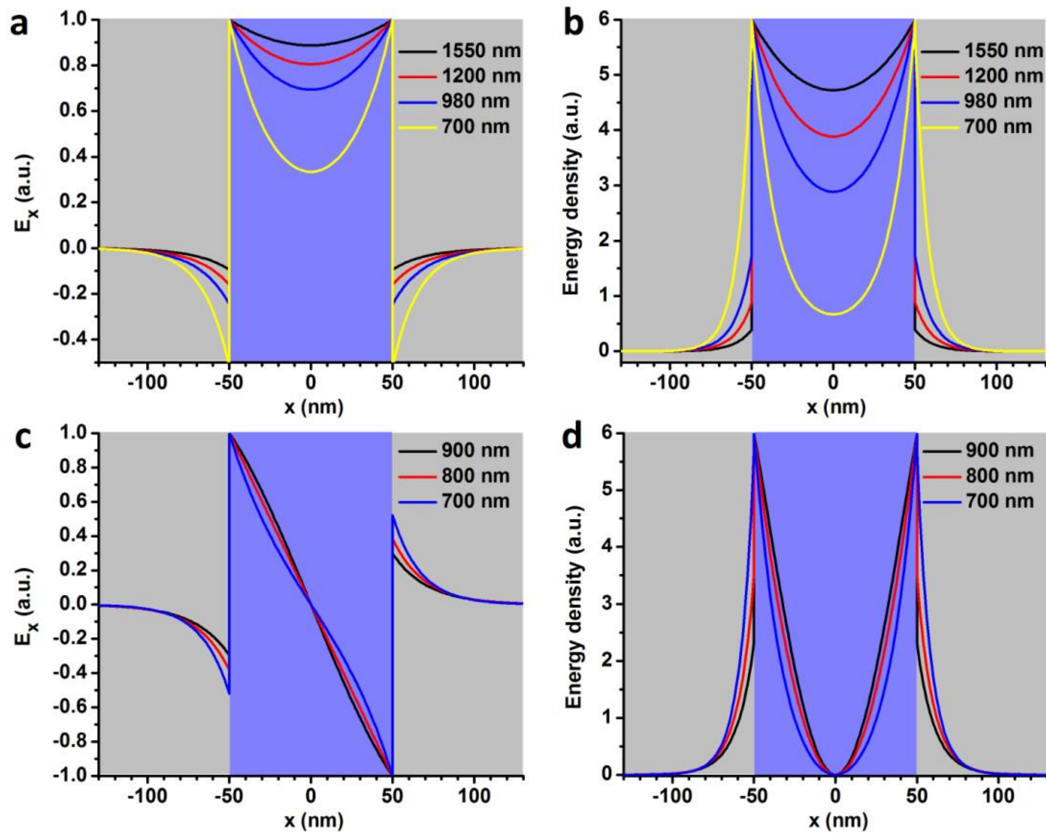

Figure 2.10 Electric field (E_x) and its energy density of SPP modes at different wavelengths in a silver-semiconductor (d = 50 nm, ε_s = 12) silver waveguide. **(a) (b)** Symmetric mode and **(c) (d)** Anti-symmetric mode.

2.4 TE modes in Metal-Semiconductor waveguides

All the modes discussed above are TM modes in which the dominant electric field is perpendicular to the metal surface. With such polarization, the optical field has a strong interaction with the electron plasma in metal and so they are as know as SPP mode. The advantage of those SPP modes is that the waveguide size can be shrunk to below the half-wavelength diffraction limit. For example, such SPP mode at 1.55 μm can be supported in a MSM waveguide with a semiconductor core layer thinner than 100 nm (see Fig. 2.10a), which is only about half the diffraction limit. On the other hand, if the

semiconductor layer is thicker than the half-wavelength diffraction limit, TE modes with dominant electric field parallel to the metal surface can also be supported in MSA and MSM waveguide.

In a MSA waveguide (shown in Fig. 2.5), the EM field of a TE_z mode is expressed as:

$$\left.\begin{aligned} E_y &= A_m \frac{k_m}{\varepsilon_0 \varepsilon_m} \exp(k_m x) \exp(-j\beta_z z) \\ H_x &= -A_m \frac{\beta_z k_m}{\omega \mu_0 \varepsilon_0 \varepsilon_m} \exp(k_m x) \exp(-j\beta_z z) \\ H_z &= jA_m \frac{k_m^2}{\omega \mu_0 \varepsilon_0 \varepsilon_m} \exp(k_m x) \exp(-j\beta_z z) \end{aligned}\right\} \text{ in metal} \qquad (2.31)$$

$$\left.\begin{aligned} E_y &= \frac{k_s}{\varepsilon_0 \varepsilon_s} (A_s \cos(k_s x) - B_s \sin(k_s x)) \exp(-j\beta_z z) \\ H_x &= -\frac{\beta_z k_s}{\omega \mu_0 \varepsilon_0 \varepsilon_s} (A_s \cos(k_s x) - B_s \sin(k_s x)) \exp(-j\beta_z z) \\ H_z &= -j \frac{k_s^2}{\omega \mu_0 \varepsilon_0 \varepsilon_s} (A_s \sin(k_s x) + B_s \cos(k_s x)) \exp(-j\beta_z z) \end{aligned}\right\} \text{ in semiconductor} \qquad (2.32)$$

$$\left.\begin{aligned} E_y &= -A_a \frac{k_a}{\varepsilon_0} \exp(-k_a x) \exp(-j\beta_z z) \\ H_x &= A_a \frac{\beta_z k_a}{\omega \mu_0 \varepsilon_0} \exp(-k_a x) \exp(-j\beta_z z) \\ H_z &= jA_a \frac{k_a^2}{\omega \mu_0 \varepsilon_0} \exp(-k_a x) \exp(-j\beta_z z) \end{aligned}\right\} \text{ in air} \qquad (2.33)$$

Applying the boundary conditions, I obtain:

$$\begin{vmatrix} k_m/\varepsilon_m & -k_s/\varepsilon_s & 0 & 0 \\ 0 & k_s \cos(k_s h)/\varepsilon_s & -k_s \sin(k_s h)/\varepsilon_s & k_a \exp(-k_a h) \\ k_m^2/\varepsilon_m & 0 & k_s^2/\varepsilon_s & 0 \\ 0 & k_s^2 \sin(k_s h)/\varepsilon_s & k_s^2 \cos(k_s h)/\varepsilon_s & k_a^2 \exp(-k_a h) \end{vmatrix} = 0 \qquad (2.34)$$

Figure 2.11 shows the results of perturbation calculation of propagation wave constant of the TE_z mode in a MSA waveguide with h = 200 nm. Unlike the SPP mode, the imaginary part of β_z increases at longer wavelengths, indicting an increased propagation loss with wavelength. This is because the TE modes is approaching the cut-off at a longer wavelength, which can be seen in the reduced real part of β_z (Fig. 2.11a).

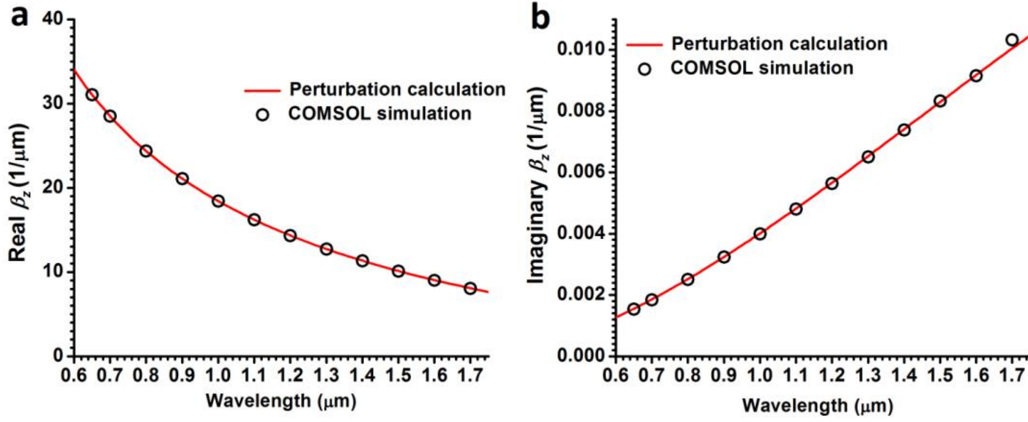

Figure 2.11 **(a)** Real and **(b)** imaginary part of propagation constant of TE_z mode in a silver-semiconductor (h = 200 nm, ε_s = 12)-air waveguide. Solid lines are from perturbation calculation. Hollow circles are from COMSOL simulation.

For the MSM waveguide, only the EM field of symmetric TE_z mode will be discussed since it is a lower order mode and has a longer cut-off wavelength than the anti-symmetric mode[43].

$$\left.\begin{aligned} E_y &= -A_m \frac{k_m}{\varepsilon_0 \varepsilon_m} \exp(k_m(x+d)) \exp(-j\beta_z z) \\ H_x &= A_m \frac{\beta_z k_m}{\omega\mu_0 \varepsilon_0 \varepsilon_m} \exp(k_m(x+d)) \exp(-j\beta_z z) \\ H_z &= jA_m \frac{k_m^2}{\omega\mu_0 \varepsilon_0 \varepsilon_m} \exp(k_m(x+d)) \exp(-j\beta_z z) \end{aligned}\right\} \text{ in the bottom metal} \quad (2.35)$$

$$\left.\begin{aligned} E_y &= A_s \frac{k_s}{\varepsilon_0 \varepsilon_s} \cos(k_s x) \exp(-j\beta_z z) \\ H_x &= -A_s \frac{\beta_z k_s}{\omega\mu_0 \varepsilon_0 \varepsilon_s} \cos(k_s x) \exp(-j\beta_z z) \\ H_z &= -jA_m \frac{k_s^2}{\omega\mu_0 \varepsilon_0 \varepsilon_s} \sin(k_s x) \exp(-j\beta_z z) \end{aligned}\right\} \text{ in semiconductor} \quad (2.36)$$

$$\left.\begin{aligned} E_y &= -A_m \frac{k_m}{\varepsilon_0 \varepsilon_m} \exp(-k_m(x-d)) \exp(-j\beta_z z) \\ H_x &= A_m \frac{\beta_z k_m}{\omega\mu_0 \varepsilon_0 \varepsilon_m} \exp(-k_m(x-d)) \exp(-j\beta_z z) \\ H_z &= -jA_m \frac{k_m^2}{\omega\mu_0 \varepsilon_0 \varepsilon_m} \exp(-k_m(x-d)) \exp(-j\beta_z z) \end{aligned}\right\} \text{ in the top metal} \quad (2.37)$$

The application of boundary conditions leads to

$$k_m = k_s \tan(k_s d) \quad (2.38)$$

Figure 2.12 shows the results of perturbation calculation of the real and imaginary part of propagation constant of the TE_z mode in a MSM waveguide with $d = 100$ nm. Again, an increased imaginary part of β_z is observed since the mode is approaching the cut-off at longer wavelengths.

Comparing Fig. 2.11 and Fig. 2.12, it can be seen that though these two waveguides both have 200 nm semiconductor layer, the MSM waveguide exhibits a cut-off wavelength around 1.65 μm while MSA waveguide has a longer cut-off wavelength. This is related to the fact that MSA waveguide is a semi-open waveguide so a long wavelength mode can spread out into air while MSM waveguide is hermetic waveguide in which mode is always confined between two metal plates. This can be seen from Fig. 2.13 where the electric fields (E_y) of TE_z mode in MSA and MSM waveguide with 200 nm

semiconductor layer are shown. Electric field in MSA waveguide significantly spreads out at 1.55 μm wavelength, while in the MSM waveguide, optical mode is always confined by the metal layers such that the electric field profiles are almost identical from 700 nm to 1.55 μm.

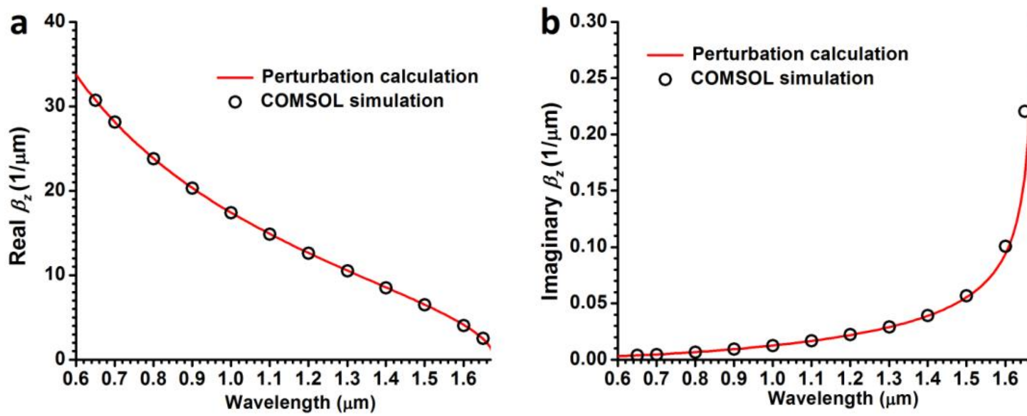

Figure 2.12 **(a)** Real and **(b)** imaginary part of propagation constant of TE_z mode in a silver-semiconductor (d = 100 nm, ε_s = 12)-silver waveguide. Solid lines are from perturbation calculation, hollow circles are from COMSOL simulation.

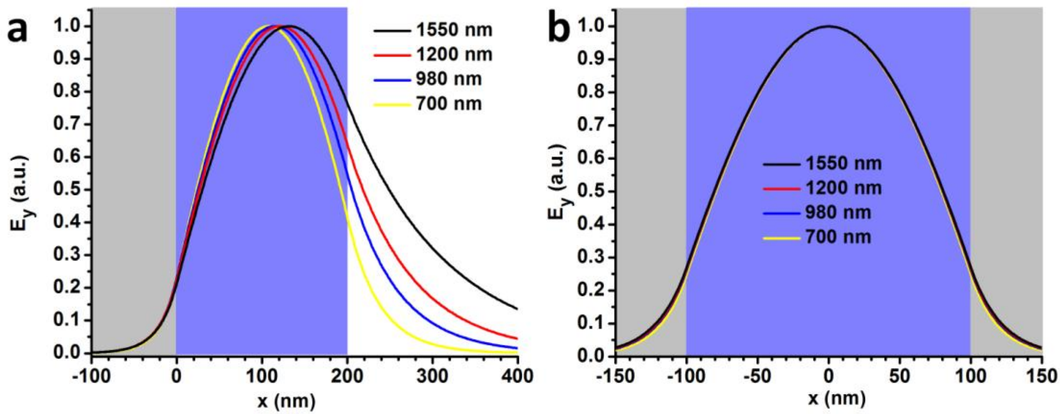

Figure 2.13 Electric field (E_y) of TE_z modes at different wavelengths in **(a)** MSA and **(b)** MSM waveguide with 200 nm semiconductor layer.

2.5 Effective waveguide width

The discussion so far has focused on mode dispersion in various metallic waveguide structures. Since the main promised advantage of metallic waveguides is its capability to confine optical field tightly to scale photonic devices down to sub-wavelength sizes, it is useful to define an effective waveguide width to compare different structures. In section 2.3.1, an effective mode width is defined as (2.17) to measure how the mode optical field is confined or localized in a waveguide. For example, Fig 2.14a shows the effective mode width of SPP mode in a MS waveguide and a MSM waveguide with a 200 nm thick semiconductor core layer for the wavelength from 550 nm to 1.7 μm. When the wavelength is approaching the SPP resonance, SPP mode is tightly localized at the metal-semiconductor interface, and therefore the effective mode width reduces. Such effective mode width definition works fine for the MS waveguide. But for the MSM waveguide, such mode width near SPP resonance can be even much smaller than the 200 nm semiconductor layer thickness, which can be misleading if this width is used for the design of real applications. In this sense, it is not proper to use the effective mode width as the effective waveguide width.

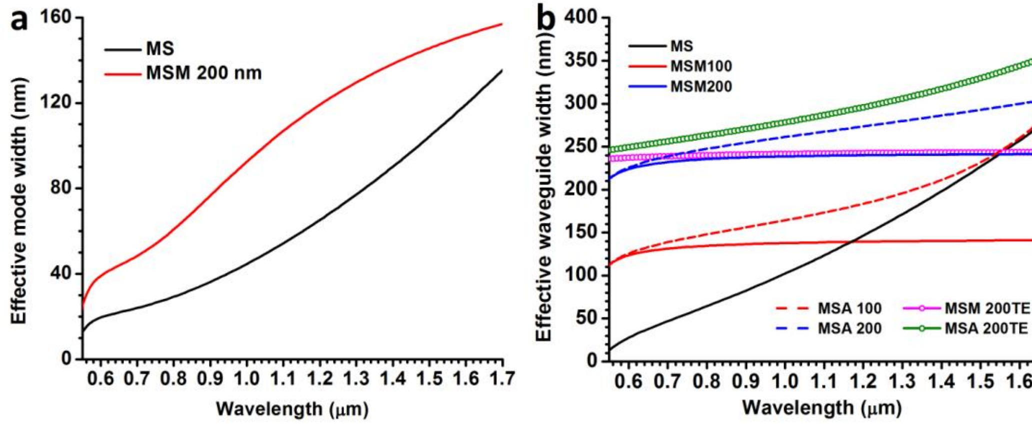

Figure 2.14 **(a)** Effective mode width calculated by (2.17) for the SPP mode in a MS waveguide and MSM waveguide with 200 nm thick semiconductor core layer. **(b)** Effective waveguide width calculated by (2.39). Solid lines are for SPP mode in MS, MSM with a 100 nm semiconductor layer (MSM100) and a 200 nm semiconductor layer (MSM200). Dashed lines are for SPP mode in MSA with a 100 nm semiconductor layer (MSA100) and a 200 nm semiconductor layer (MSA200). Circled lines are for TE mode in MSM (MSM 200TE) and MSA (MSA 200TE) with a 200 nm semiconductor layer.

A proper effective waveguide useful for the design of real applications must consider the physical dimension of the waveguide itself as well. To take into account the physical thickness of semiconductor layer, an effective waveguide width defined as:

$$W_{eff_wg} = W_{semi} + W_m + W_{air} \tag{2.39}$$

would be more reasonable. Here W_{semi} is the thickness of semiconductor core layer*. W_m and W_{air} are the penetration depth of EM field into metal and air, which is expressed as:

$$W_m = \begin{cases} 1/k_m & \textit{single side metal} \\ 2/k_m & \textit{double side metal} \end{cases}$$

$$W_{air} = 1/k_a$$

Effective modal widths defined in (2.39) are plotted in Fig. 2.14b for different

* For MS waveguide, W_{semi} is the penetration depth into semiconductor as $W_{semi} = 1/k_s$

waveguides. MS and MSA are semi-open waveguides and their effective waveguide width will increase with wavelength, meaning optical modes spread more into semiconductor or air at longer wavelengths. But for MSM waveguides, optical field is always confined between the two metal plates, and the effective waveguide width at long wavelengths saturates at near infrared.

2.6 Confinement factor and gain compensation of various waveguides

Optical loss in metallic waveguides can be compensated for by the optical gain in semiconductor gain. Such gain compensation can be described as[27]:

$$G_{\mathrm{mod}} = \Gamma g - \alpha \tag{2.40}$$

Here G_{mod} is the modal gain the mode experienced in waveguide, g is the material gain in semiconductor, $\alpha = 2 \times imag(\beta_z)$ is the propagation loss and the gain (or semiconductor) confinement factor Γ is calculated by (1.1)[27]:

A waveguide threshold material gain, defined as the material gain required to balance the propagation loss in the waveguide is calculated by:

$$g_{w_th} = \alpha / \Gamma \tag{2.41}$$

Figure 2.15 shows the calculated propagation loss, confinement factor, and the for MS, 100 nm MSM, 100 nm MSA, 200 nm MSM, 200 nm MSA waveguide, respectively, where the thickness refers to the thickness of the semiconductor layer. The TE mode in 200 nm MSA waveguide and 200 nm MSM waveguide has the lowest and second lowest waveguide threshold material gain. The TE mode in 200 nm MSM waveguide has the

second lowest waveguide threshold material gain. Considering that the effective waveguide width for the 200 nm MSM is only around 240 nm and the waveguide width for 200 nm MSA keeps increasing with wavelength, The TE mode in MSM waveguide provides a good trade-off between waveguide size and required threshold gain. Fig. 2.15b shows that confinement factor can be much larger than one for TM mode in near the SPP resonance and for TE mode near the cut-off. This is because of the significant slowing down of mode in these two regions. When the mode is slowed down, it will experience more loss (if the waveguide is lossy) or gain (if the waveguide has net gain) than propagating in bulk material, thus leading to a confinement factor larger than one. An interesting giant model gain in due to this peculiar behavior of confinement factor in metallic waveguide has been analyzed and discussed in Ref. 27, 44.

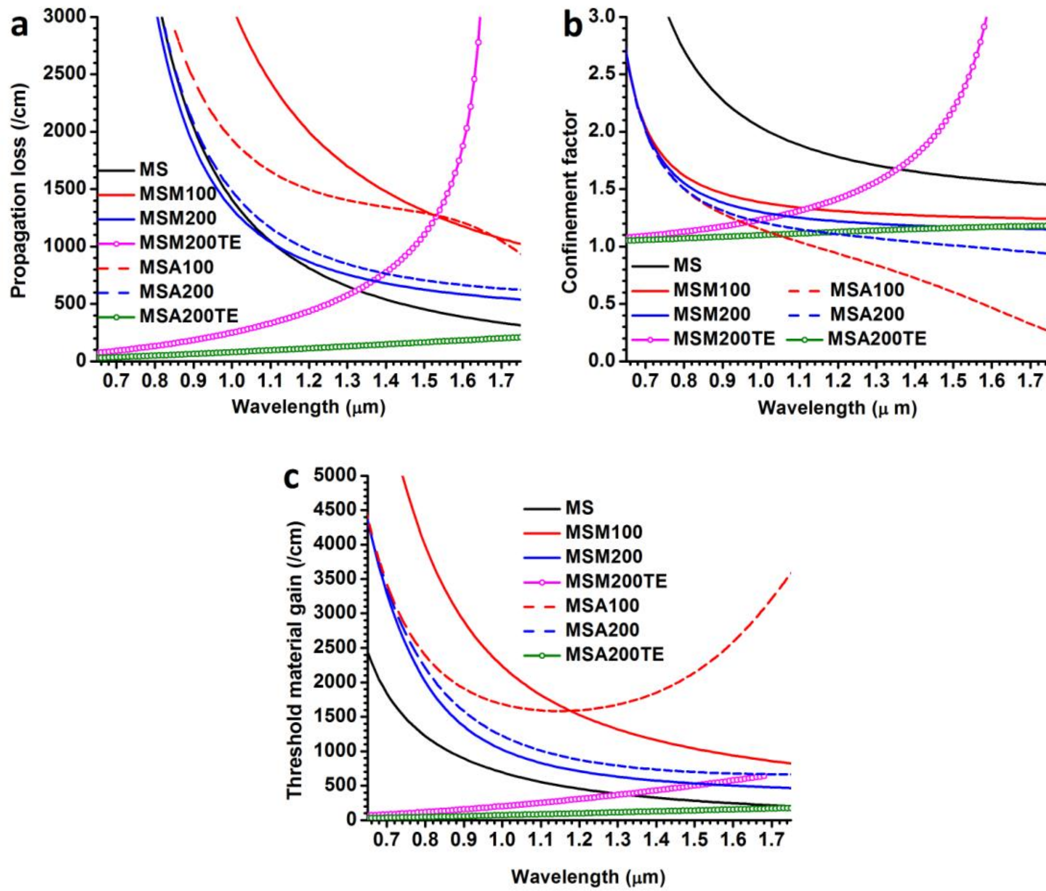

Figure 2.15 **(a)** Propagation loss, **(b)** confinement factor in semiconductor, and **(c)** waveguide threshold material gain for MS, 100 nm MSM, 100 nm MSA, 200 nm MSM, 200 nm MSA waveguide. Legends here are the same as in Fig. 2.14.

2.7 Summary

In this chapter, the Drude model for metal dielectric constant is derived. Mode dispersion, electric field profile, propagation loss, effective mode width, confinement factor, and waveguide threshold material gain are calculated rigorously for single-interface MS waveguide. Using perturbation method, those properties are also calculated for double-interface MSA and MSM waveguide. A general trade-off among mode confinement, propagation loss and waveguide threshold material gain can be seen from

these calculations. The SPP mode near the SPP resonance is strongly localized in metal-semiconductor interface in MS, MSA and MSM waveguide, leading to ultra-small effective mode width. Therefore, the SPP mode in metallic waveguides offer a great superiority in device miniaturization than conventional pure dielectric waveguide, whose miniaturization is limited by the wavelength involved as discussed in Chapter 1. However, such confinement for SPP mode is at the cost of huge loss and waveguide threshold material gain. On the other hand, if the semiconductor layer thickness in MSA and MSM waveguide is larger than the half wavelength diffraction limit, the supported TE mode shows a much lower propagation loss and waveguide threshold material gain than SPP mode until the TE mode approaches its cut-off, while good confinement is still provided by the mirror-like metals. If ultra-strong field confinement down to deep sub-wavelength scale is not required, such TE mode will be a good trade-off between all these factors. In Chapter 4, I will show laser designs with a low threshold using this low loss TE mode.

CHAPTER 3

PROCESSING

3.1 Introduction

This chapter will focus on the fabrication of metallic cavity nanolasers. I will first introduce the structures of the two types of nanolasers that have been fabricated. Afterwards, wafer design, device fabrication process and the final packaging will be described in detail. Several batches of nanolasers were fabricated and the fabrication process described here is from the batch with optimized processing and resulted in best device performance. Several important issues in fabrication have been investigated with both simulations and experiments and will be discussed in this chapter as well.

3.2 Device structure

Two types of nanolasers were fabricated whose structures are schematically shown in Fig. 3.1. For the purpose of displaying the key parts of device, the top n-contact pad is not shown in this figure. The device core is an InP/InGaAs/InP p-i-n double heterostructure pillar covered by a thin SiN layer on the sidewall. Then the whole pillar is encapsulated in silver to forms a metallic cavity. The InP/InGaAs/InP layer provides a vertical refractive index profile of 3.16 (InP) / 3.55 (InGaAs) / 3.16 (InP)[45] to confine optical field in the InGaAs active region along the vertical direction. Electrical injection is enabled through n and p contacts. The n-contact is made through contact metal on top of the pillar. The p-contact is made on the p-type InGaAsP contact layer underneath the cavity. The cross section of the semiconductor pillar is either rectangular or circular, which is defined in the initial electron beam lithography (EBL) step. All other fabrication steps for these two types of devices are identical and therefore they can be fabricated on one wafer in a single run.

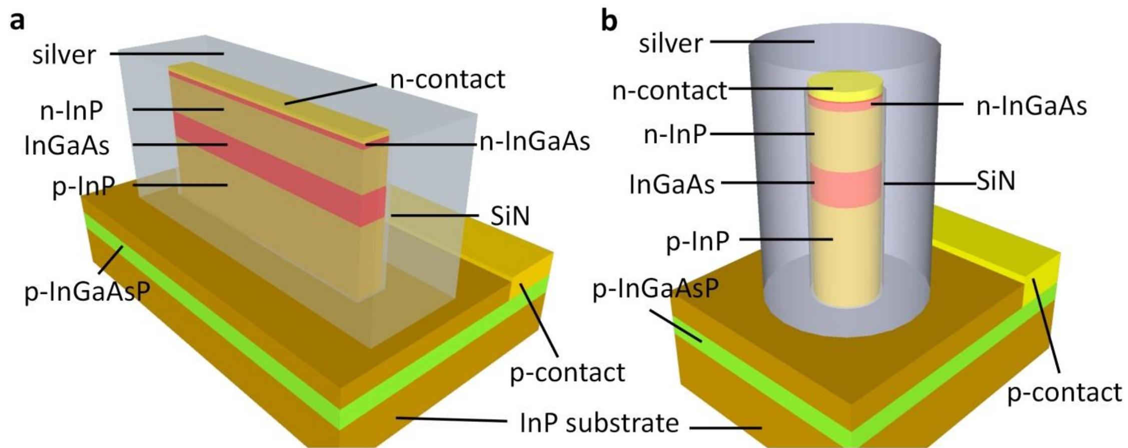

Figure 3.1 Schematic structure of metallic cavity nanolasers. Semiconductor pillar with a **(a)** rectangular or (**b)** circular cross section is encapsulated in silver to form a metallic cavity.

3.3 Wafer design

A double side polished InP wafer with epitaxial layers grown by metal organic chemical vapor deposition (MOCVD) is used for nanolasers fabrication. Wafer structure is shown in Table 3.1.

All the epi-layers are lattice matched to InP. The top 50 nm of InP layer is used to protect the underneath InGaAs layer from oxidation or environmental erosion after growth. Then the 100 nm highly doped InGaAs layer (No. 1) is the n-type ohmic contact layer. Layers No. 2-No. 8 form an InP/InGaAs/InP double heterostructures , which provides confinement for both carriers and optical field due to its potential well and refractive index profile[46]. The energy bandgap of InGaAs material is 0.74 eV at room temperature, corresponding to a wavelength of 1.675 μm, so the lasing wavelength will be close to the 1.55 μm telecommunication wavelength[47]. The highly doped InGaAsP-1.25 is the p contact layer with a bandgap energy corresponding to emission at 1.25 μm wavelength. In a real device, the area of top contact will be much smaller than bottom contact, so n contact is placed as top contact to reduce total contact resistance since the specific contact resistance

of n-contact on InGaAs is usually one order lower than that of p-contact[48].

Table 3.2 Stacking layer structure of the wafer for nanolaser fabrication

No.	Material	Thickness [nm]	Doping [cm^{-3}]
0	n-InP	50	5×10^{18}
1	n-InGaAs	100	$2\sim3\times10^{19}$
2	n-InP	50	$>5\times10^{18}$
3	n-InP	150	5×10^{18}
4	n-InP	200	1×10^{18}
5	$In_{0.53}Ga_{0.47}As$	300	Not intentionally doped
6	p-InP	100	1×10^{18}
7	p-InP	100	5×10^{18}
8	p-InP	1000	$>5\times10^{18}$
9	p-InGaAsP-1.25	80	2×10^{19}
10	p-InP	120	$>5\times10^{18}$
11	InP	substrate	Semi-insulating

3.4 Device fabrication

In this section, I will show in detail the fabrication process for metallic cavity nanolasers, which is illustrated in Fig. 3.2a-u. I always use a quarter of a 2-inch wafer in one fabrication run. The whole fabrication includes six stages: wafer preparation, device pillar definition, pillar etching, SiN deposition, silver deposition and finally contact formation.

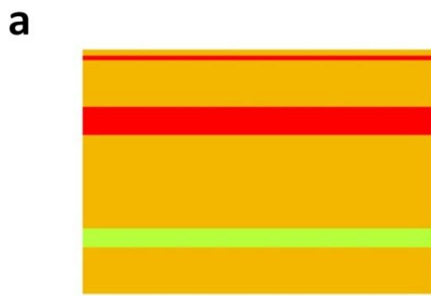

(**a**) Clean sample

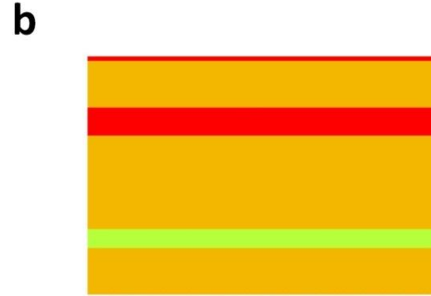

(**b**) Remove top InP layer

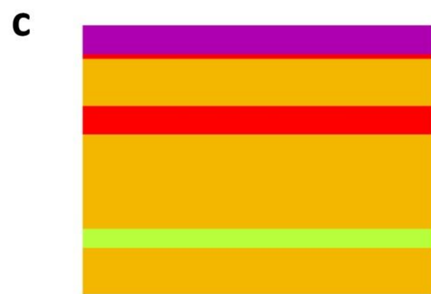

(**c**) Deposit 400 nm SiO_2

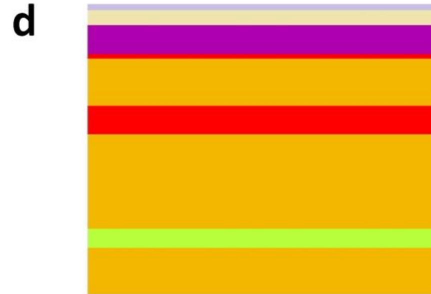

(**d**) Spin-coat HPR-504/HSQ resist

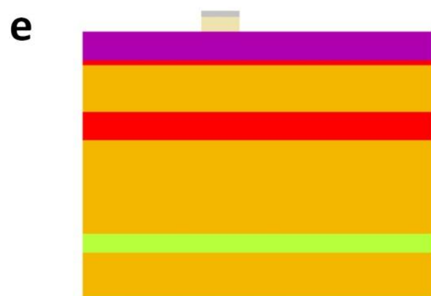

(**e**) EBL expose and dry etch HPR-504 resist

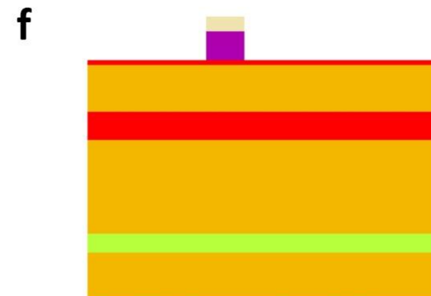

(**f**) Dry etch SiO_2

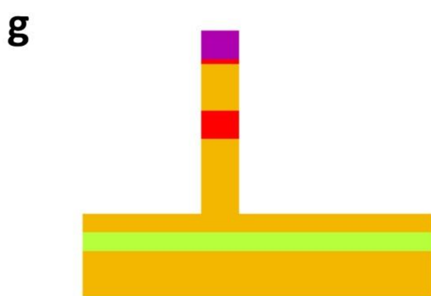

(**g**) Dry etch InP/InGaAs pillar

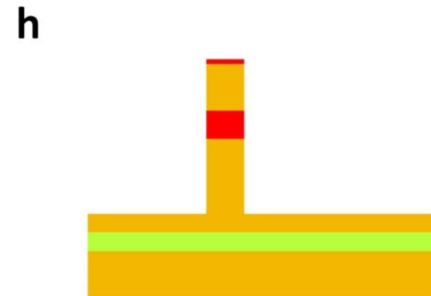

(**h**) Clean surface and remove SiO_2

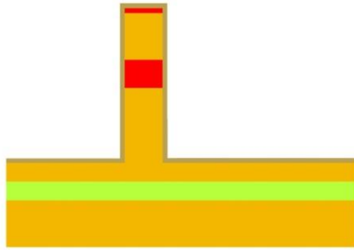

(i) Deposit SiN

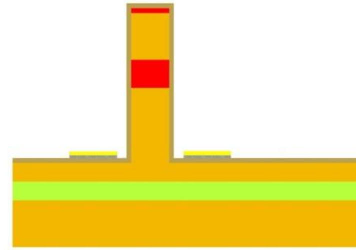

(j) fabricat Ti/Au adhesion layer

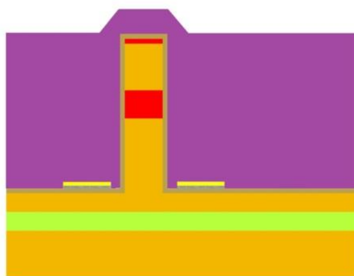

(k) Spin-coat negative photoresist

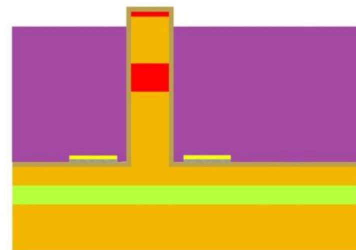

(l) Etch back photoresist

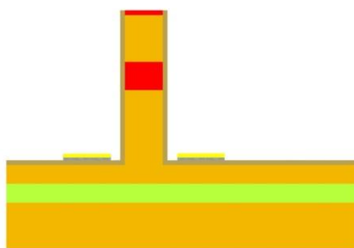

(m) Dry etch SiN on top of pillar

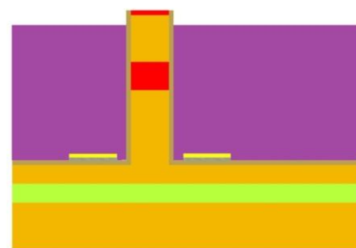

(n) Do second planarization

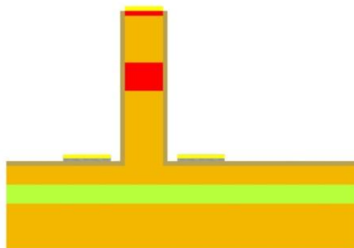

(o) Deposit top contact metal and lift-off

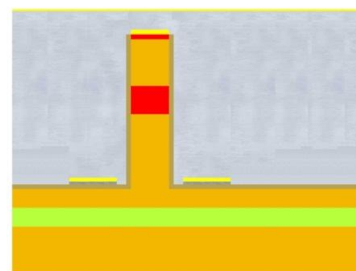

(p) Deposit silver and gold

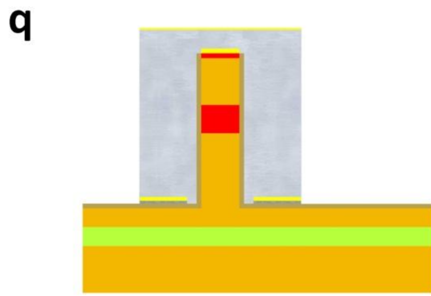

(q) Wet etch silver pad

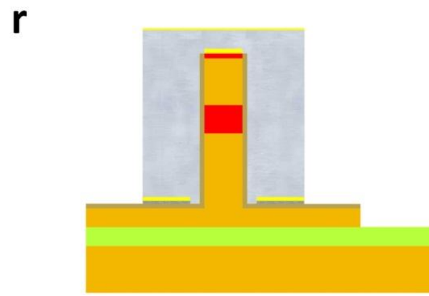

(r) Define p contact and wet etch SiN/InP

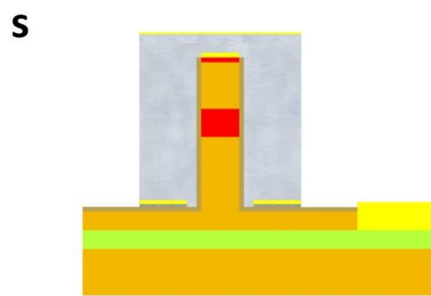

(s) Deposit p contact metal

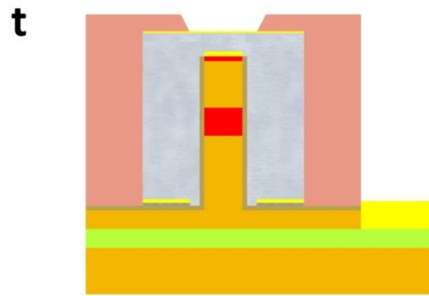

(t) Spin polyimide/open contact windows

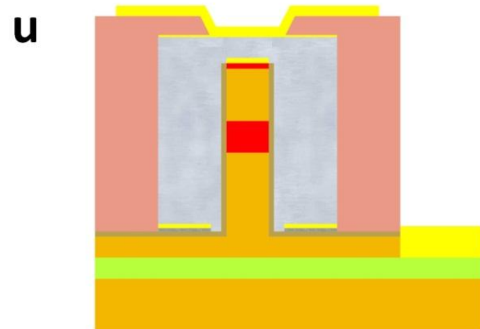

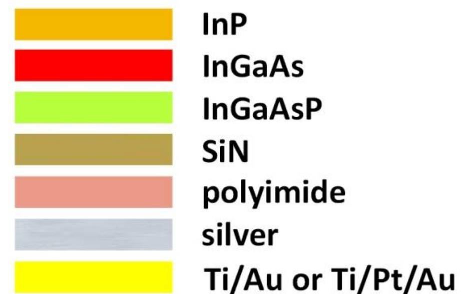

(u) Fabricate top contact pad

Figure 3.2 Device fabrication procedures

3.4.1 Wafer preparation: Fig. 3.2a-c

First the sample is treated by oxygen (O_2) plasma for 10 min to remove any organic contamination on the surface. Photoresist MAN-440 is brushed to the backside of the sample and baked at 100°C for 33 min to protect the backside. Then the sample is dipped in diluted phosphoric acid (H_3PO_4: H_2O=1:10) to remove the oxidized layer on the top surface formed during the O_2 plasma treatment. InP wet etching (H_3PO_4: HCl=4:1) is used to remove the top InP layer (layer No. 0) and the etching will stop at InGaAs layer (layer No. 1). Photoresist at the backside of sample is washed away by acetone and isopropyl alcohol (IPA) rinsing. The same O_2 plasma/diluted phosphoric acid treatment is applied again to clean sample surface. Then 400 nm SiO_2 is deposited via plasma enhanced chemical vapor deposition (PECVD) at 300°C.

3.4.2 Device definition: Fig. 3.2d-e

Due to small feature size of nanolasers pillar, EBL is used to define the device pillar pattern. Photoresist HPR-504 and hydrogen silsesquioxane (HSQ) electron beam resist are successively spun on the sample. After hard baking, the thicknesses for two layers are 450 nm and 80 nm respectively. Before EBL exposure, a 7.5 nm gold layer is deposited at the bottom part of the sample, away from the patterning area, to facilitate the focusing of electron beam. The EBL exposure is performed in a Raith 150 system. After the exposure, KI-I_2 gold etchant is used to remove the gold layer on the sample and then HSQ is developed in a tetramethylammonium hydroxide (TMAH) based developer. HSQ is a negative tone resist so exposed HSQ will remain on the sample after development. Then

the HPR-504 resist underneath is dry etched in O_2 reactive ion etching (RIE) using HSQ as mask, thus the HSQ pattern is transferred to the HPR-504 resist layer. Figure 3.3 shows the scanning electron microscopy (SEM) image of a HPR-504/HSQ bilayer resist pattern after development and RIE etching.

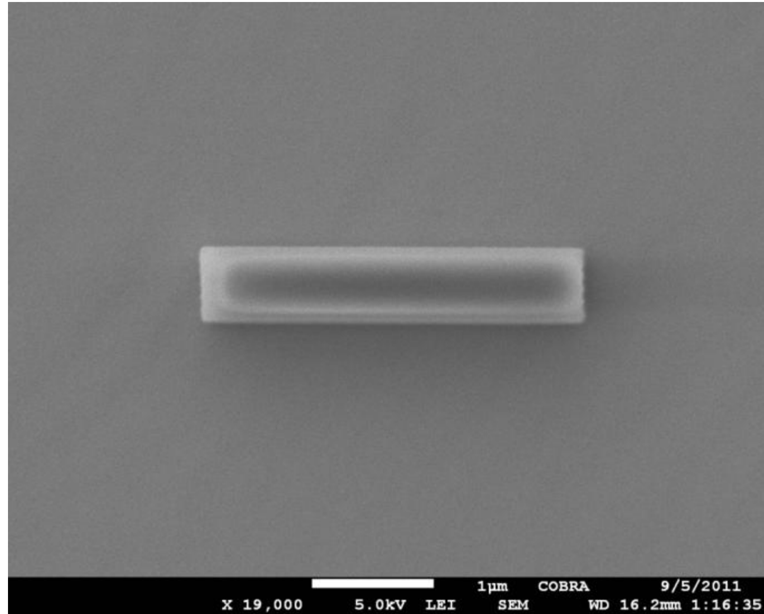

Figure 3.3 HPR-504/HSQ pattern fabricated after EBL exposure, development and RIE etching

3.4.3 Etching and cleaning: Fig. 3.2f-i

Dry etching process is employed to etch the semiconductor pillar. First, the SiO_2 layer is etched in CHF_3 RIE using HPR-504 resist as the mask. The HSQ layer will be etched during this step as well since the composition of HSQ is mainly SiO_2. Then the sample is dipped in diluted hydrofluoric acid (HF) for a short time to remove any HSQ residue. An O_2 plasma/diluted H_3PO_4 treatment is used again to clean sample and remove HPR-504 resist before sending the sample to inductively coupled plasma reactive ion etching (ICP-RIE). During ICP-RIE etching, a number of cycles of CH_4/H_2 etching followed by an

O_2 descum, are executed to etch the InP/InGaAs pillar with SiO_2 as the hard mask. Before etching the main sample, several etching runs on test samples will be performed to optimize the etching parameters and select appropriate number of etching cycles so that desired etching depth (usually 1.6 - 1.7 μm) can be reached on main sample. A number of O_2 plasma/dilute H_3PO_4 treatments are conducted to remove the damaged material on the pillar surface after ICP etching. During this cleaning process, the SiO_2 will be removed by 10% HF. Figure 3.4 shows the SEM image of cleaned InP/InGaAs/InP pillar.

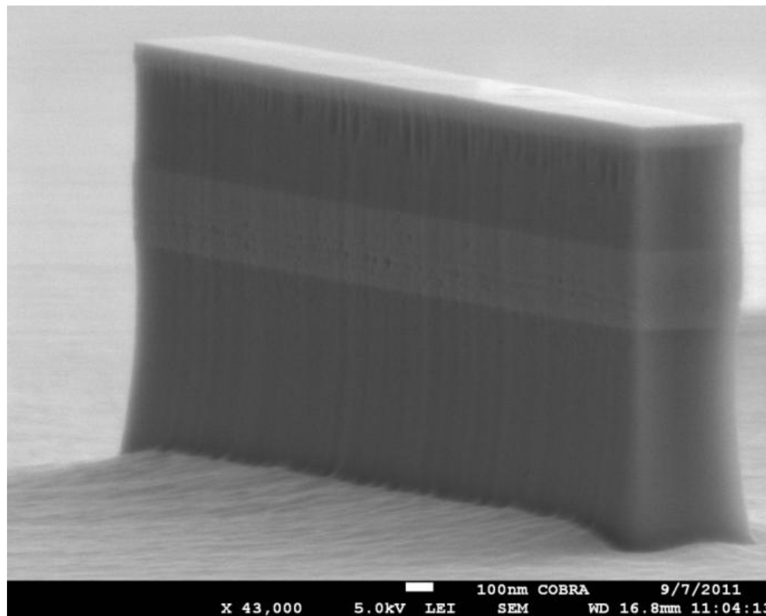

Figure 3.4 SEM image of a cleaned InP/InGaAs/InP pillar

After the surface damaged is removed, SiN layer will be deposited using plasma enhanced chemical vapor deposition. The first 8 nm SiN is deposited at 30˚C to passivate the semiconductor surface states and then another 22 nm SiN is deposited at a higher temperature of 200˚C to provide strong enough electric insulation.

3.4.4 Silver deposition: Fig. 3.2j-q

Since silver itself does not stick well to III-V semiconductor or SiN, an additional adhesion layer between silver and sample substrate is necessary. For this purpose, a rectangular adhesion pad consisting of Ti (50 nm)/ Au (40 nm) is created surrounding each individual pillar through photolithography, metal deposition and lift-off process.

Up to this point, the pillar is cover by SiN layer on all sides, so a top contact needs to be created before encapsulating the pillar in silver to enable electrical injection. Negative photoresist MAN-415 is spun on the sample and soft baked. Then the photoresist is etched back slowly in developer until the top part of semiconductor pillar is exposed while keeping the rest of the pillar buried in photoresist. This process is referred to as planarization. The height of exposed pillar will be monitored in profilometer so it can be well controlled to around 250 nm. SiN on top of the pillar will be removed in a CHF_3/O_2 based RIE. Photoresist left on the sample is washed away in acetone and IPA. After another planarization, Ti (20nm) / Pt (15nm) / Au (15nm) layer is deposited by electron beam evaporation. Ti/Pt/Au contact metal is left only on the top the semiconductor pillar after lift-off, thus forming the n-contact of device. Figure 3.5 shows the SEM image of a pillar with SiN on all sides and Ti/Pt/Au on its top. Occasionally, photoresist in the second planarization is over etched and some upper part of the pillar is exposed as well, so there will be extra Ti/Pt/Au particles deposited on the sidewall of the pillar as shown in Fig. 3.5. Such Ti/Pt/Au particles will introduce extra metal loss since they are high loss metal compared to silver and so over etch of photoresist needs to be carefully avoided.

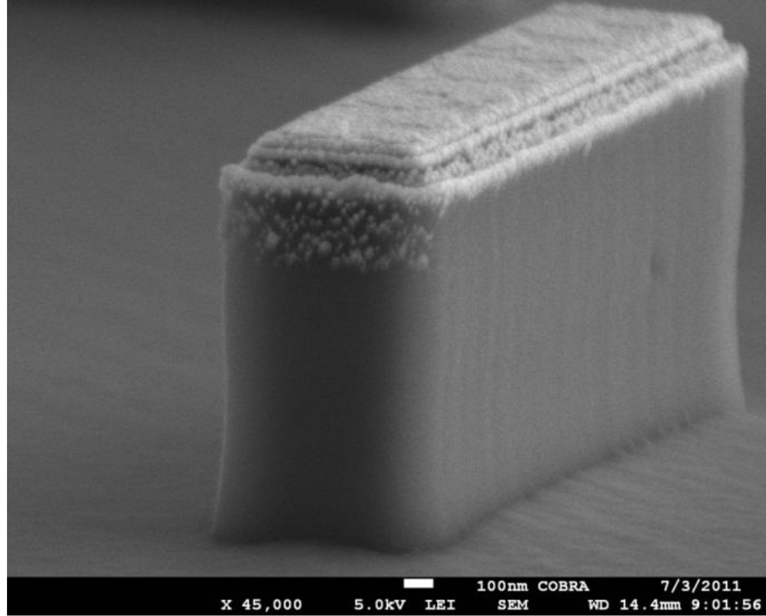

Figure 3.5 SEM image of a pillar with SiN coated on the side and top contact metal

1 μm of silver is deposited to the substrate by thermal evaporation. During the deposition, the sample is tilted to a 15 degree angle with respect to the vertical direction and rotated continuously (Fig. 3.6a) to cover the pillar sidewall uniformly. Then sample is annealed at 400 ℃ by rapid thermal annealing (RTA) for 1min to promote a solid adhesion between silver and Ti/Au pad. Additionally, RTA helps to improve silver quality by increasing crystalline grain size and to improve SiN passivation to reduce surface recombination at the InGaAs/SiN interface. I will discuss these two functions in a later section of this chapter. SEM image of this silver coated pillar (Fig. 3.6b) shows the grain sized can be up to 1 μm. After annealing, another 1 μm of silver is deposited in the same manner but at a 60 degree angle to cover the top of the pillar and base. A further 100nm gold layer is sputtered to protect silver. Photolithography and wet etching in KCN (for gold) and $NH_4OH:H_2O_2:H_2O$ (for silver) is executed to remove metals outside silver device pad.

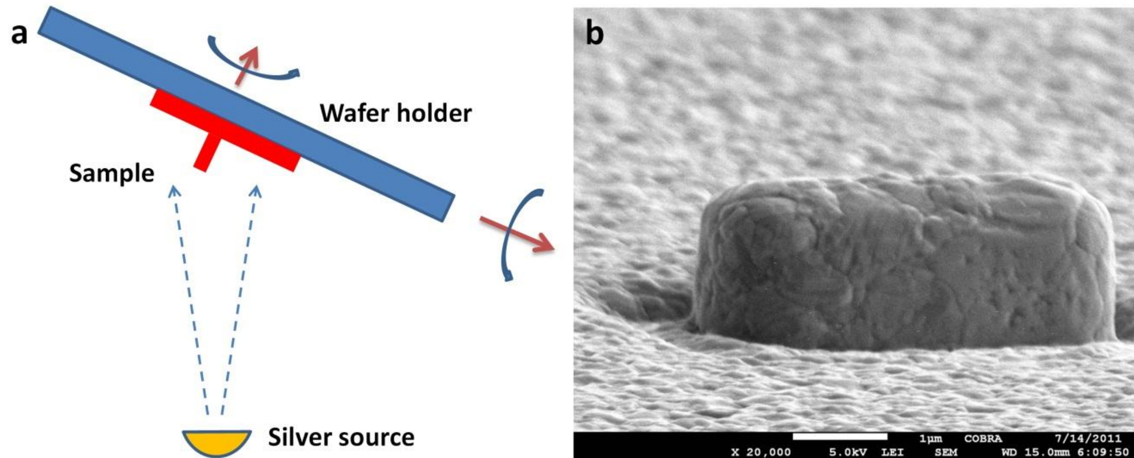

Figure 3.6 **(a)** Schematic of silver deposition. The wafer holder can be rotated in two directions freely in order to deposit silver uniformly. **(b)** SEM image of a pillar coated with silver after annealing. The silver grain size can be up to 1 μm.

3.4.5 Contact formation: Fig. 3.2 r-u

The area of p-contact is defined by photolithography. The SiN on the area of p-contact is etched in buffered HF (NH_4F:HF). Wet etching (H_3PO_4: HCl = 4: 1) is used to etch InP through to the InGaAsP layer (Layer No. 9). Ti (65nm)/ Pt (75nm)/Au (200nm) layer is deposited and the p-contact is formed after lift-off process.

A photosensitive polyimide PI3727 layer is spun on the sample to form the mesa for n-contact pad. Photolithography is performed on this polyimide layer to open the windows for p-contact and device pad. After regular photolithography, metal sputtering and lift-off process, the n-contact pad is formed with metal layer Ti (50 nm)/ Au (200 nm) and fabrication for laser devices is finished here.

3.5 Packaging

After fabrication, the sample is cleaved into small bars containing 5 devices on each

piece as shown in Fig. 3.7a. Gold wires (diameter 40 μm) are glued to the n-contact pads by silver epoxy. Then a copper block is mounted to the common p-contact pad by silver epoxy as well. Then the copper block is flipped over and mounted to a ceramic dual inline package. A gold wire is glued to the copper block as well. Afterwards, all gold wires are glued to the pins on the package so that the device can be connected to external electric source via the pins on the package. In this manner of packaging, light emission from device can be collected from the backside of sample as shown in the Fig. 3.7b. A picture of packaged sample bar is presented in Fig. 3.8.

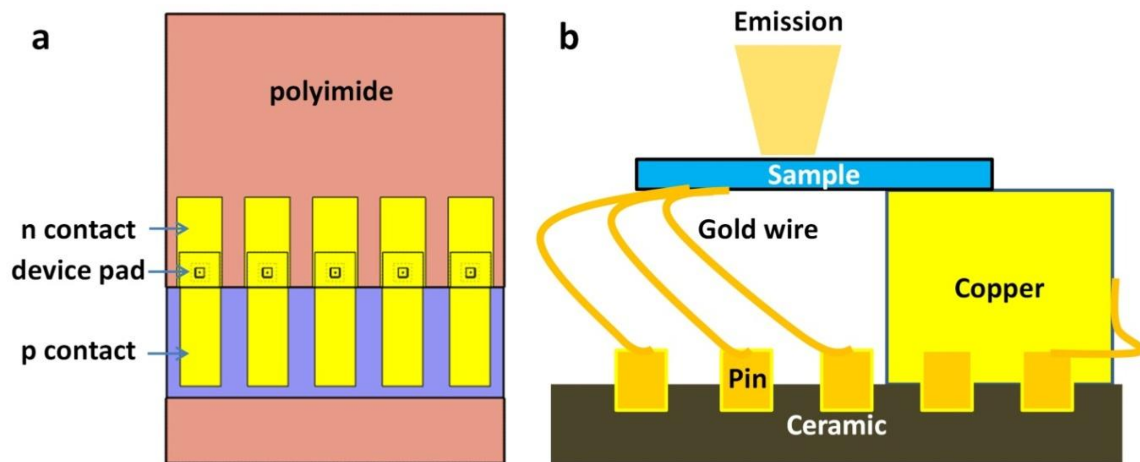

Figure 3.7 **(a)** Schematic of a sample bar containing 5 individual devices. **(b)** A sample bar flipped over and mounted to ceramic package by a copper block and gold wires.

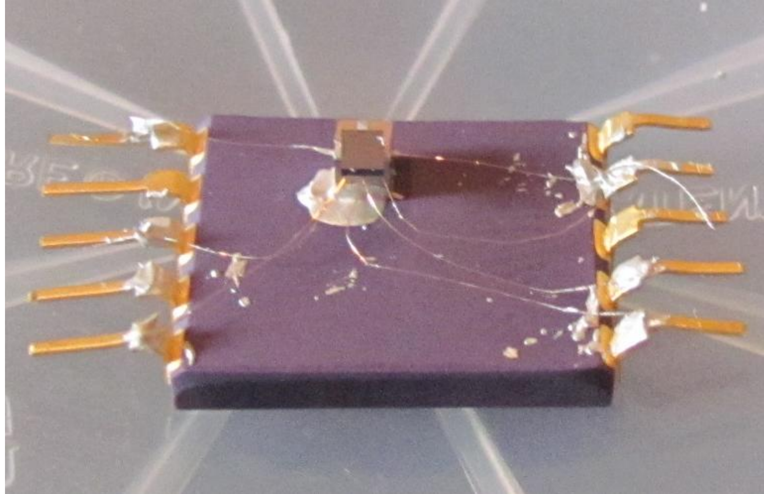

Figure 3.8 Picture of a device bar mounted on a ceramic package by copper block and gold wires

3.6 Critical steps in nanolaser fabrication

In this section, I will discuss several steps in nanolaser fabrication that I found critical to device performance. Two of the key factors that will determine the final device performance of nanolasers are associated with device fabrication. One is the Q factor of metallic cavity, and the other is surface recombination. Due to the use of lossy metal, metallic nanocavity is generally a low Q cavity. What is worse, any imperfection in fabrication can severely degrade cavity even further because of cavity's sub-wavelength scale. Therefore special attention must be paid to several fabrication steps including EBL, pillar dry etching and silver deposition, which will influence cavity Q factor. The other is surface recombination. The surface of InP/InGaAs pillar must be well passivated to reduce surface recombination otherwise a large amount of injected carriers will be consumed by high surface recombination which will significantly increase laser threshold. All the fabrication steps discussed in this section are related to these two issues.

3.6.1 EBL

Optical loss induced by scattering at the dielectric/metal interface[49] can be significant in such nanocavity device due to its large surface area/volume ratio. Such scattering is particularly crucial in narrow waveguide type of devices supporting the plasmonic gap mode where optical field is strongly localized in the thin SiN layer between semiconductor and silver. Therefore a smooth semiconductor pillar surface is desired to reduce optical scattering loss and improve cavity Q factor.

In my first generation of nanolaser, lift-off process is employed in device pattern definition. After deposit 400 nm SiO_2 by PECVD, Poly methyl methacrylate (PMMA) EBL resist is spun on the wafer. PMMA is a positive tone resist, so after development, exposed resist will be washes away. Then 50 nm chromium mask is fabricated through metal evaporation and lift-off process. In the second generation of nanolasers, I used the HPR-504/HSQ bilayer resist EBL to improve pattern edge smoothness. Compared to PMMA resist, HSQ resist has two major advantages. First, HSQ is a resist with small molecular size and it pattern edge roughness can be under 2 nm[50], significantly smaller than polymer based resist such as PMMA and ZEP. Also HSQ is a high-resolution resist capable of defining patterns as narrow as 10 nm[51]. What is more important, HSQ is a negative tone resist, eliminating the need for metal lift-off process to invert resist pattern to metal. Metal lift-off is a process with flaw in nature by introducing extra roughness at the metal boundary. The roughness of metal boundary will affect the following semiconductor pillar etching process and roughen the pillar surface, thus increasing the loss in the cavity.

In HSQ EBL, HSQ pattern is transferred to photoresist and SiO_2 hard mask through RIE process. The RIE dry etching will not introduce significant extra roughness to device pattern thus leads to improved pattern quality. A comparison between patterns created by PMMA/metal lift-off process and HSQ/RIE process is shown in Fig. 3.9. Apparently, a pattern defined in HSQ EBL has much smoother edges than a metal pattern made by PMMA EBL and metal lift-off.

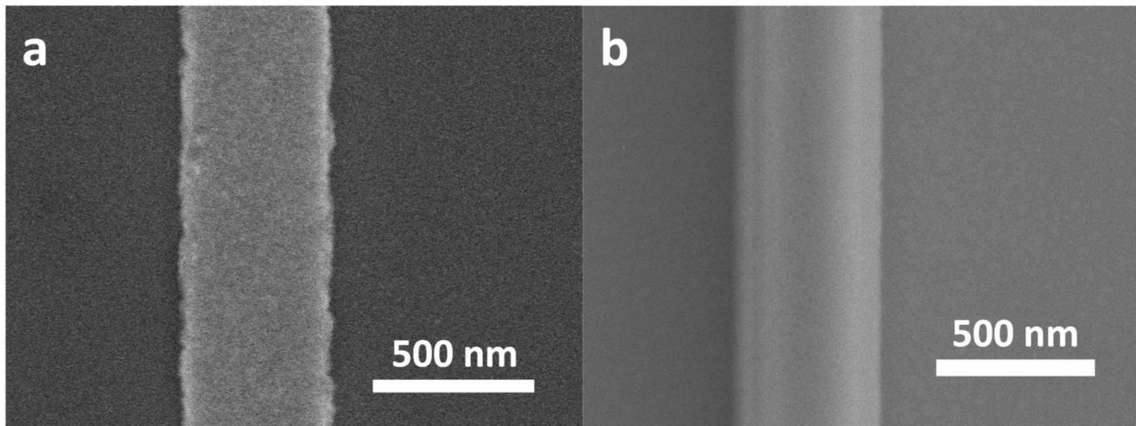

Figure 3.9 400nm wide strip pattern made by EBL with **(a)** PMMA resist and metal lift-off and **(b)** HPR-504/HSQ bilayer resist and RIE.

3.6.2 Pillar etching

Due to various non-ideal factors (e.g. SiO_2 mask erosion[52]) in the CH_4/H_2 dry etching process, the sidewall of the InP/InGaAs/InP pillar is not perfectly vertical in general and will tilt at a small angle as shown in Fig. 3.10a. The effects of such sidewall tilting can be examined in FDTD simulation. Simulated Q factor as a function of sidewall tilting angler for the TE01 mode in a circular metallic cavity nanolaser with radius of 200 nm is shown in Fig. 3.10b. A sidewall tilting as small as 2-degree can fatally degrade device cavity Q, imposing strict precision requirement on device fabrication. To understand the

degradation of Q due to the sidewall tilting, the optical field intensity ($|E|^2$) in the cavity is shown in Fig. 3.11. When the sidewall is perfectly vertical (θ=0, Fig. 3.11a), the optical field is well confined in the InGaAs layer. However, if the sidewall is tilted by 2 degree (θ=2, Fig. 3.11b), the optical field will leak into the bottom InP cladding layer, leading to a large radiation loss and a severe degradation in cavity Q factor.

In real fabrication, I also perform several ICP etching runs on test samples before etching the real sample. During those test runs, I will optimize the processing parameters, such as pressure and O_2 descum time, to restrict the sidewall tilting angle within 1 degree. Figure 3.12 shows an example of ICP etched pillar. The sidewall is quite straight until the very bottom of InP section.

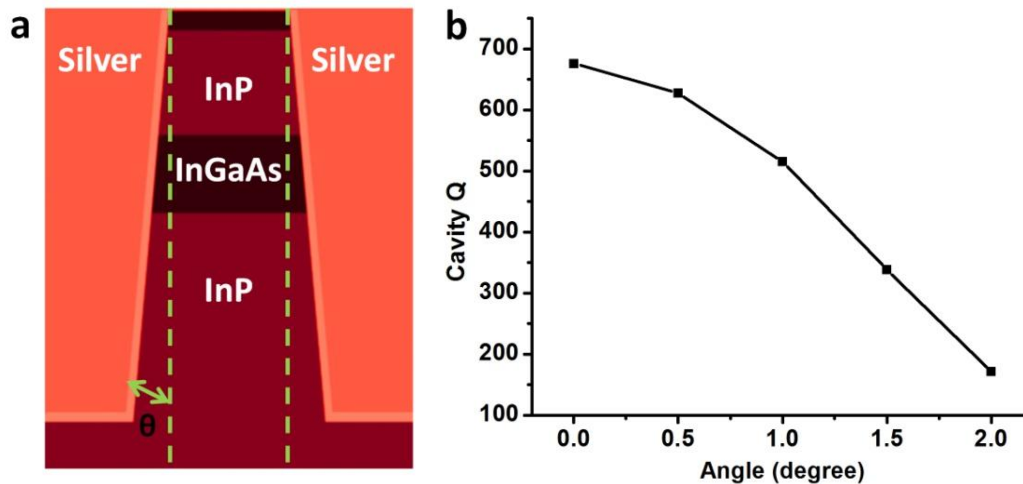

Figure 3.10 **(a)** Schematic of a device with tilted sidewall. **(b)** Cavity Q (TE_{01} mode in a circular device with radius of 200nm, Johnson and Christy[26] silver used) as a function of sidewall angle θ.

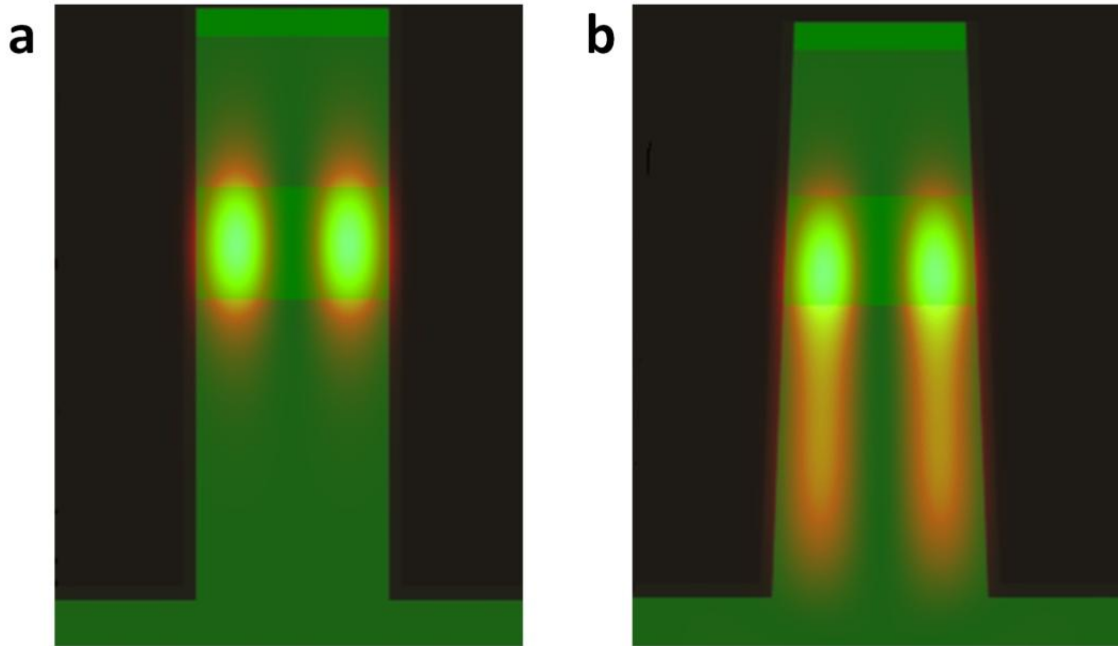

Figure 3.11 Optical field ($|E|^2$) of TE_{01} mode in cavities with **(a)** straight sidewall and **(b)** tilted sidewall

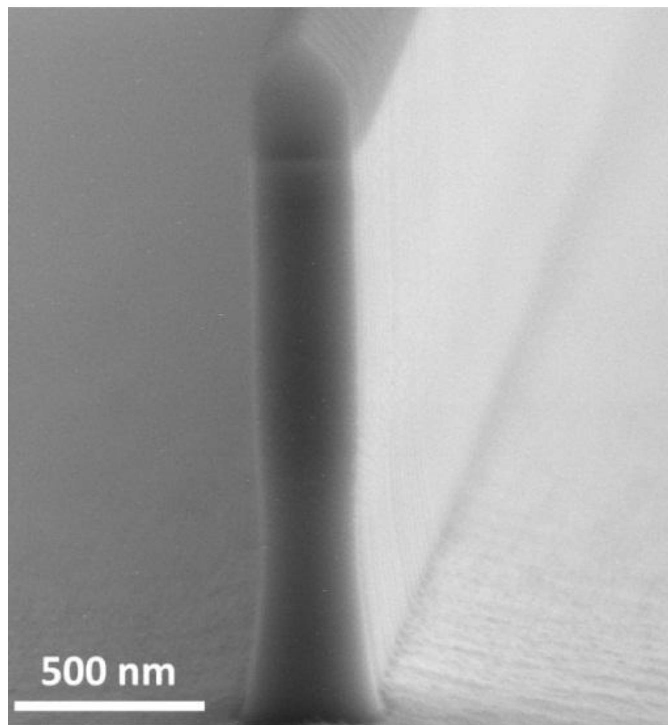

Figure 3.12 SEM image of an InP/InGaAs/InP pillar etched by ICP RIE with optimized processing parameters

3.6.3 Surface cleaning and passivation

Another surface related issue in nanolasers is the surface recombination (SR). The surface recombination velocity (SRV) in InGaAs is $1\text{-}2\times10^5$ cm/s [53,54] in general without good passivation, leading to a short SR lifetime in nanocavities. For example, the SR lifetime in a circular nanolaser with radius around 200 nm is estimated to be 0.1-0.05 ns by:

$$\tau = \frac{R}{2\upsilon_{SR}} \tag{3.1}$$

where R is the radius of semiconductor pillar and υ_{SR} is the SRV.

How to reduce the surface recombination includes two aspects: first, surface damage induced by CH_4/H_2 dry etching needs to be removed; second, the semiconductor surface needs to be effectively passivated by dielectric material. As mentioned in Section 3.4.3, I performed thorough oxygen plasma and dilute H_3PO_4 treatment to remove the damaged layers on the InP/InGaAs/InP pillar surface after ICP dry etching. SiN layer then is deposited using plasma enhanced chemical vapor deposition. The first 8 nm SiN is deposited at 30°C to passivate the semiconductor surface states and the other 22 nm SiN is deposited at a higher temperature of 200°C to provide strong enough electric insulation.

Specific experiment is designed to examine the effects of those processes to SR. An InGaAs/InP grating structure shown in Fig. 3.13 is fabricated using the CH_4/H_2 ICP RIE. The total grating area is 200 μm × 200 μm, with period of 1 μm and pillar width at 200 nm. The height of the pillar is around 1.3 μm, similar to the height of nanolaser pillar. I perform photoluminescence (PL) measurement on this grating structure using a 632 nm

wavelength laser. InP and InGaAs are not doped here. Unlike doped p-i-n junction, there is not built-in electric field in this intrinsic material and therefore the photo-generated carriers will not drift away but recombine in the InGaAs layer with photon emission at the energy of bang gap. Due to the small width of etch pillar, its PL intensity will be determined by SR[55]. The smaller the SR, the stronger the PL intensity is. The PL intensity after each process step is plotted in Fig. 3.14. Initially, the un-etched wafer (step 1) shows strong PL emission due to good material quality. After etching (step 2), PL intensity from the grating structure drops to about half of the wafer value due to reduced active material and increased surface area. But there is still quite strong emission from such newly etched grating structure, suggesting that the polymer generated during the dry etching can somehow passivate the surface states. After O_2 plasma treatment (step 3), the PL intensity drops to nearly zero since the polymer is removed by O_2 plasma and the semiconductor surface is oxidized. A large amount of surface states at the oxidized surface will consume most of the photo-generated carriers, resulting in weak PL emission. Then I remove this oxidized surface layer in dilute H_3PO_4 (step 4) and the PL intensity is restored. After depositing SiN layer (step 5) to coat the surface, PL intensity drops to a low level again but recovers after a rapid thermal annealing (RTA) at 400°C for 60s (step 6). This RTA will be performed after silver deposition in real nanolaser fabrication to improve silver crystal quality and promote silver adhesion with Ti/Au adhesion pad. Through this PL measurement, it can be seen that the third function of RTA is to improve surface passivation with SiN. The final PL intensity is close to the intensity for un-etched bulk

material, indicating that the cleaning and SiN deposition process can effectively remove the dry etching damage on pillar surface and passivate the surface states.

In nanolaser fabrication, the O_2 plasma/diluted phosphoric acid treatment is performed for several (7-9) times to remove the damaged layer thoroughly. One issue worth mentioning is that the diluted phosphoric acid etching must be carried out in dark environment; otherwise the surface of pillar will be very rough after etching. Figure 3.15 shows the SEM images of InP/InGaAs/InP pillar after cleaning under room light and in dark. If wet etching is done under room light (Fig. 3.15a), there will be bumps on the surface while smooth surface is obtained if etched in dark (Fig. 3.15b). There could be photo-assisted electric-chemical reaction at the surface related to the photo-generated current in the InP/InGaAs/InP p-i-n junction under illumination[56], which can cause a rough surface.

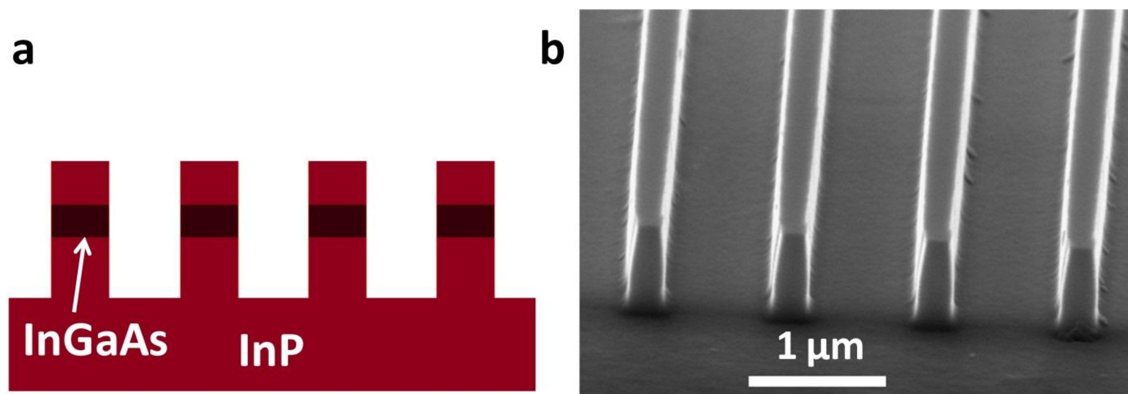

Figure 3.13 **(a)** InP/InGaAs/InP grating structure used in PL measurement and **(b)** its SEM image

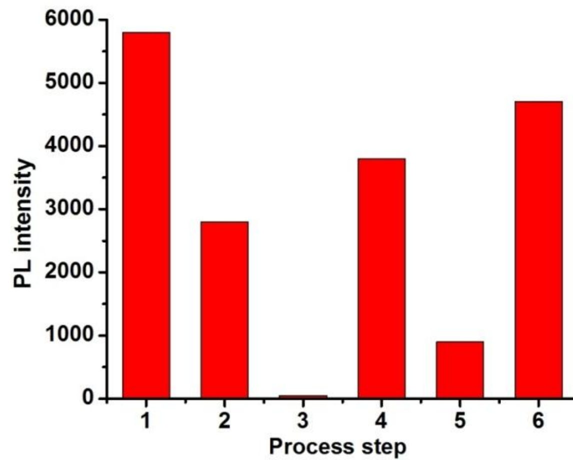

Figure 3.14 PL intensity of test grating structure after different process steps. 1) Un-etched. 2) Dry etched. 3) O_2 plasma treated. 4) Dilute H_3PO_4 treated. 5) SiN deposited on surface. 6) Thermally annealed.

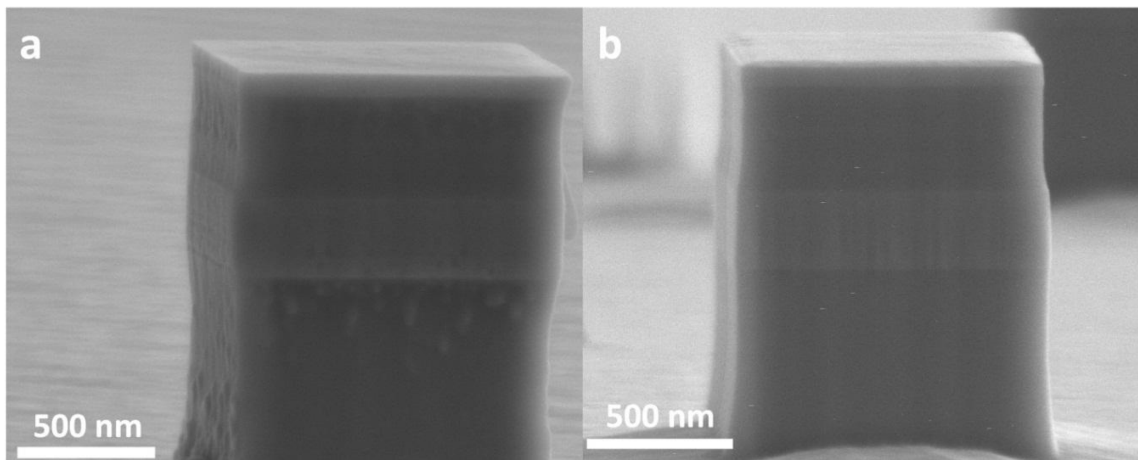

Figure 3.15 SEM images of InP/InGaAs/InP pillar after cleaning **(a)** under room light, **(b)** in dark.

3.6.4 Silver deposition

Ohmic loss in metal is the major loss source in metallic nanocavities. One representative quantity to evaluate ohmic loss in metal is the metal dielectric constant. In practice, measured silver dielectric constant, especially its imaginary part, varies widely in literature, which is summarized in Fig. 3.16. Through FDTD simulation, I calculated the

Q factors of the TE_{01} mode in a circular nanolaser with a 200 nm radius. As shown in Fig. 3.17, cavity Q from simulation can be significantly different depending on the silver dielectric constants used. I believe this large variation in silver dielectric constant can be attributed to silver crystal quality which is determined by the specific deposition techniques used. Therefore special attention should be paid to silver deposition process to obtain silver with good crystal quality.

To investigate this silver quality issue, I first look into the Drude model for metal dielectric constant.

$$\varepsilon(\omega) = \varepsilon_{\infty} - \frac{\omega_p^2}{\omega^2 + j\omega\gamma} \tag{3.2}$$

As discussed in Chapter 2, ω_p is metal plasma frequency, γ is electron damping rate. I fit silver dielectric constant with Drude model and get γ for silver from different sources. As shown in Fig. 3.17, cavity Q factor is roughly inversely proportional to γ, so one of the keys to increased cavity Q factor is to reduce electron damping rate γ, which represents metal ohmic loss. Theoretical study and experiment report both indicate that γ is related to metal crystal grain size.

Generally γ can be divided into three parts[58]: electron-electron collision (υ_{ee}), electron-phonon collision (υ_{ep}) and electron collisions at defects and metal grain boundaries (υ_{ed}) or $\gamma = \upsilon_{ee} + \upsilon_{ep} + \upsilon_{ed}$. Obviously the last term υ_{ed} is related to metal crystal quality and grain size. The better metal crystal quality and larger grain size, the smaller υ_{ed} is and therefore the lower metal Ohmic loss is. Even though there is no separate value

for the υ_{ed} published in literature, the influence of υ_{ed} should be significant. The values of reported imaginary part of silver permittivity vary widely from the smallest of ~3.4 (at 1.5 μm wavelength) by Johnson & Christy[26] to ~ 11.10 reported by Winsemius *et al*[38]. Since υ_{ee} and υ_{ep} are more intrinsic properties of metals such as band structure, Fermi level, electron density and temperature, such large variation can only be attributed to the difference in υ_{ed}, or metal crystal quality and grain size. Thus, it can be concluded that υ_{ed} has significant influence on the imaginary part of silver permittivity. By improving metal crystal quality and grain size, υ_{ed} can be reduced, leading to the reduction of γ and the metal Ohmic loss. A more direct measurement of the grain size effect in metal loss is reported by Kuttge *et al*[59]. They measured the SPP propagation length on different forms of gold: single crystal, gold films with 80 nm grain size and 20 nm grain size. At 700 nm wavelength, SPP propagation lengths on single crystal, 80 nm-grain-size, 20 nm-grain-size gold are 74 μm, 18 μm, 3.6 μm respectively, strongly depending on metal crystal quality and grain size. Since the propagation length is directly related the metal Ohmic loss, it is quite clear that metal Ohmic loss can be reduced by improving metal crystal quality and grain size. Though Kuttge's experiment was performed on gold at shorter wavelength (600 nm ~ 750 nm), the same mechanism is also applicable to silver at longer wavelengths.

In my fabrication, it was found that deposition rate and post RTA are the two key factors related to silver grain size. The optimized deposition process includes a relatively fast deposition rate at 4 nm/s in a thermal evaporator and a RTA at 400°C for 60 s. The

obtained silver grain size can be up to 1μm (see Fig. 3.6b). For a device with submicron dimensions, this silver behaves almost as single crystal and that is probably the best silver that can be obtained in our cleanroom.

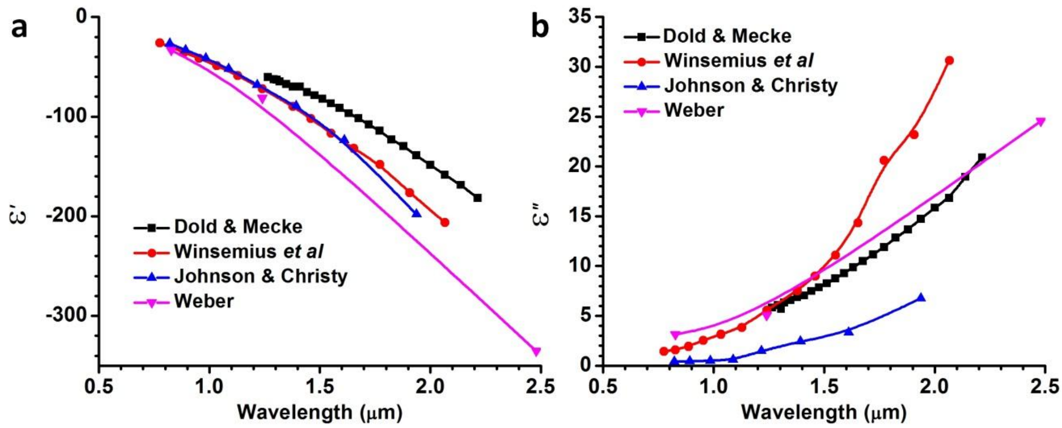

Figure 3.16 Measured dielectric constant of silver: **(a)** real part and **(b)** imaginary part from different sources: Dold and Mecke[37], Winsemius *et al*[38], Johnson and Christy[26], Weber[57].

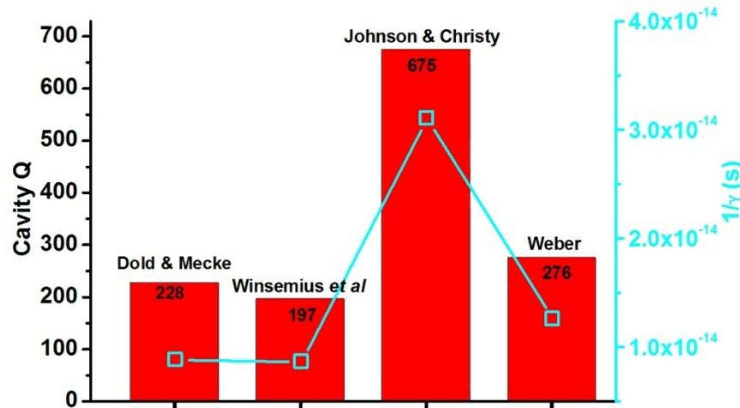

Figure 3.17 Device cavity Q obtained in the simulation using different silver dielectric constants. Cavity radius is set to 230 nm, supporting TE_{01} mode. Hollow square ☐ is inversed electron damping rate γ for different silver data extracted by fitting with Drude model.

3.7 Summary

In this chapter, I discussed the fabrication process for nanolaser in which EBL, photolithography, wet and dry etching, PECVD dielectric deposition, PVD metal deposition techniques are used. The whole fabrication process is not only complex but also requires precision for good device performance. Critical steps in fabrication include EBL, ICP-RIE dry etching, surface cleaning and passivation, and silver deposition, because those steps will strongly influence the optical property (Q factor) and electrical property (surface recombination) of devices. From my experiences, device performance always fall far short of what simulation predicts which I believe can be attributed to the fabrication imperfections. Therefore further development in fabrication techniques, especially the surface passivation and silver deposition techniques to reduce surface recombination and obtain high quality silver, will be the keys to improved device performance.

CHAPTER 4

RECTANGULAR NANOLASERS

4.1 Introduction

In this chapter, I will present my research results on one type of nanolasers with rectangular shape. Modal properties and related polarization measurement results will be presented first. So far, the smallest rectangular nanolaser I fabricated has a deep sub-wavelength physical volume of 0.19 λ^3 (λ = 1454 nm, lasing wavelength in the vacuum). Improving device operation temperature is one of the focuses of my research. Through optimizing device design and fabrication, I demonstrated the world's first continuous wave (CW) sub-wavelength laser under electrical injection at room temperature (RT).

4.2 Waveguiding in MISIM structure

The structure of a rectangular nanolaser is schematically shown in Fig. 4.1. An InP/InGaAs/InP pillar with rectangular cross section is encapsulated in SiN and silver to form a metallic cavity. Dimensions of the rectangular pillar, width (W, in X direction), height (H, in Y direction) and length (L, in Z direction), are indicated in Fig. 4.1 as well. The InP/InGaAs/InP layer forms three-layer sandwich waveguide in the vertical direction. If the cavity is long and thin (long length L and narrow width W), its XY plane can be treated as a metal-dielectric-semiconductor-dielectric-metal (MISIM) waveguide as shown in Fig. 4.2. At near infrared region, silver behaves more like a perfect conductor or

perfect mirror[18], thus confining the optical field in the horizontal direction. Similar waveguides with Metal-insulator-Metal (MIM) structures have been intensively studied both theoretically[60-63] and experimentally [64, 65]. By inserting InP/InGaAs/InP heterostructure in the middle, such MISIM configuration enables compensation for the metal loss by optical gain in the InGaAs layer. The entire structure can be pumped using electrical injection to achieve optical amplification or lasing.

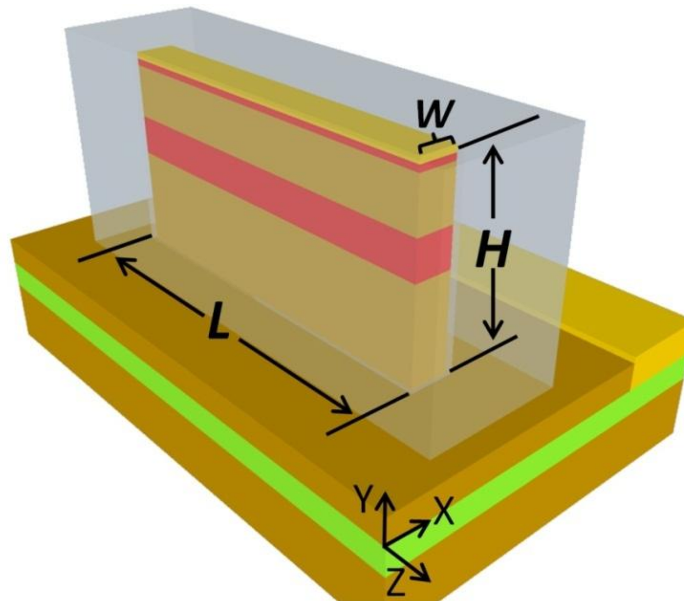

Figure 4.1 Structure of a rectangular metallic cavity nanolaser. Dimensions of the rectangular pillar, width (W, in X direction), height (H, in Y direction) and length (L, in Z direction), are indicated.

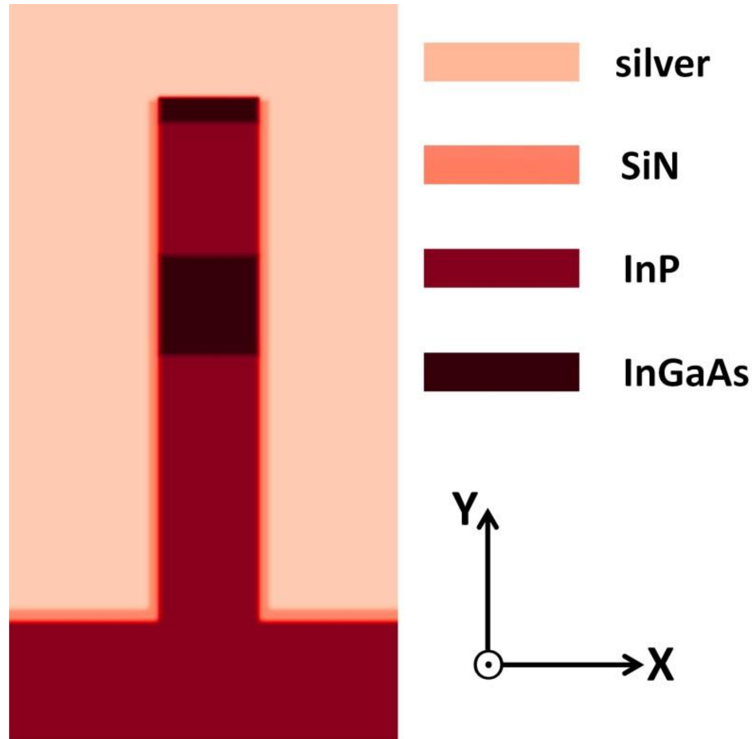

Figure 4.2 Schematic of metal-dielectric-semiconductor-dielectric-metal (MISIM) waveguide in XY plane.

2D simulation is conducted in COMSOL software package, RF module to study the modal property of this MISIM waveguide. Two kinds of mode are supported in this waveguide when the waveguide width exceeds half of the wavelength in the InGaAs gain medium. Figure 4.3 shows the mode pattern (|E|) of the TE-like mode (E_y dominant) and the TM-like mode (E_x dominant).

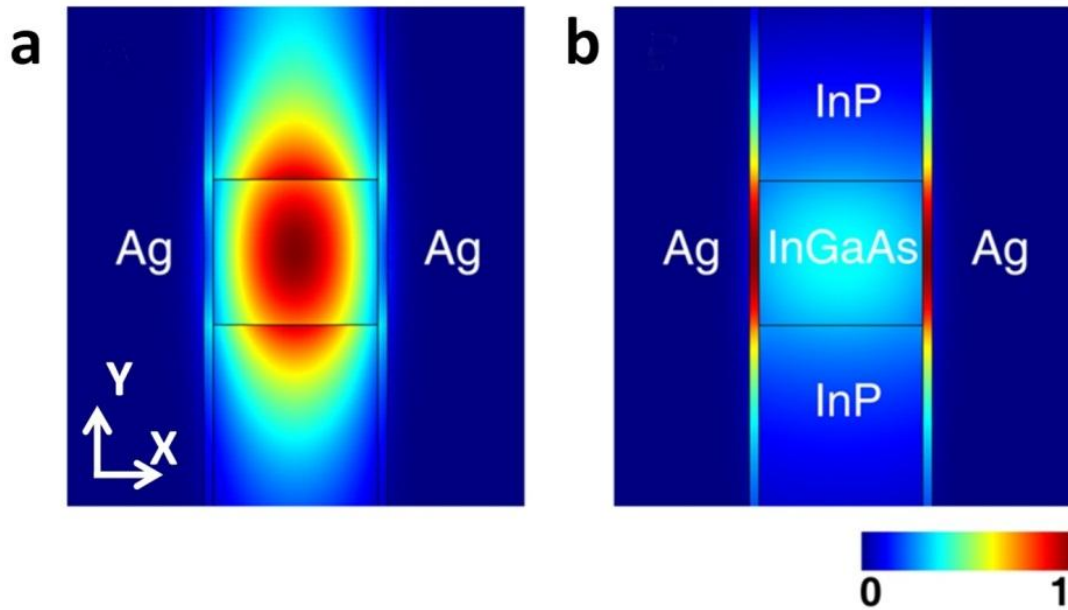

Figure 4.3 Mode |E| patterns of **(a)** TE-like mode, E_y dominant and **(b)** TM-like mode or plasmonic gap mode, E_x dominant.

Propagation loss and mode effective indices of these two modes as function of for semiconductor core width are plotted in Fig. 4.4a (assuming 20 nm SiN layer and wavelength of 1.55 μm). The mode effective index is defined as

$$n_{eff} = real(\beta_z)/\beta_0 \tag{4.1}$$

β_z, β_0 are the wave propagation phase constant in MISIM waveguide (Z direction) and free space respectively.

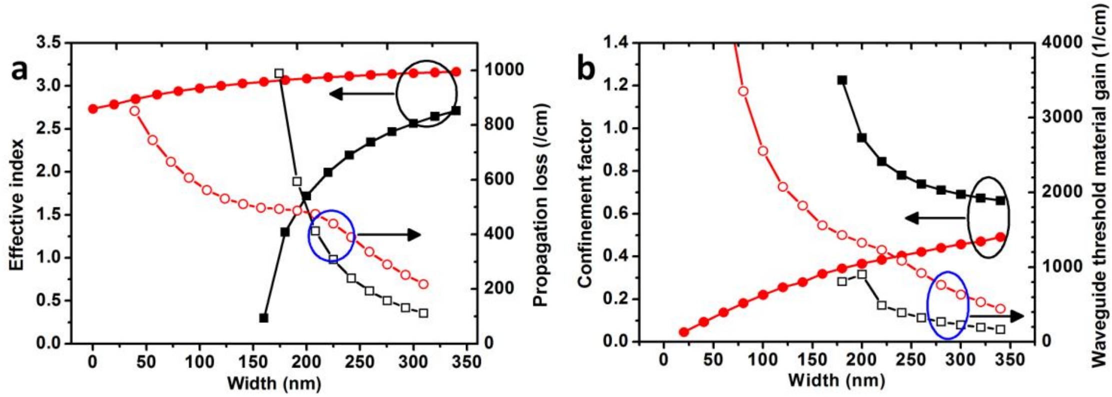

Figure 4.4 **(a)** Mode effective index and propagation loss for TE-like (black symbols) and TM-like (red symbols) modes in MISIM waveguide at 1.55μm wavelength plotted as a function of waveguide core width. TE-like mode has a cut-off width below the diffraction limit ($\lambda/2n_r$) while TM-like mode shows no cut-off. **(b)** Confinement factor defined by (1.1) and waveguide threshold material gain defined by (2.41) for this two modes as a function of waveguide core width.

As shown in Fig. 4.4a, the TE-like mode shows a cut-off around 200 nm (roughly $\lambda/2n_r$, or the diffraction limit) as indicated by a dramatically decreased effective index and increased modal loss. The TM-like mode, or as known as plasmonic gap mode, exists even when the width of the waveguide core approaches zero with a slighted decreased effective index to 2.75. Meanwhile the propagation loss of TM-like increases significantly with the decrease of the core width. Theoretically, such MISIM waveguide can be made arbitrarily thin to support the plasmonic gap mode, thus offering the possibility to overcome the so-called diffraction limit by confine the plasmonic gap mode in MISIM waveguide narrower than the half wavelength limit. Based on this idea, Hill *et al*[12] has demonstrated lasing around 1.36 μm in a MISIM waveguide cavity with 90 nm semiconductor core width and 6 um length at 10 K under DC current injection, supporting a TM_0 plasmonic gap mode.

However, the TE-like mode is a more favorable mode in terms of propagation loss and confinement factor. As shown in Fig. 4.4a, when waveguide width is slightly larger than diffraction limit ~200 nm, the propagation loss of TE-like mode drops dramatically lower than the TM-like mode. Meanwhile, the optical field of TE-like mode is mostly confined in the InGaAs high index region while TM-like mode concentrates in the SiN low index layer between metal and semiconductor. Intuitively, the TE-like mode has a much larger confinement factor than TM-like mode.

The numerical calculation result for confinement factor by (1.1) and waveguide threshold material gain by (2.41) is plotted in Fig. 4.4b. The waveguide threshold material gain for the TE-like mode is much smaller than TM-like mode due to less propagation loss and larger confinement factor. Though the size of such MISIM waveguide supporting TE-like mode is still above the diffraction limit, it provides a trade-off between device size and optical loss, confinement factor, and the threshold gain, thus facilitating the realization of metallic nanolasers with good device performance. Therefore I focus on building nanolasers supporting on this TE-like mode.

It shall be noticed that the confinement factor for TE-like mode can be larger than unity when the waveguide width is close to the cut-off width. As discussed in Chapter 2, this is due to the slowing down of mode energy velocity[27] when it is close to cut-off.

4.3 Metallic nanocavity based on MISIM waveguide

In the rectangular metallic cavity nanolaser, two ends of the pillar are covered by silver as

well. Therefore optical wave is reflected at both ends and bounces back and forth in the length (Z) direction, thus forming a Fabry-Perot cavity. Figure 4.5 shows the standing wave in a metallic nanocavity with a physical dimension of 260 nm (W) $\times$ 1.58 μm (H) $\times$ 4.26 μm (L) in XZ and YZ plane. The propagating mode is the TE-like mode with a Q factor of 287 from FDTD simulation.

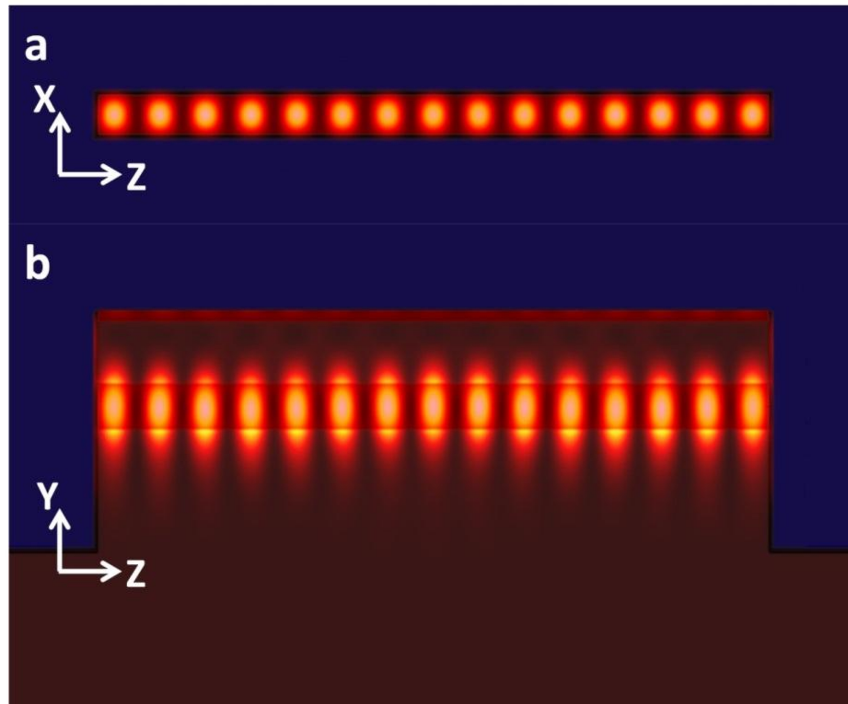

Figure 4.5 Standing wave in a metallic nanocavity based on MISIM waveguide. $|E|^2$ is plotted.

4.4 Device measurement setup

I fabricate a series of such metallic cavity nanolasers based on MISIM waveguides. After fabrication and packaging, devices were loaded into a liquid nitrogen cooled cryostat, whose temperature was controlled by an electric heater from 78K to 293K. The device was forward biased by a DC voltage source (Keithley 6487). The laser emission escaping

from the backside of substrate was collected by an objective and directed to an optical spectrometer equipped with a liquid nitrogen cooled InGaAs detector array. For emission intensity measurement, coarse grating with 1 nm resolution was used. For measurement related to linewidth, peak position, a fine grating was chosen to grantee a 0.2 nm resolution. A Glan-Taylor polarizing prism was used for polarization measurement. The schematic of this measurement setup is shown in Fig. 4.6.

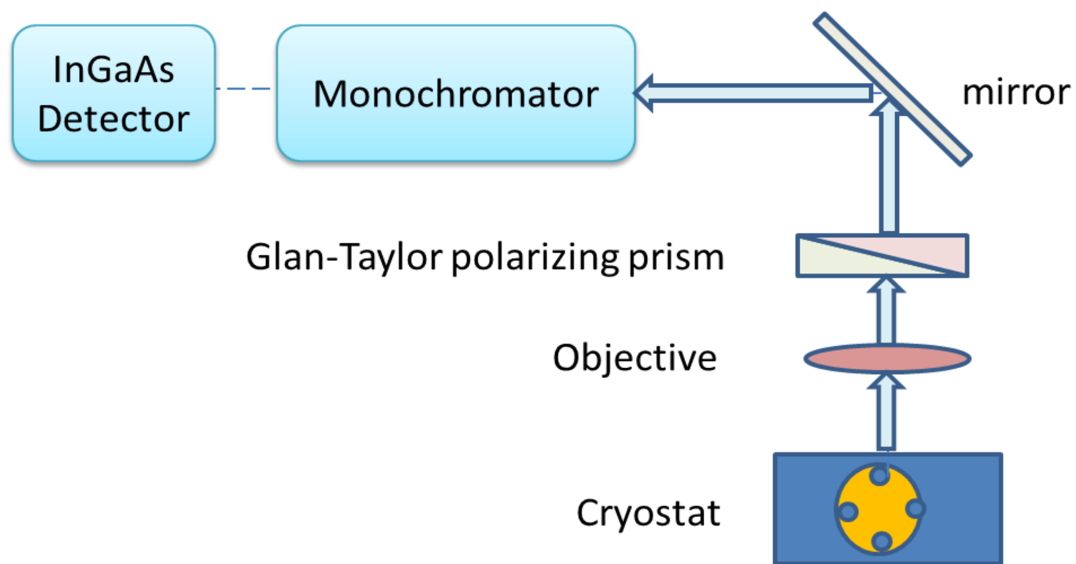

Figure 4.6 Schematic of the optical measurement setup for nanolaser measurement

4.5 Characterization for devices based on MISIM waveguides

In this section I will present characterization result for nanolasers based on MISIM waveguide. Devices discussed here are from my first successful fabrication run. The fabrication for these devices was not optimized, for example I used metal lift-off to transfer EBL pattern to substrate (see detailed discuss in Chapter 2). Therefore the operation temperature is generally under 200 K and most results here were collected at low temperature.

4.5.1 Mode and polarization

As stated in section 4.2, both TE-like and TM-like modes are supported in a MISIM waveguide when the waveguide width is larger the half of the wavelength in gain medium. Due to its less loss and larger confinement factor, the TE-like mode has a lower threshold and will become the lasing mode. Experimentally, TE-like and TM-like mode can be identified through polarization measurement. In the nanolasers, the size of the silver pad is 40 μm × 40 μm, much larger than the lasing wavelength and laser cavity cross section. Therefore lasing emission escaping from the device can be treated as light coming out from an aperture on an infinite perfect metal plate and its far field can be calculated using equivalent surface theorem[43]. In my measurement, light was collected from backside of the substrate in the direction normal to the substrate. Far field calculation shows that in this normal direction, the far field of TE-like mode is linearly polarized along the cavity length direction (Z) and TM-like mode shows linear polarization perpendicular to the length direction.

Such different behaviors of TE-like and TM-like mode is observed in the device with physical dimension of 280 nm (W) × 6 μm (L) × 1.53 μm (H) under DC current injection at 100 K. At a small current of 90 μA, several peaks emerge as shown in Fig. 4.7a. Through polarization resolved measurement, two modes are identified as TE-like mode (TE1 and TE2) and two are TM-like mode (TM1 and TM2) (see Fig. 4.7).

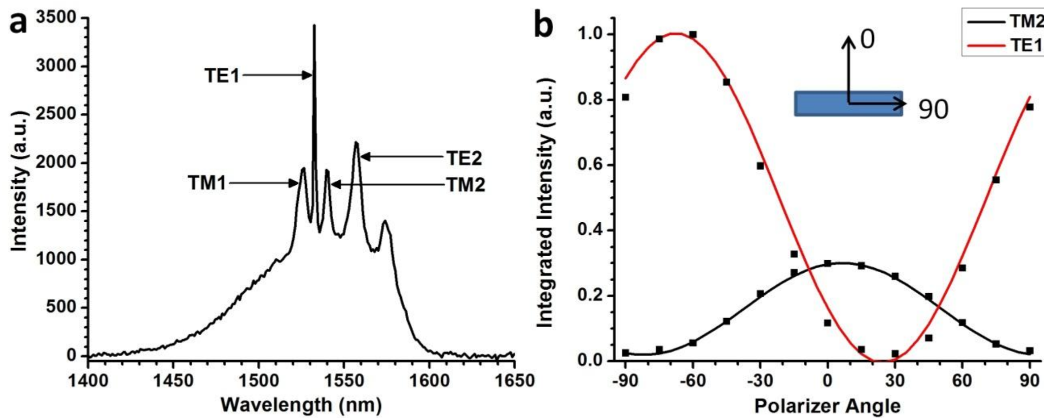

Figure 4.7 **(a)** Multimode observed in a device with physical volume of 280 nm (W) $\times$6 μm (L) $\times$1.53 μm (H) at 100 K before threshold. **(b)** Polarization result for TE1 mode and TM2 mode. TE1 mode is linearly polarized about 20° away for device's length direction (90°) and TM2 mode is linearly polarized perpendicular to device length direction (0°).

As injection current increases, the TE1 mode becomes the final lasing mode after a threshold about 90 μA and the other TM-like modes saturate after threshold as shown in Fig. 4.8. This polarization and L-I measurements combined, confirms the simulation result that in a MISIM waveguide above diffraction limit, both TE-like mode and TM-like mode can be supported and the TE-like mode will become the final dominant lasing mode due to its less loss and larger confinement factor.

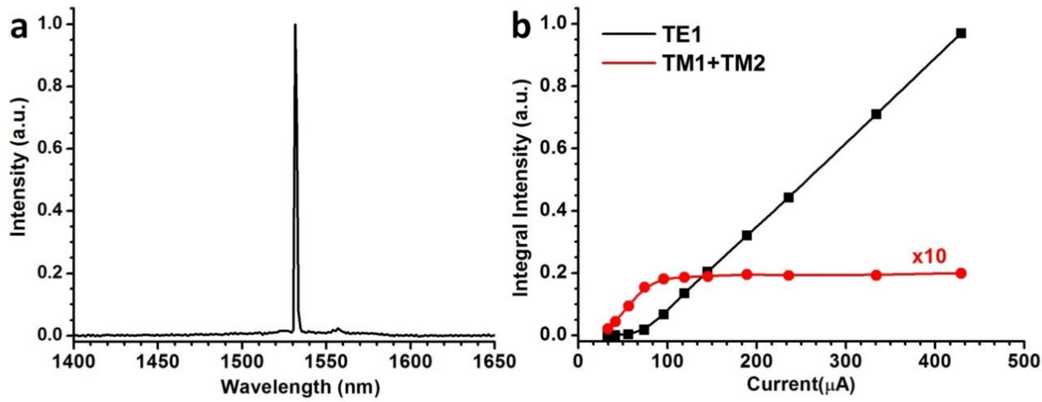

Figure 4.8 **(a)** Lasing spectrum of this device at 429 μA. **(b)** L-I curve for the lasing TE1 mode and sum of TM1 andTM2. The TE1 mode had a threshold around 90 μA while TM1+TM2 saturated after threshold.

4.5.2 Multimode lasing

Multi-longitudinal mode lasing is also observed on some long devices. Figure 4.9 shows the lasing spectra from a device with dimensions of 280 nm (W) ×6 μm (L) ×1.53 μm (H) at 220 K under CW operation.

At a lower current 1186 μA, those multi-modes can be seen more clearly (Fig. 4.10), and modes M1-M3, M5 are equally spaced longitudinal mode. Mode M2 becomes the final lasing mode after the threshold current at 1650 μA. Mode M3 also shows lower a lasing threshold around 1200 μA but its intensity saturates afterwards, giving ways to mode M2.

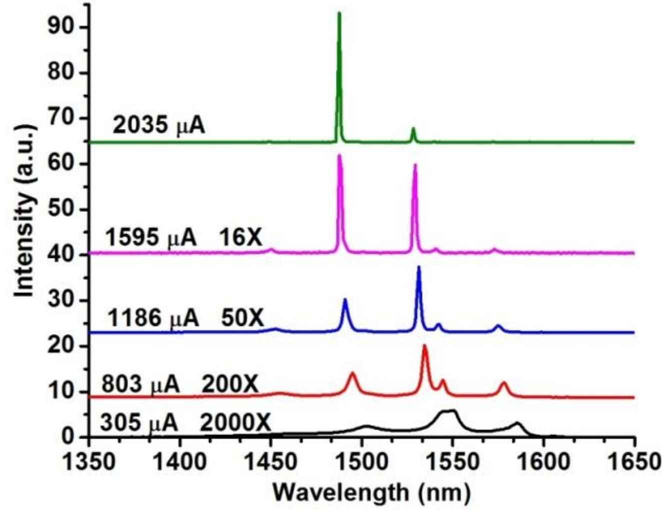

Figure 4.9 Spectra of a device with physical volume of 280 nm (W) × 6 μm (L) × 1.53 μm (H) at 220 K under different injection currents. Double mode lasing is observed.

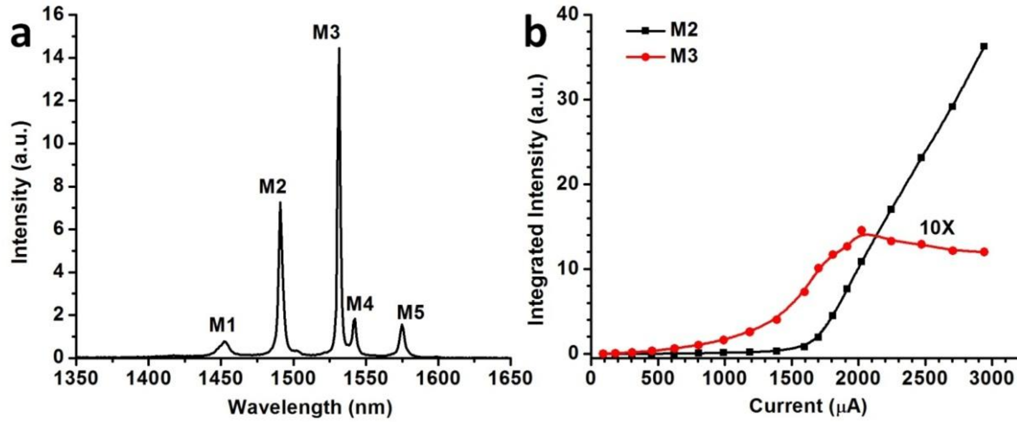

Figure 4.10 **(a)** Spectra for this device at a low current 1186 μA below the threshold of final dominant lasing mode M2. M1-M3, M5 are equally spaced longitudinal mode. **(b)** L-I curve for mode M2 and M3. M2 becomes the final lasing mode after the threshold current at 1650 μA. Mode M3 also shows lower a lasing threshold around 1200 μA but saturates afterwards, giving ways to mode M2.

The group index calculated for these longitudinal modes using standard formula by standard formula (4.2) is plotted in Fig. 4.11.

$$n_g = \frac{\lambda_1 \lambda_2}{2L(\lambda_1 - \lambda_2)} \tag{4.2}$$

A relatively high group index ~4.65 is found here. The InGaAs material has a high material dispersion $\partial\varepsilon/\partial\omega \sim 4\times10^{-15}$ (Ref.45), then the dielectric constant of InGaAs can be expressed as

$$\varepsilon = 12.6 - 7.54\times10^{3}(\lambda - 1550)/\lambda^{2} \tag{4.3}$$

near 1550 nm with λ in the unit of nanometer.

The dispersion of the TE-like mode in a MISIM waveguide with a 280 nm core width and 15 nm SiN layer is obtained through 2D COMSOL simulation and plotted in Fig. 4.12. The group index is calculated as $n_g = c\frac{dk_z}{d\omega} = 4.62$, which matches quite well with the measurement result.

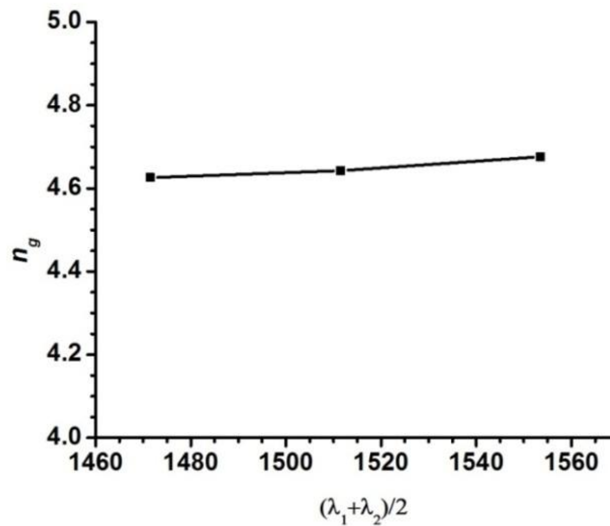

Figure 4.11 Group index calculated for M1-M3 and M5 using (4.2)

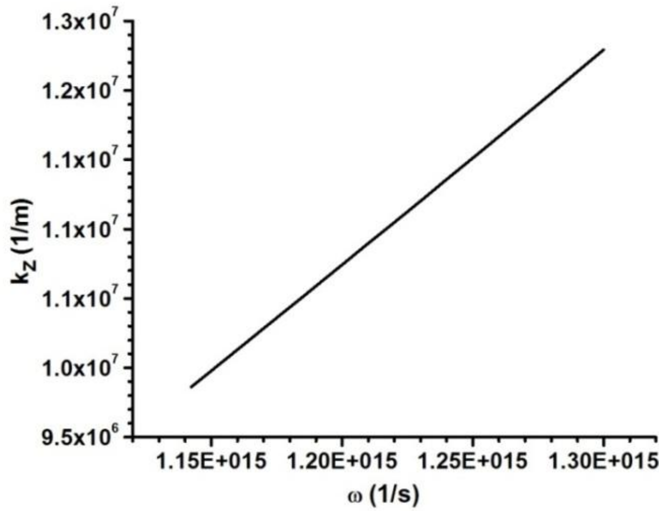

Figure 4.12 Dispersion of the TE-like mode in a MISIM waveguide with a 280 nm core width and 15 nm SiN layer with an InGaAs dispersion shown in (4.3).

4.5.3 Small lasers

Due to low propagation loss and high reflection at the pillar ends, the device length of wide TE-like mode can be significantly shortened while maintaining a reasonable cavity Q factor. CW lasing at 100 K on a device with a physical dimension of 400 nm (W) $\times$900 nm (L) $\times$1.5 μm (H) was observed. The total volume of the device cavity is only 0.19 λ^3 (λ = 1454 nm), even smaller than the device with 90 nm wide plasmonic gap mode reported in Ref. 12. Figure 4.13a shows its lasing spectra under different currents. The L-I curve (Fig. 4.13b) shows a clear threshold at 80 μA. After the threshold, the spontaneous emission saturates, indicating the pinning of carrier density in the active region. The Full Width at Half Maximum (FWHM) of the lasing mode also shrinks from 5.8 nm below threshold (which indicates a Q factor at 250) to 0.6 nm at 635 μA. The behaviors of lasing mode intensity, spontaneous emission intensity and linewidth are

typical of laser threshold[66]. The lasing peak also shows a blue shift with current, from 1468nm at 59 μA to 1454 nm at 890 μA due to band filling. As current increases, the carrier density in the active region increases as well before threshold, which leads to a decrease of refractive index of the InGaAs[67]. So the mode in the laser cavity will shift to shorter wavelength when the current increases as well. Figure 4.14 shows a rapid blue shift of lasing wavelength below threshold and a slowing down of the shift after the threshold where the carrier density in the active region saturates. This is consistent with the behavior of carrier density inside the InGaAs active region as current increases.

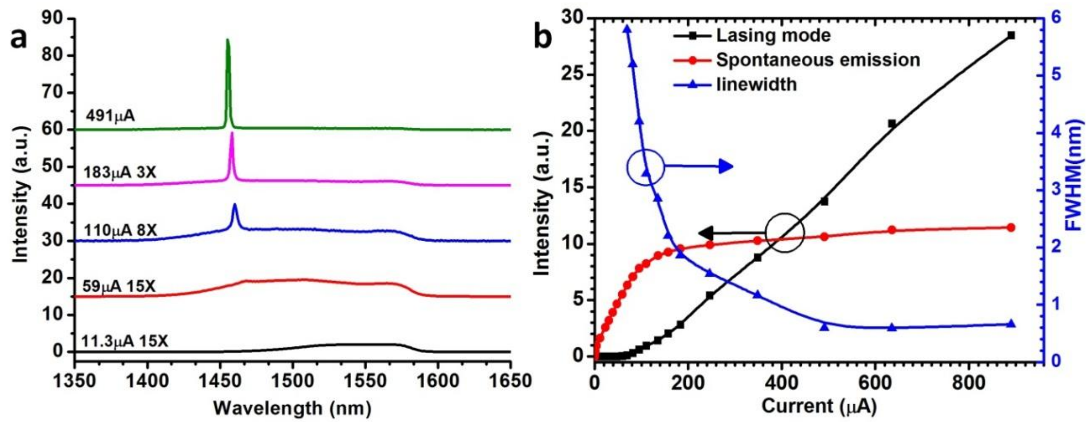

Figure 4.13 **(a)** Lasing spectra of a device with physical volume of 400 nm (W) $\times$900 nm (L) $\times$1.5 μm (H) at 100 K under different injection currents. **(b)** L-I curve shows a lasing threshold around 80 μA. The spontaneous saturates after threshold. Linewidth narrows from 5.8 nm when below threshold to 0.6 nm when above threshold.

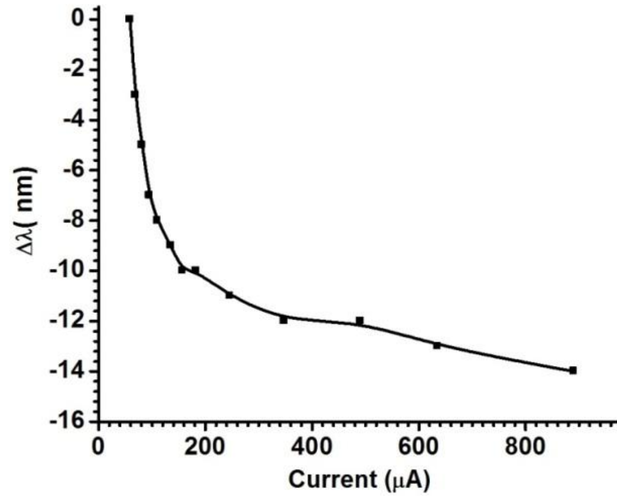

Figure 4.14 Blue shift of lasing mode as current increases

Due to the smaller physical volume, an important property of such deep sub-wavelength cavity lasers is the enhanced spontaneous emission coupled to the lasing mode, also known as the Purcell effect[29] as discussed in Chapter 1. The effective mode volume of the TE_0 mode in this device is estimated to be $5.4(\lambda/2n_{eff})^3$ so a large Purcell factor F=29.27 is obtained using (1.2).

Following rate equations[68,69] including the Purcell effect are used to the lasing behavior.

$$\begin{aligned} \frac{dN}{dt} &= \frac{I}{qV_a} - v_g g S - \frac{1-\beta_0}{\tau_{sp}} N - \frac{F\beta_0}{\tau_{sp}} N - \frac{v_s S_a}{V_a} N - \frac{N}{\tau_a} \\ \frac{dS}{dt} &= \Gamma v_g g S + \frac{\Gamma F \beta_0}{\tau_{sp}} N - \frac{S}{\tau_{ph}} \end{aligned} \tag{4.4}$$

The definitions of the parameters are listed in Table 4.1.

Through rate equation calculation, β_0 is fitted to be 0.004. Spontaneous emission factor defined as ratio of spontaneous emission coupled to the lasing mode to the total emission, or

$$\beta = \frac{F\beta_0}{1-\beta_0+F\beta_0} \quad (4.5)$$

is calculated to be 0.105. This large spontaneous emission factor is two to three orders larger than that in conventional ridge waveguide lasers[70, 71], one order larger than in typical VCSELs[72] and similar to the reported values for microdisk lasers and photonic crystal lasers[73, 74].

Table 4.1 Definitions of parameters in rate equations

Parameter	Definition
N	Carrier density
S	Photon density
v_g	Group velocity
τ_{sp}	Spontaneous emission life time into large 3D space
V_a	Active region volume
v_s	Surface recombination velocity
S_a	Active region surface area exposed to SiN layer
τ_{au}	Auger recombination life time
Γ	Confinement factor
g	Material gain
τ_{ph}	Photon life time
β_0	Spontaneous emission factor without the Purcell enhancement
F	Purcell factor

In (4.4), group velocity v_g appears in the stimulated emission term. In this rectangular nanolaser with a length/width ratio larger than 2, the lasing mode has a definite propagation direction, therefore v_g can be easily obtained through simulation. However, as I will show in Chapter 5, the trapped modes in cylindrical nanolasers do not have a

dominant propagation direction and v_g is not very clear. Therefore (4.4) is not suitable to model those lasers with trapped modes. In Chapter 6, I will develop a rate equation model in which the stimulated emission and spontaneous emission are calculated rigorously from Fermi's golden rule and this rate equation model is applicable to nanolasers presented in this thesis.

The lasing wavelength of this device is 1454 nm, far from the band-edge emission wavelength of InGaAs material at 100 K. Given that the cavity length of this device is only 900 nm, the mode spacing is estimated to be 287 nm around 1.55 μm wavelength using (4.2). So there is only one mode within InGaAs material gain bandwidth. Due to the mismatch between the bandgap and the modal wavelength, such lasers can only lase at a much higher injection level where the gain spectrum expands to overlap with optical mode. Therefore, an important strategy to reduce threshold current for such small lasers is to match the cavity resonance and material gain peak, which can be achieved by careful design of the cavity to tune its resonance or optimize gain material composition.

4.6 Room temperature operation

4.6.1 Strategy to improve operation temperature

Generally, large devices will have lower threshold current density and can operate at higher temperature. For example, in section 4.5.2 I showed a multi-mode laser operating at 220 K with a total physical volume of 0.87 λ^3 (λ = 1487 nm). This volume is already approaching the sub-wavelength volume criteria, but still far away from the room

temperature operation. To improve device operation temperature, its design needs to be optimized both optically and electrically. One major loss mechanism in metallic cavity lasers comes from the overlap of the optical field with the lossy metal, which is directly related to the surface area of the cavity. Figure 4.15 shows the cavity quality factors from FDTD simulation for 2D rectangular silver-SiN-InGaAs cavities with different length/width ratio but same area of 1.9 μm^2 which is about 0.8 λ^2 (λ=1.55 μm) while keeping the mode resonance at 1.55 μm. Clearly with aspect ratio of 3~5, the cavity has the highest Q. In this simulation, the TE mode with electric field in Z direction is simulated. In TE mode, the electric field is parallel to metal surface and has least interaction with the lossy metal thus leading to less metal loss and higher Q. Meanwhile, given the large surface/volume ratio of these sub-wavelength cavity devices, the carrier lifetime in the active region will be significantly reduced by the surface recombination. These two issues are both related to the surface/volume ratio of the metallic cavity. One obvious strategy to improve the cavity quality of the rectangular device optically and electrically is to reduce the aspect ratio, so the structures are more square-like with less surface area at the same total volume.

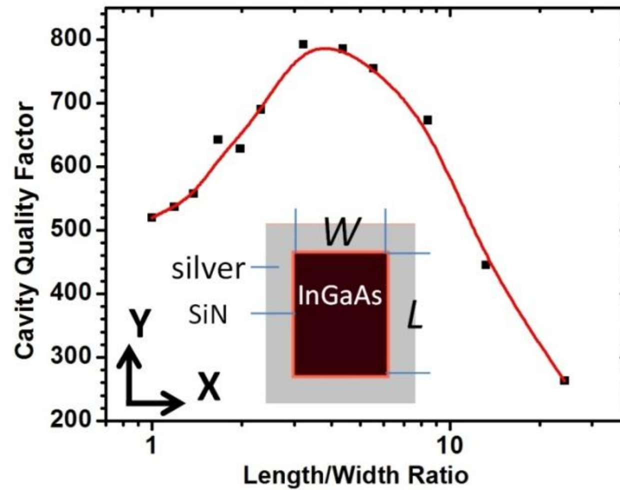

Figure 4.15 Cavity quality factors of 2D rectangular Silver-SiN-InGaAs cavities of different length/width ratios but same total area of 0.8 λ^2. Inset is the simulation geometry.

4.6.2 Endeavors to RT CW Operation

Although this 2D simulation does not necessarily represent exactly the real 3D situation, it does show the improvement of cavity quality factor in a rectangular cavity with proper aspect ratio compared to the narrow waveguide with a large aspect ratio. I fabricated a series of devices with rectangular cross section having different aspect ratios (with device pattern defined by PMMA/ metal lift-off EBL process). Improved CW operation temperature is observed as expected with decreasing length/width ratio. In Figure 4.16, I show the spectra of two lasers with similar volume but different length/width ratio under similar current injection level at room temperature. Physical volume of device 1 and device 2 is 280 nm (W) $\times$ 6 μm (L) $\times$ 1.53 μm (H) and 1.1 μm (W) $\times$ 2.1 μm (L) $\times$ 1.5 μm (H) respectively. The length/width ratios for these two devices are 21.4 and 1.91, respectively. Though they have similar physical volume 0.87 λ^3 and 0.95 λ^3 (λ is the

mode wavelength of each device), device 1 (Fig. 4.16a) shows a broad linewidth of 4.5 nm while device 2 (Fig. 4.16b) with smaller length/width ratio shows a narrower linewidth of 3 nm, which is a significant improvement.

The lasing quality of the result shown in Fig. 4.16b is not very good[75]. On one hand, the intensity of lasing mode (Fig. 4.17, black arrow) increases much faster than the non-lasing mode (Fig. 4.17, red arrow) and spontaneous emission (Fig. 4.17, pink arrow) as current increases, and the linewidth shows a dramatic drop from 11.5 nm to 3 nm. Such superlinear increase in lasing mode intensity and significant narrowing in linewidth are important signatures of lasing. But on the other hand, the broad linewidth and smooth threshold transition indicate that laser is, at least, not operating far above threshold. Such broad linewidth is often seen in reported in demonstrations of nanolaser under room temperature CW operation[15, 21]. The broad linewidth and smooth threshold transition in all these demonstrations can be attributed to the severe self-heating at room temperature under DC electrical injection and it does raise questions about the capability of such sub-wavelength metallic cavity lasers operating at room temperature with CW performance comparable to conventional semiconductor lasers. Meanwhile most of the proposed applications of nanolasers such as on chip sensing and communication require narrow linewidth[47,76]. A demonstrate of RT CW nanolaser with lasing characteristics similar to conventional semiconductor lasers, such as narrow linewidth and clear threshold, is needed to clear all the doubts on metallic cavity nanolasers.

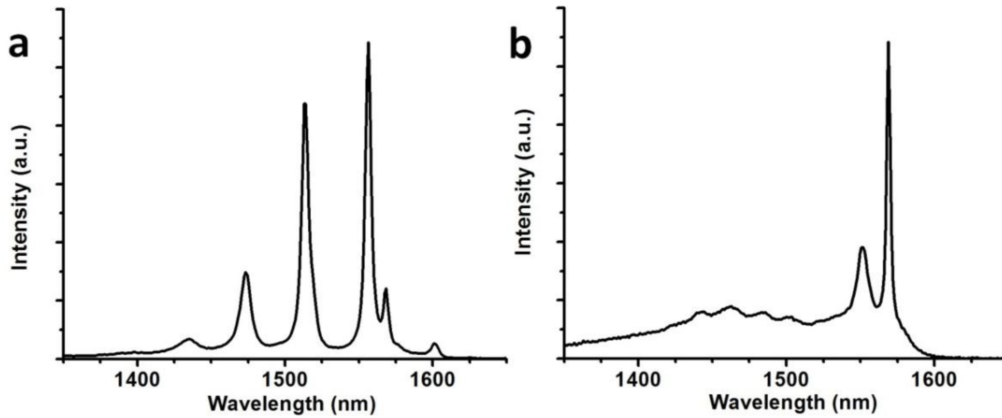

Figure 4.16 Spectra of two devices under similar current injection at room temperature. **(a)** 280 nm (W) × 6 μm (L) × 1.53 μm (H), current is 2964 μA. **(b)** 1.1 μm (W) × 2.1 μm (L) × 1.5 μm (H), current is 2276 μA.

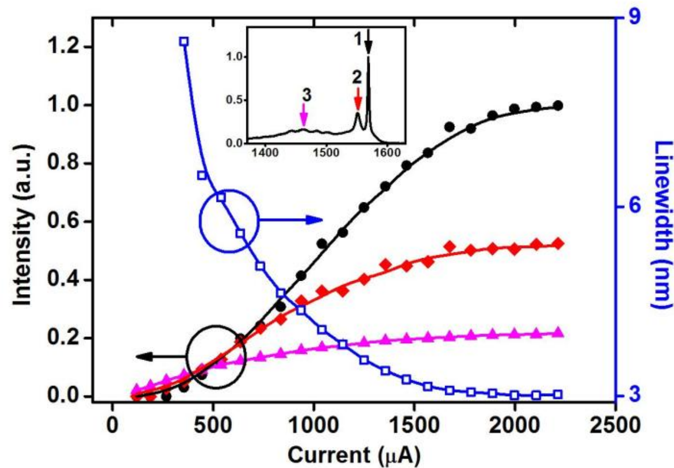

Figure 4.17 Light intensity and FWHM as functions of DC current at 293K. Inset: spectrum with arrows and numbers indicating positions where light intensity is taken: lasing mode (● circles, 1), non-lasing mode (♦ diamonds, 2), and spontaneous emission at 1460 nm (▲ triangles, 3). The threshold is estimated ~1000 μA.

4.6.3 Record performance of RT CW nanolaser

To improve device performance, I further optimized fabrication process for our nanolasers in our second generation of device including HSQ electron beam lithography, more thorough surface cleaning and improved silver deposition with large silver crystal

grain size (see details in section 3.5), and finally achieved break through by demonstrating a RT CW nanolaser with narrow linewidth and clear threshold on a device with optical cavity dimensions (including the SiN layer) of 1.15 (W) $\times$ 1.39 (L) $\times$ 1.7 (H) $\mu m^3 = 0.67\ \lambda^3$ (λ=1591 nm).

The light output versus current (L-I curve) for this device is shown in Fig. 4.18(a). The L-I curve shows a clear turn-on threshold around 1.1 mA. Above the threshold, the integrated lasing mode intensity increases linearly with injection current. The integrated spontaneous emission intensity initially increases faster than the lasing mode intensity but shows a gradual clamping trend afterwards, giving way to the lasing mode. Well below threshold and close to transparency, FWHM of the lasing peak is 6.8 nm, corresponding to a cavity quality factor of 235. The FWHM shows a rapid decrease with increasing current and further drops to 0.5 nm at 2.02 mA. Such intensity and linewidth behavior is typical of a laser transition from below to above threshold as pumping current increases. As shown in Fig. 4.18b, the threshold behavior is accompanied by a significant blue shift of the laser wavelength from 1601 nm (well below threshold) to 1591 nm (above threshold) due to the band filling effect.

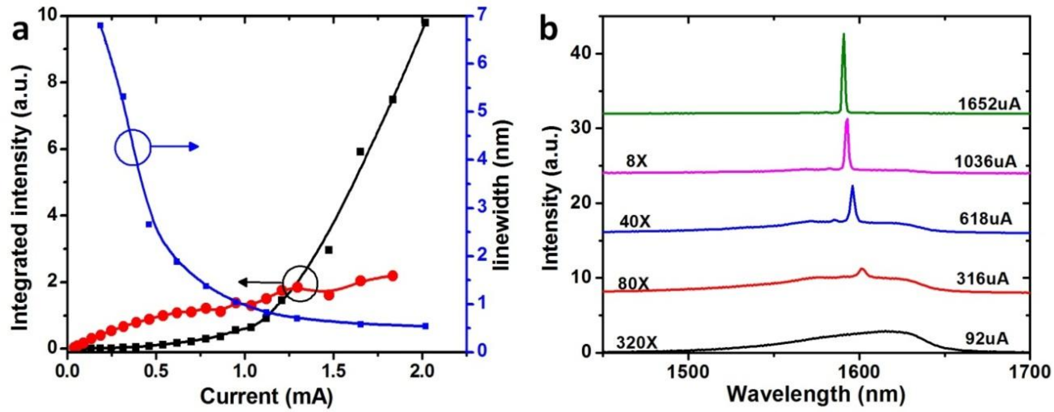

Figure 4.18 CW Laser characteristics at room temperature of a device with physical volume of 1.15 μm (W) × 1.39 μm (L) × 1.7 μm (H). **(a)** L-I and FWHM-I curve at 294K under DC current injection of the laser. ■: integrated lasing mode intensity; ●: integrated spontaneous emission intensity. **(b)** Spectra (offset for clarity) of this device at different currents.

Optical mode properties in this device are investigated through three-dimensional finite-difference time-domain (FDTD) simulations. A mode (E_{106}, corresponding to 1, 0 and 6 E-field nodes in x, y, and z direction of the cavity, see Fig. 4.19a) with Q-factor of 428 is identified as the lasing mode. Using the surface equivalence theorem[43], the far field radiation in the direction normal to the substrate for this mode is calculated and shows linear polarization along the Z direction, which matches the polarization measurement results (see Fig. 4.19b). The effective mode volume is estimated to be $V_{eff}=10.29(\lambda/2n_{eff})^3$, and the confinement factor is 0.645. The Q-factor from experiment is significantly lower than in the simulation, and the difference is likely due to the imperfections of the fabrication, such as deviation of the electron beam lithography pattern from a perfect rectangle and non-vertical cavity sidewalls.

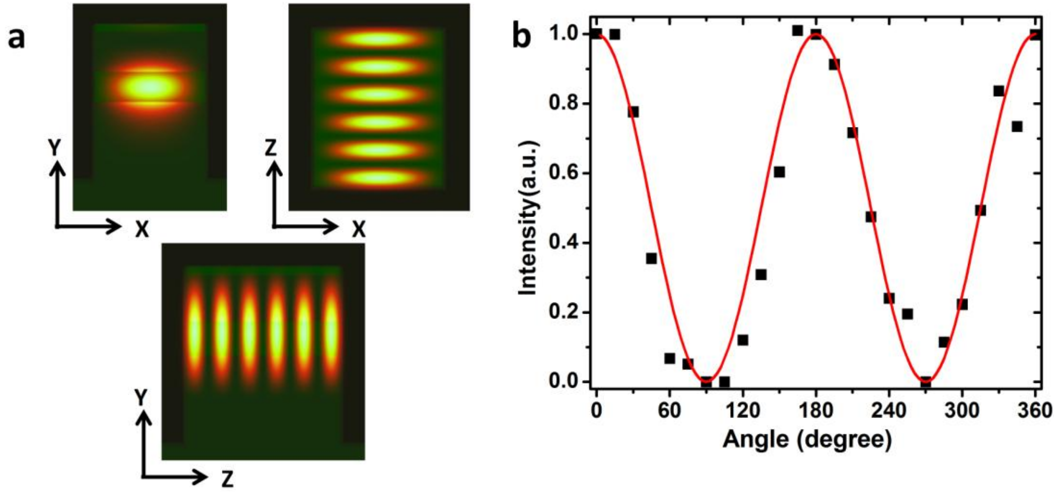

Figure 4.19 **(a)** $|E|^2$ patterns of E_{106} mode. **(b)** Polarization resolved measurement result, where Z-direction corresponds to 0 and 180 degrees.

To understand the lasing behavior, rate equations (4.4) are used to model a single mode nanolaser at room temperature. Purcell factor F calculated to be 13.88. Surface recombination is also considered as an essential parameter given the large surface area to volume ratio of such a sub-wavelength cavity device. Solving for the steady-state photon density and current of the rate equations, I find a good agreement between the measured and calculated L-I curves. The Purcell effect enhanced spontaneous emission factor β is estimated to be 0.048.

Plotting the L-I curve on a log-log scale, Figure 4.20 clearly shows three regions with different slopes, representing the evolution of device output from spontaneous emission to threshold transition and eventually above-threshold lasing. Below the threshold transition region, a slope of 2 is observed in the log-log scale L-I curve. Well below threshold, the lasing mode emission is dominated by spontaneous emission and a linear

scaling is expected if current is also dominated by spontaneous emission. The superlinear scaling below threshold indicates that the current contains significant contributions from non-radiative recombinations such as surface recombination and Shockley-Read-Hall (SRH) process. In such a sub-wavelength device, the surface recombination lifetime is estimated to be on the order of nanoseconds. Typical bulk SRH recombination lifetime in metal organic chemical vapor deposition (MOCVD) grown high quality intrinsic III-V semiconductors is hundreds of nanoseconds[53], so SRH process is negligible compared to surface recombination and therefore ignored in the rate equation analysis. A surface recombination velocity of 5×10^4 cm/s is obtained through rate equation fitting. This value is lower than typical surface recombination velocity of InGaAs structures produced by dry etching processes which is $1\sim2\times10^5$ cm/s [53,54], and approaches the lowest value reported to our knowledge[55]. I believe that low surface recombination is one of the key factors to achieve good device performance[77], and improvement in surface passivation techniques to further reduce surface recombination velocity will lead to further improvement in the performance of such sub-wavelength cavity lasers.

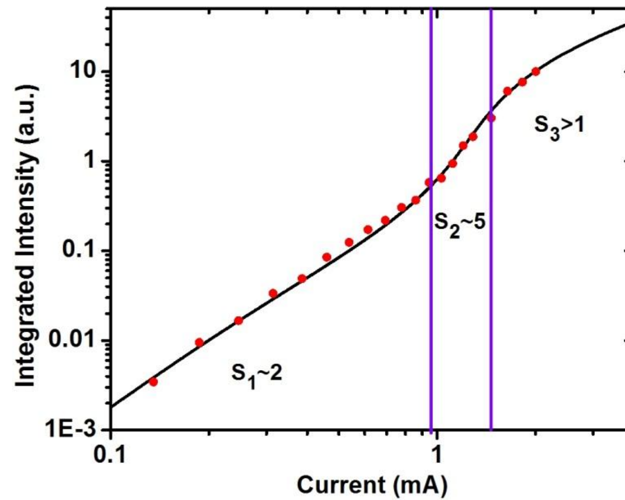

Figure 4.20 L-I curve plotted on a log-log scale and its slope from experimental result (red solid circle ●) and from rate equation (RE) calculation (solid line), with slopes given for three regions.

4.7 Summary

In this chapter, I discussed my research work on rectangular metallic cavity nanolasers. I started with nanolasers based on MISIM waveguide, in which both TE-like and TM-like plasmonic gap mode can be supported depending on waveguide width. Though light can be squeezed below diffraction limit in a TM-like mode, I chose to focus on devices supporting TE-like mode in a waveguide wider than half the wavelength in the gain media due to its relatively low loss and large confinement factor which in turn leads to lower lasing threshold. Lasing phenomena such as TE, TM mode competition and multimode lasing were observed and studied. CW lasing from a deep sub-wavelength device with a physical cavity volume as small as $0.191\lambda^3$ was demonstrated. To reduce surface related loss in such metallic cavities, I also investigated devices with smaller

length/width ratio to reduce surface/volume ratio in which the concept of waveguide no longer applies. Through optimizing design and fabrication, I finally demonstrated a RT CW metallic cavity nanolaser with a physical cavity volume $0.66\lambda^3$ under electrical injection. This result is critical in many respects. This unambiguous demonstration proves that such sub-wavelength nanolasers with metallic cavities are capable of RT operation with similar characteristic performance to a conventional semiconductor laser. In terms of technological applications, RT CW electrical injection operation represents a key milestone for the practical implementation of such devices as one key component of future nanophotonic systems.

CHAPTER 5

CIRCULAR NANOLASERS

5.1 Introduction

In this chapter, I will discuss one type of metallic cavity nanolasers with circular cross section. In circular nanolaser, trapped modes or whispering gallery modes are supported. In small circular nanolasers, the mode spacing is so large that single mode lasing and resonance tuning can be easily achieved by controlling the size of device through EBL pattern definition. Cylindrical cavities are known to support modes with cylindrical symmetries, especially modes with radially or azimuthally polarized beams. Such cylindrical-symmetry sources are especially important for high-resolution microscopy, particle trapping applications, and laser machining. Devices supporting TE_{01} mode show interesting azimuthal polarization, which may have special applications. High temperature operation is observed in some larger devices supporting whispering gallery mode.

5.2 Modes in circular metallic nanocavity

The structure of a circular metallic cavity nanolaser is shown in Fig. 5.1. A cylindrical InP/InGaAs/InP pillar is encapsulated in SiN and silver to form a metallic nanocavity. Device structure is identical to rectangular nanolaser except for the shape of its circular cross section.

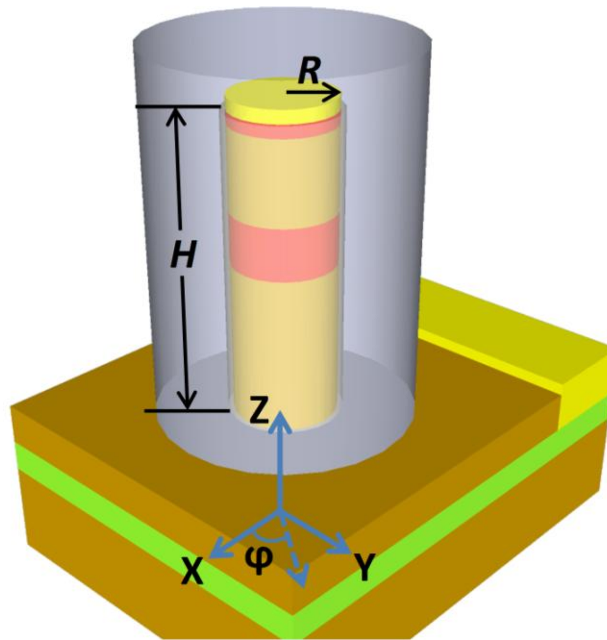

Figure 5.1 Structure of a rectangular metallic cavity nanolaser. Dimensions of the rectangular pillar, radius (R), height (H, in Z direction), are labeled.

The optical field ($|E|^2$) for the three lowest order modes: HE_{11}, TM_{01} and TE_{01}, are shown in Fig. 5.2. Compared to the waveguide modes discussed in Chapter 2 and Chapter 4, and the whispering gallery modes in microdisk cavities, those low order modes do not show a dominant propagation direction. They are trapped in the InGaAs high index region, instead of propagating in certain direction. If modes are propagating in the vertical direction of the pillar, they will suffer from huge radiation loss at the bottom part of the cavity where there is no high reflection DBR structure. Therefore such trapped mode becomes the dominant mode in these small lasers. Within the gain spectrum bandwidth of InGaAs, these modes are only supported in devices with a small radius (100 nm – 250 nm). Mode resonance as a function of pillar radius for a device with 30 nm SiN is plotted in Fig. 5.3. The mode spacing between these three modes is so large that only

one mode will fall within the gain spectrum bandwidth of InGaAs gain material for a given device radius, thus enables single mode operation. Meanwhile, the mode resonance shifts almost linearly with respect to cylinder radius. Therefore the lasing wavelength can be tuned easily by controlling the cylinder radius.

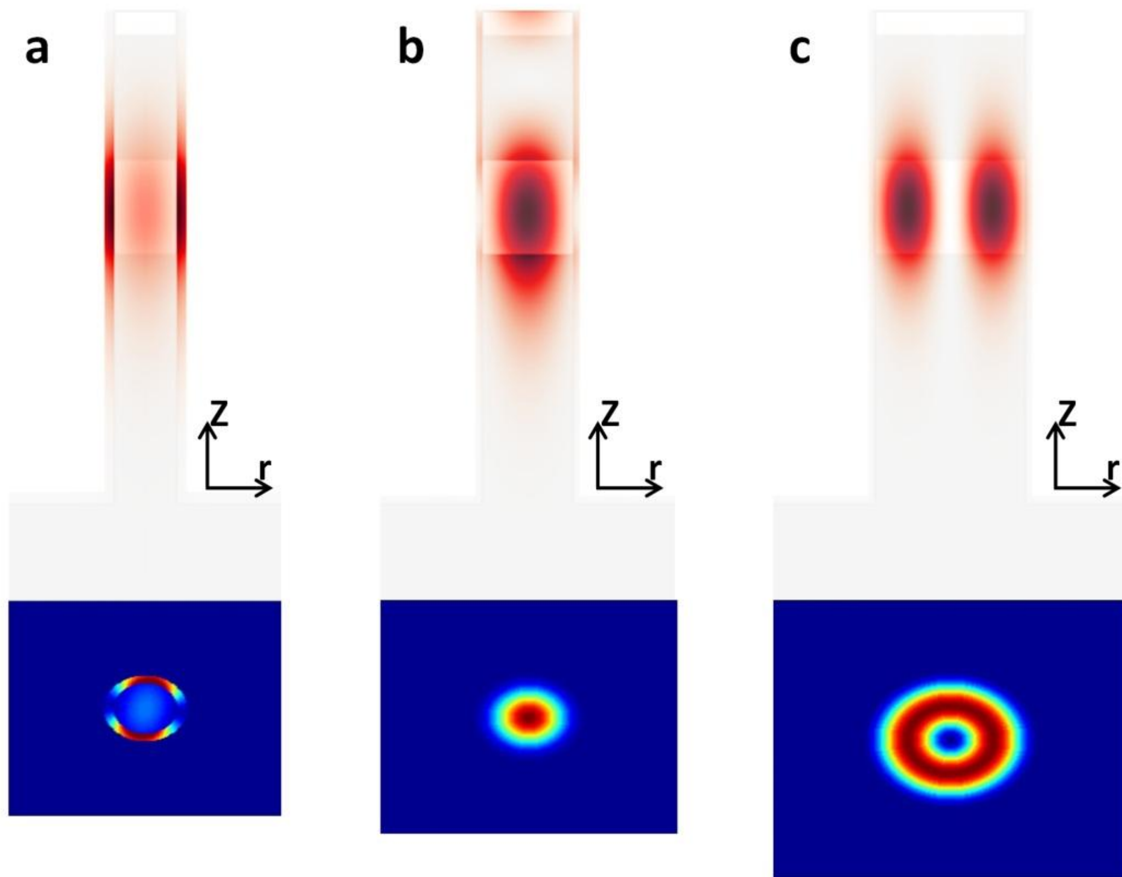

Figure 5.2 Mode optical field $|E|^2$ of **(a)** HE_{11} mode, R = 100 nm **(b)** TM_{01} mode, R = 145 nm and **(c)** TE_{01} mode R = 240 nm. The bottom part of the each figure shows the $|E|^2$ pattern at the cross section plane at the center of InGaAs gain layer.

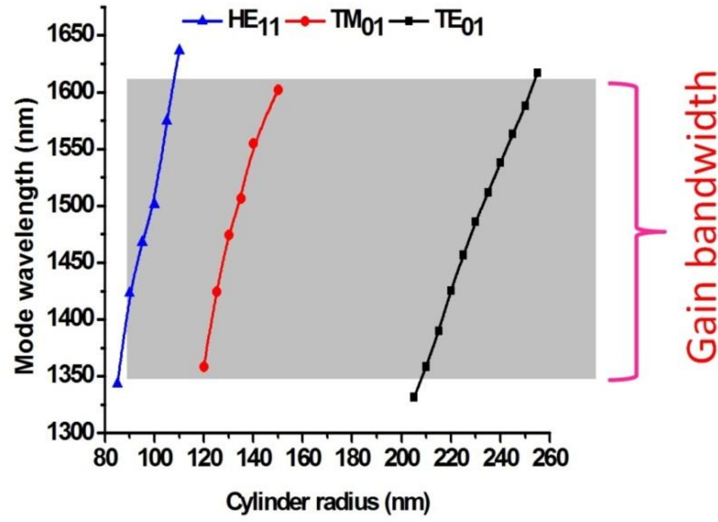

Figure 5.3 Resonance wavelengths of HE_{11}, TM_{01} and TE_{01} modes in a metallic cavity nanolaser as a function of semiconductor pillar radius. Thickness of SiN layer is 30 nm. Shaded gray region indicates roughly the gain bandwidth of InGaAs material.

5.3 First generation with thick SiN layer

5.3.1 Optimizing SiN thickness

From the rate equations (4.4), the laser threshold gain is

$$g_{th} = \frac{2\pi n_g}{\Gamma Q \lambda} \tag{5.1}$$

So g_{th} is inversely proportional to ΓQ product. To reduce laser threshold, large Q factor and Γ are needed. Among the three lowest modes, the TE_{01} mode usually has a large Q factor compared to the other two. The electric field is dominated by the azimuthal component which is always parallel with the metal surface. This particular electric field has least interaction with lossy metal, which leads to least metal loss and a high Q factor.

For the trapped mode with no dominant propagation direction, it is difficult to get the confinement factor using (1.1). So the energy confinement factor Γ_E (2.18) is here for approximation.

This Q factor can be further improved by optimizing the thickness of the SiN layer. Due to its lower refractive index, the SiN serves as an optical buffer layer between active region and lossy metal. A thicker dielectric layer can better isolate the optical field from lossy metal thus reducing metal loss and increasing cavity Q factor. But on the other hand, thick SiO_2 can reduce Γ_E since more energy is stored in the SiO_2 layer. Obviously there is an optimum SiO_2 thickness that generates the largest $\Gamma_E Q$ product for lowest threshold gain.

To obtain this optimum thickness, simulations for the devices supporting TE_{01} mode is performed. In this simulation I change both the thickness of SiN and radius of InP/InGaAs pillar simultaneously to keep the resonance wavelength around 1.55 μm. The simulated Q factor, energy confinement factor Γ_E, and the $\Gamma_E Q$ product are plotted in Fig. 5.4. The largest $\Gamma_E Q$ product is obtained with SiN thickness at 120 nm and semiconductor pillar radius at 190 nm.

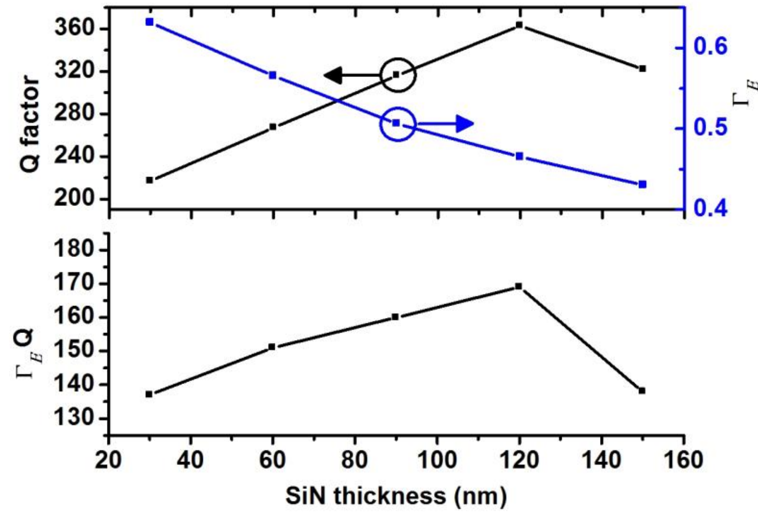

Figure 5.4 Cavity Q factor and energy confinement factor (upper panel) and Γ_EQ product (lower panel) as a function of SiN thickness for the TE_{01} mode. In FDTD simulation, semiconductor radius is modified accordingly to keep the resonance wavelength around 1.55 μm.

This optimum SiN thickness generates a large Γ_EQ product at 169, corresponding to a threshold material gain of 959 cm^{-1} if a group index n_g is estimated at 4. Such threshold material gain is achievable at room temperature[78]. Noticeably, the radius of InP/InGaAs pillar is 190 nm. The pillar height is around 1.5 μm, then the total physical volume of this cavity, including SiN layer, is only 0.125 λ^3.

5.3.2 Azimuthal polarization of TE_{01} mode device

Another interesting property of this TE_{01} mode is its azimuthal polarization. Inside the cavity, the optical field is dominated by the azimuthal electric field and shows a 'donut' shape (see Fig. 5.5a). Simulation also shows that this azimuthal polarization is preserved after the light escaping from the cavity through the bottom aperture as shown in Fig. 5.5b.

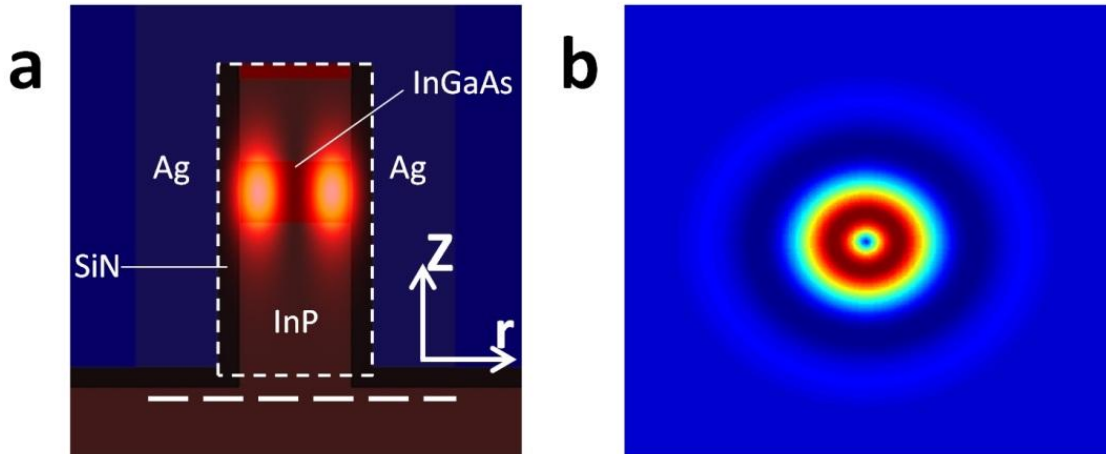

Figure 5.5 **(a)** $|E|^2$ field of TE_{01} mode in Z-r plane. Cavity boundary is marked by white dashed rectangle. **(b)** Azimuthal component of the electric field of TE_{01} mode beneath the cavity bottom aperture at the vertical location in r-φ plane, indicated by the white long dashed line in (a).

As a subset of cylindrical vector beams, azimuthally polarized beam has special applications such as particle trapping[79] and high resolution imaging[80]. Numerous approaches have been developed to generate azimuthally polarized light beams, including inserting optical components into YAG laser cavities[81, 82] to select the lasing mode. Optical fibers[83] and dielectric gratings[84] are utilized to convert light beam to azimuthal polarization as well. However, these methods are generally cumbersome. Incorporating surface grating has been proven as an effective approach to realize polarization control and stabilization in vertical cavity surface emitting lasers (VCSELs)[85]. Compact light sources based on this approach for radially polarized beam have been demonstrated[8]. Metallic cavity nanolasers with circular geometry also exhibit such polarization properties. Radially polarized lasing emission was observed in a metallic coaxial nanolaser[15]. Yu *et al*[18] reported lasing emission with azimuthal polarization from

nanopatch lasers. However, both of them were under optical pumping. The circular metallic cavity nanolaser could serve as a compact electrically driven laser source with azimuthal polarization.

5.3.3 Characterization of circular nanolaser

I fabricated a series of devices with semiconductor pillar radius from 165 nm to 250 nm and SiN layer thickness at 120 nm. Measurements with DC current injection were performed at 78 K. Light output from a device was collected by a 50X objective with a 0.5 numerical aperture. Passing through a beam splitter, half of the light was detected by a spectrometer equipped with a liquid nitrogen cooled InGaAs array detector and the other half was directed to an InGaAs near infrared (NIR) camera for imaging. The optical setup is schematically shown in Fig. 5.6. CW lasing was achieved at 78 K. Figure 5.7 shows lasing characteristics from a device with a semiconductor pillar radius of 175 nm and a total cavity volume of 0.146 λ^3 (λ = 1416 nm), including SiN layer. The L-I curve (Fig. 5.7b) shows a threshold current around 80 μA. The saturation of the spontaneous emission confirms the lasing behavior. Linear resonance wavelength shift is observed over a large wavelength range from 1.37 μm to 1.53 μm on devices with different radius (see Fig. 5.7c). A shifting slope defined as $\Delta\lambda/\Delta d$ (λ: resonance wavelength, d: semiconductor pillar diameter) from experimental result is 2.7, which matches the value of 3.1 for TE_{01} mode from simulation well.

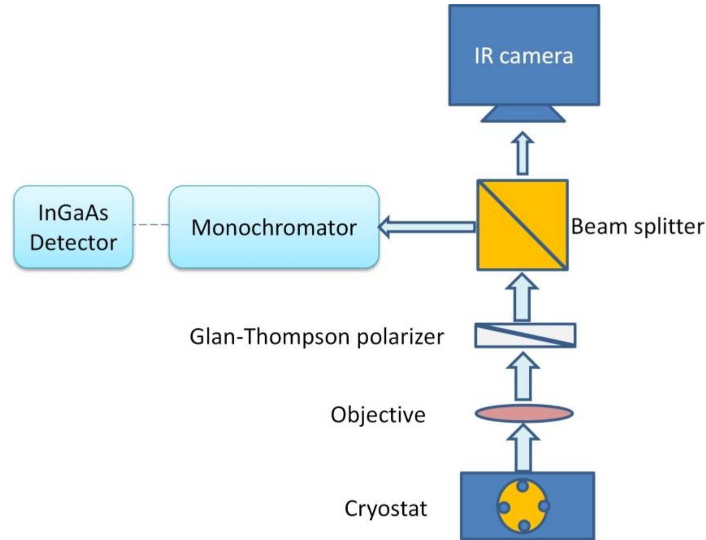

Figure 5.6 Schmetic of the optical setup for nanolaser measurement

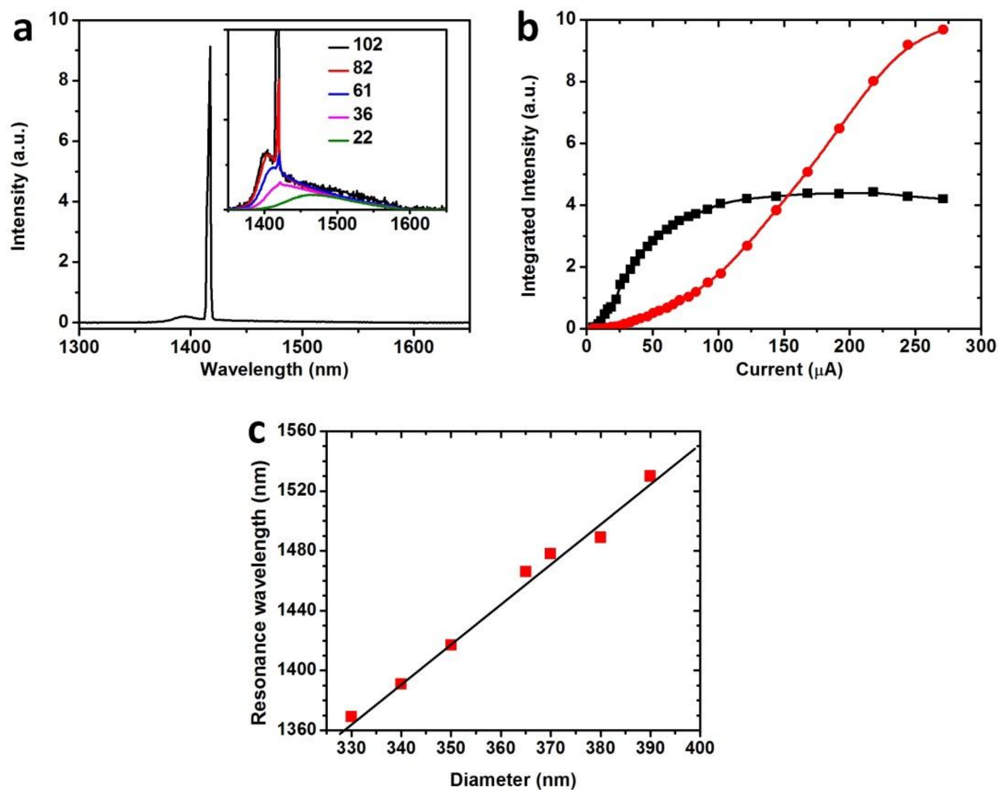

Figure 5.7 Lasing characteristics of a circular nanolaser with pillar radius at 175 nm, total cavity volume of 0.146 λ^3 (λ = 1416 nm), including SiN layer. **(a)** Lasing spectrum. Inset is the lasing spectra under different currents (μA). **(b)** Integrated intensity of lasing mode (red circle) and spontaneous emission (black square) of this device as a function of injection current. **(c)** Linear dependence of resonance wavelength on diameter from 1.37 μm to 1.53 μm. The slope is 2.7.

To confirm the azimuthal polarization of the lasing beam, I took the images of the laser output after inserting a linear polarizer between the objective and camera. The beam splitter was removed to avoid any influence from it. The azimuthal polarization is characterized by the dark line splitting the images along the polarizer direction (see Fig. 5.8a). The origin of this dark line is illustrated in Fig. 5.8b. The electric field in an azimuthally polarized beam is always along the tangential direction of the concentric circles. Therefore electric field along one circle axis (the shaded double arrow) will be blocked by the polarizer, leaving a dark line in the beam image. Hence a compact nanoscale electrically driven laser source for azimuthally polarized beam is realized based on a metallic cavity nanolaser supporting TE_{01} mode.

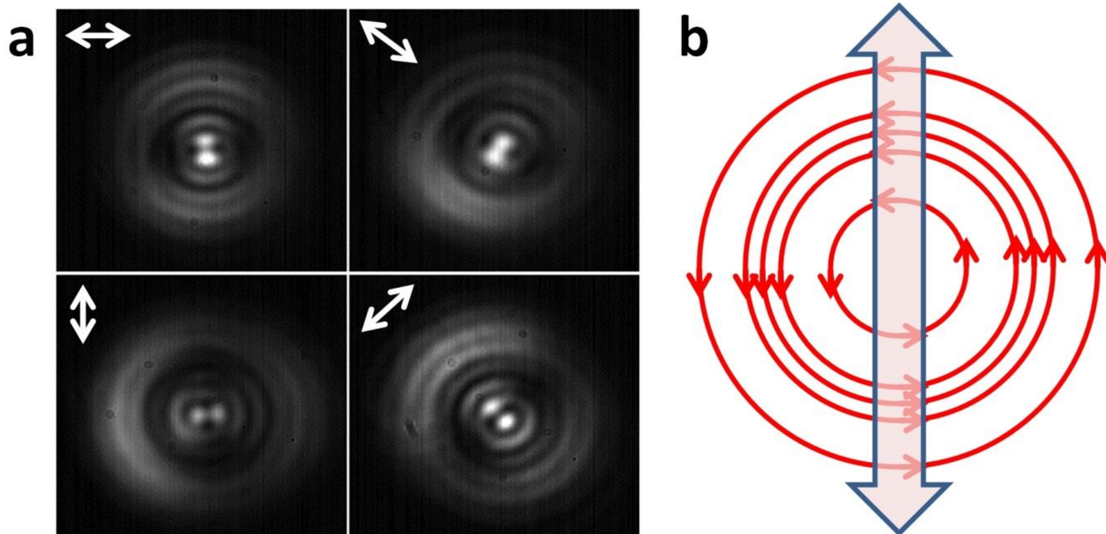

Figure 5.8 **(a)** Laser output images taken by a NIR camera behind a linear polarizer in four different orientations, as indicated by the white arrow. The dark line splitting the image along the polarizer direction confirms the azimuthal polarization of the laser output. **(b)** Schematic illustration of the dark line in (a). Electric field (red lines) at the circle axis (the shaded double arrow) is be blocked by the polarizer, leaving a dark line in the beam image.

Compared to other compact light sources for cylindrical vector beams, such as the surface grating VCSELs reported by Cai *et al*[8], this circular nanolaser is not only smaller but also offers a reduction in fabrication complexity. First, vertical confinement in this nanolaser is achieved through trapping optical mode in high refractive index gain material instead of reflection by DBR, thus eliminating the need for complex DBR layer stack growth. Second, desired single TE_{01} mode lasing can be ensured easily by controlling the radius of semiconductor pillar in lithography step while design and fabrication of surface grating for VCSELs is generally more sophisticated.

CW operation temperature of the laser is limited to 78 K, far below the room temperature as predicted in the simulation. I believe that the reason can be mainly attributed to the device degradation due to poor heat dissipation and surface recombination related to the thick SiN layer (120 nm) used. Slightly larger devices are able to reach CW lasing at higher temperature. Figure 5.9 shows the CW lasing spectrum from a device with a radius of 255 nm supporting TM_{02} mode under DC current injection at 200 K. The total volume of this device is 0.283 λ^3 (λ = 1.342 μm).

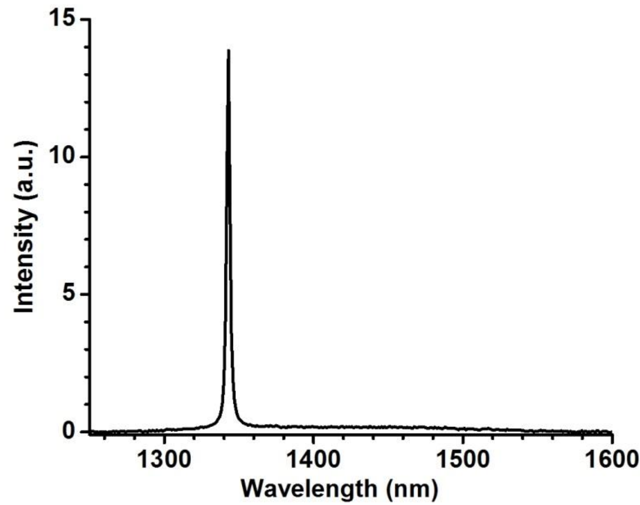

Figure 5.9 CW lasing spectrum from a device with a radius of 255 nm supporting TM_{02} mode under DC current injection at 200 K. The total volume of this device is 0.283 λ^3 (λ = 1.342 μm).

5.4 Second generation with thin SiN

Though CW lasing at deep sub-wavelength circular nanolasers is successfully demonstrate, the operation temperature of those devices is quite low, far below what simulation predicts. Device performance also degrades rapidly, resulting a very short lifetime. The poor heat dissipation and high surface recombination due to thick SiN layer used could be the reason for this limited operation temperature and device lifetime. To obtain devices capable of room temperature operation, I fabricated a second generation of circular nanolasers with larger sizes (radius from 420nm to 730 nm). I also reduced the SiN thickness to 30 nm so as to improve heat dissipation and reduce surface recombination.

Higher order modes or whispering gallery modes with much smaller mode spacing are supported in these large devices. Multimode operations are often observed in these

large devices. For example, Figure 5.10 shows the emission spectrum from a device with radius of 540 nm at 200K under DC current injection. The three major modes in this spectrum, M2 and M3 show very narrow linewidth and the M1 is somehow broader. Through FDTD simulation, these three modes are identified as TM_{51} (whispering gallery mode), HE_{13} and EH_{22} respectively, whose mode patterns ($|E|^2$) are shown in Fig. 5.11.

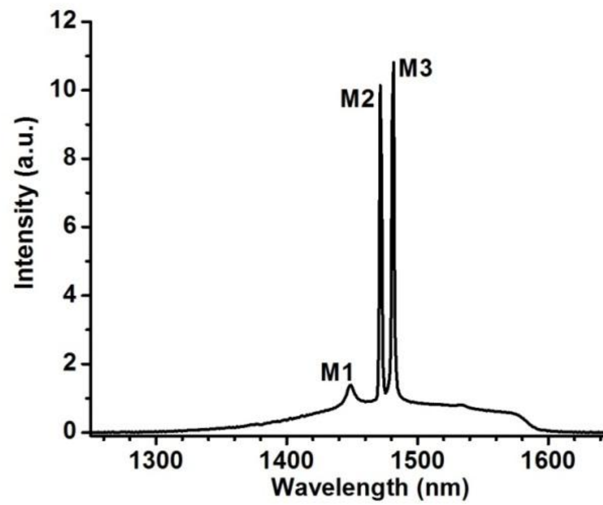

Figure 5.10 Emission spectrum from a device with radius of 540 nm at 200K under DC current injection

The wavelength and Q factor of these three modes are listed in Table 5.1. Material dispersion of InP and InGaAs is not considered, so the wavelength from simulation and experiment differs a bit but relative mode position from simulation and experiment match quite well. Meanwhile, the difference in mode Q factor from simulation is well reflected in experimental results.

Table 5.1 Mode resonance wavelength and Q factor for a circular nanolaser with 540 nm radius from simulation and measurement.

	Simulation	Experiment
EH_{51} wavelength (nm)	1426	1448
EH_{51} Q	379	247
HE_{13} wavelength (nm)	1480	1473
HE_{13} Q	490	736
EH_{22} wavelength (nm)	1485	1482
EH_{22} Q	413	673

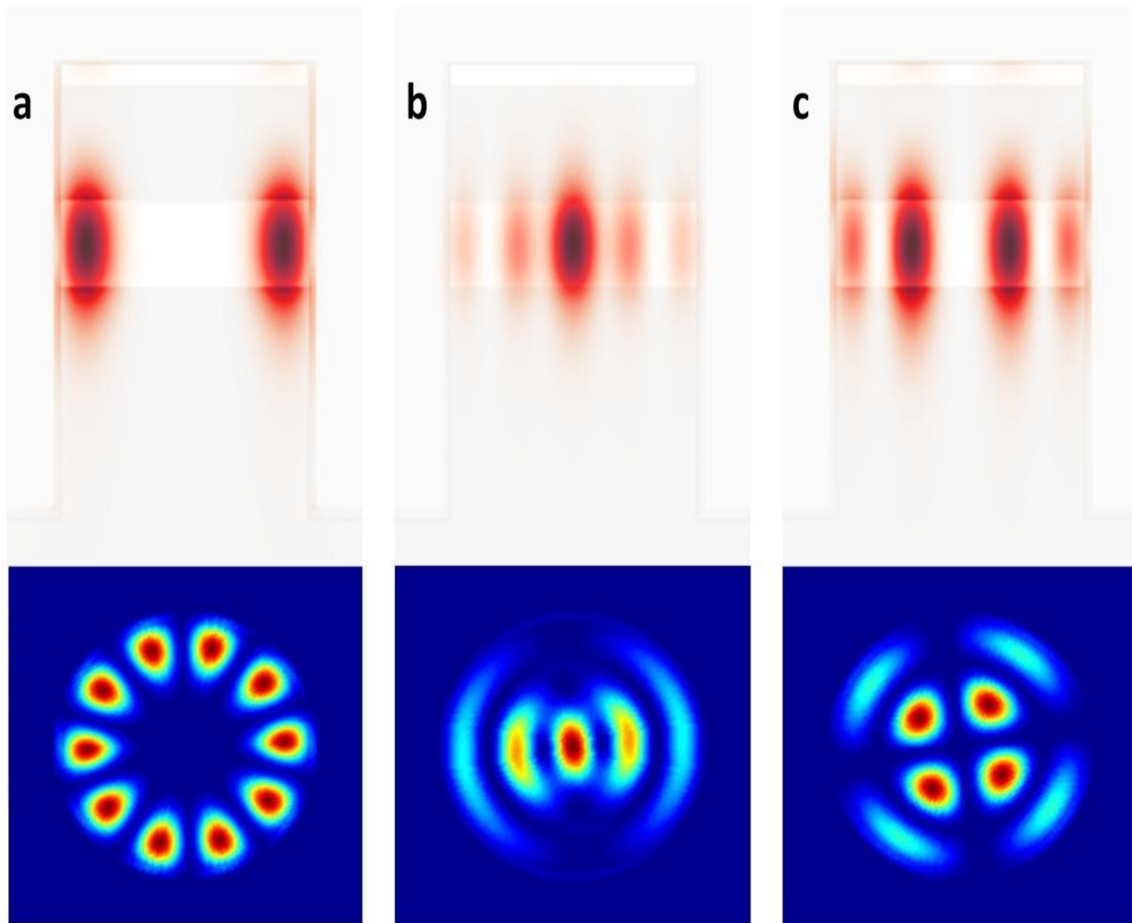

Figure 5.11 Mode patterns $|E|^2$ of a circular device with a radius at 540 nm and SIN thickness at 30 nm **(a)** TM_{51} mode **(b)** HE13 mode and **(c)** EH_{22}. The bottom part of the each figure shows the $|E|^2$ pattern at the cross section plane at the center of InGaAs gain layer.

Mode analysis in these large devices is much more complex than in smaller devices due to this multi-mode operation. Linear mode shift with device size is still observed in large devices as in small devices. Figure 5.12 shows the plot of lasing wavelength versus device diameter. The lasing mode wavelength shifts linearly as device diameter.

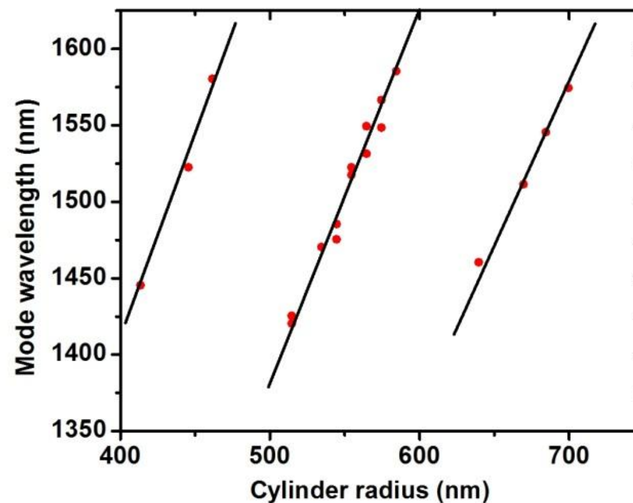

Figure 5.12 Linear dependence of resonance wavelength on diameter in large circular nanolasers

Lasing at room temperature 296K is achieved under pulse current injection (30 ns pulse width and 1MHz repetition rate) on a device with radius of 700nm. The optical cavity volume including SiN layer of this device is 0.77 λ3 (λ=1545 nm). The L-I curve shows a turn-on threshold around 2.5 mA. A significant reduction of linewidth is observed. The FWHM is about 2nm when well below threshold, indicating a quality factor of 773 and at higher pumping current it shrinks down to smaller than 0.5nm which is approaching the resolution limit of our spectrometer.

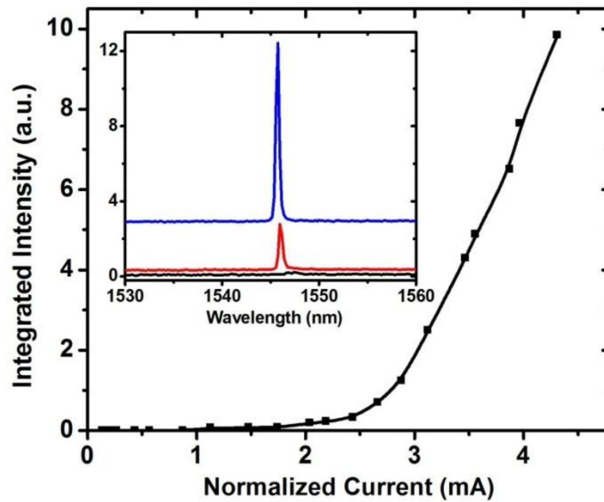

Figure 5.13 L-I curve of a device with radius of 700nm at room temperature (296K) under pulse current injection (30ns pulse width/1MHz repetition rate). The current is normalized. The inset shows the spectra at different currents of 2.13mA (black), 3.07mA (red) and 3.83mA (blue).

5.5 Summary

In this chapter, I discussed the design, fabrication and characterization of metallic cavity nanolasers with circular cross section. Through FDTD simulation, I designed a high Q metallic nanocavity supporting the TE_{01} mode with optimized SiN thickness. A series of circular nanolasers with increasing radius were fabricated and CW single mode lasing at low temperature was achieved. The azimuthal polarization of the TE_{01} mode was experimentally confirmed. These small TE_{01} mode circular nanolasers are also a compact laser source for azimuthally polarized beam which has special applications. The linear shift of cavity resonance wavelength on pillar diameter was observed in experiment as well.

Though room temperature operation is expected based on simulation results, the performance of those circular nanolasers with TE_{01} mode falled far short of simulation prediction. Such performance can be attributed to the bad heat dissipation and surface recombination induced by the thick SiN layer used. Therefore, later on I fabricated large circular nanolaser (radius from 420nm to 730 nm) with thin (30 nm) SiN layer. Multimode operation was often observed in those large devices. Room temperature pulse operation was achieved. Actually, the performance of those very large (radius around 700 nm) circular nanolasers is expected to be better than the best rectangular nanolaser since the Q factor of a circular nanolaser cavity will be generally higher than the rectangular nanolaser cavity. However, only room temperature pulse operation instead of CW operation is achieved on those circular nanolasers. In many cases, the performance of cylindrical nanolasers is not as good as rectangular nanolasers with similar cavity volumes, though simulation shows that the cylindrical nanolasers have lower threshold gain. This outcome could be also related to the surface recombination. In rectangular nanolasers, the surfaces of the semiconductor pillar are along certain crystalline face (011 or $01\bar{1}$). However, in circular nanolasers, many other crystalline faces are exposed at the pillar surface, this may lead to a higher surface recombination than 011 or $01\bar{1}$ face. Again it is demonstrated that the surface recombination will play a critical role in nanolasers, so it should be carefully considered during device design. The trade-off between Q factor and surface recombination is also an important aspect when deciding if rectangular or circular devices are to be fabricated.

CHAPTER 6

NANOLASER MODULATION

6.1 Introduction

In this chapter, I study the modulation of metallic cavity nanolasers. A proposed application for metallic cavity nanolaser is the future on-chip or off-chip optical interconnects which require a power consumption as low as 10 ~ 100 fJ/bit to be competitive with electrical interconnects[86]. To reach such low level of power consumption, the size of semiconductor laser active region needs to shrink to deep sub-wavelength scale of tens of nanometers[87]. In this sense, metallic cavity nanolaser is a promising candidate for this application due to its superior scalability compared to conventional dielectric cavity lasers[88]. There have been quite a few experimental[89,90] or theoretical studies[32-35] on the modulation response of a nanolaser or a nanoLED. In a nanocavity, both simulated emission and spontaneous emission rate is modified by the presence of a nanocavity. I will calculate the simulated emission and spontaneous emission couple to lasing mode in a nanocavity operating at near infrared. After that I will study the data rate and energy consumption of the circular metallic nanolasers (which is discussed in Chapter 5) with laser noise considered.

6.2 Spontaneous and simulated emission in a nanocavity in near infrared

In this section, several text books[91, 92] are consulted with to rigorously derive the expression of spontaneous emission and simulated emission in a cavity. I first consider

the electric field $E(r)$ of a cavity mode with a linewidth of $\Delta\omega_m$

$$|E(r)|^2 = N_{ph}|E_0(r)|^2 \tag{6.1}$$

Here N_{ph} is the number of photons in this mode, and $E_0(r)$ is the amplitude of electrical field corresponding to a single photon whose energy is quantized to $\hbar\omega_m$. When the photon frequency is far below the SPP resonance, for example in the near infrared nanolasers presented in this thesis, its energy can be expressed as:

$$\hbar\omega_m = \int_\infty dV \frac{\varepsilon_0\varepsilon_g(r,\omega_m)}{2}|E_0(r)|^2 \tag{6.2}$$

Here $\varepsilon_g(r,\omega)$ is the material group dielectric constant as:

$$\varepsilon_g(r,\omega) = \left.\frac{\partial[\omega'\varepsilon_R(r,\omega')]}{\partial\omega'}\right|_{\omega'=\omega} \tag{6.3}$$

$\varepsilon_R(r,\omega)$ is the real part of material dielectric constant.

Under the dipole approximation, the interaction Hamiltonian H_{int} is expressed as:

$$H_{\text{int}} = -\mu_{cv}\cdot E(r) \tag{6.4}$$

μ_{cv} is the dipole operator of an electron. The Fermi's golden rule states that the stimulated emission rate (in the unit of 1/s) due to the interaction between this photon and a single dipole at position r is:

$$r_{st,dipole}(r) = \int \frac{2\pi}{\hbar} N_{ph}|\mu_{cv}\cdot E_0(r,\omega)|^2 \rho_m(\hbar\omega_m,\hbar\Delta\omega_m)\delta(\hbar\omega - E_{cv})d(\hbar\omega) \tag{6.5}$$

Here $\rho_m(\hbar\omega_m,\hbar\Delta\omega_m)$ (in the unit of 1/J), the number of mode per unit energy for this mode, is expressed as:

$$\rho_m(\hbar\omega_m, \hbar\Delta\omega_m) = \frac{1}{\pi} \frac{\hbar\Delta\omega_m / 2}{(\hbar\omega - \hbar\omega_m)^2 + (\hbar\Delta\omega_m / 2)^2} \tag{6.6}$$

Using Einstein's relationship, the dipole's spontaneous emission rate (1/s) coupled to this mode can be easily written as:

$$r_{sp,dipole}(r) = \frac{r_{st,cv}(r)}{N_{ph}} = \int \frac{2\pi}{\hbar} |\mu_{cv} \cdot E_0(r, \omega)|^2 \ \rho_m(\hbar\omega_m, \hbar\Delta\omega_m) \delta(\hbar\omega - E_{cv}) d(\hbar\omega) \tag{6.7}$$

In semiconductor the linewidth of electron-hole transition should be considered, and then the delta function in (6.5) and (6.7) should be replaced by the transition lineshape function in (6.8).

$$L_{cv}(E_{cv}, \hbar\Gamma_{cv}) = \frac{1}{\pi} \frac{\hbar\Gamma_{cv} / 2}{(\hbar\omega - E_{cv})^2 + (\hbar\Gamma_{cv} / 2)^2} \tag{6.8}$$

Then the stimulated emission rate of an electron-hole pair in semiconductor $r_{st,cv}(r)$ (1/s) is written as:

$$\begin{aligned} r_{st,cv}(r) &= \frac{\pi}{2\hbar} |\mu_{cv}|^2 \ N_{ph} \, | \, E_0(r) \, |^2 \int_{\infty} d(\hbar\omega) \rho_m(\hbar\omega_m, \hbar\Delta\omega_m) L_{cv}(E_{cv}, \hbar\Gamma_{cv}) \\ &= \frac{\pi}{2\hbar} |\mu_{cv}|^2 \ N_{ph} \, | \, E_0(r) \, |^2 \ \frac{1}{\pi} \frac{\hbar(\Delta\omega_m + \Gamma_{cv}) / 2}{(\hbar\omega_m - E_{cv})^2 + \hbar^2 (\Delta\omega_m + \Gamma_{cv})^2 / 4} \end{aligned} \tag{6.9}$$

The integration of two lineshape function is another lineshape function:

$$L(E_{cv}, \hbar\omega_m) = \frac{1}{\pi} \frac{\hbar(\Delta\omega_m + \Gamma_{cv}) / 2}{(\hbar\omega_m - E_{cv})^2 + \hbar^2 (\Delta\omega_m + \Gamma_{cv})^2 / 4} \tag{6.10}$$

In the same manner, I obtain the spontaneous emission rate (1/s) of an electron-hole pair, written as:

$$r_{sp,cv}(r) = \frac{\pi}{2\hbar} |\mu_{cv}|^2 | \, E_0(r) \, |^2 \ L(E_{cv}, \hbar\omega_m) \tag{6.11}$$

Considering the joint density of state $\rho_{cv}(E_{cv})$ (1/m^3/J) in semiconductors, the total stimulated emission and spontaneous emission rate (both in the unit of 1/s) is obtained by integrating over the active region as:

$$\begin{aligned} R_{st}N_{ph} &= \int_{V_a} |E_0(r)|^2\, dV \int_{E_g}^{\infty} dE_{cv}\rho_{cv}(E_{cv})r_{st,cv}(r)(f_c - f_v) \\ &= \frac{\pi}{2\hbar}|\mu_{cv}|^2\, N_{ph}\int_{V_a} |E_0(r)|^2\, dV \int_{E_g}^{\infty} dE_{cv}\rho_{cv}(E_{cv})L(E_{cv},\hbar\omega_m)(f_c - f_v) \end{aligned} \tag{6.12}$$

and

$$R_{sp,m} = \frac{\pi}{2\hbar}|\mu_{cv}|^2 \int_{V_a} |E_0(r)|^2\, dV \int_{E_g}^{\infty} dE_{cv}\rho_{cv}(E_{cv})L(E_{cv},\hbar\omega_m)f_c(1-f_v) \tag{6.13}$$

Here V_a is the volume of active region. f_c and f_v is the Fermi-Dirac distribution function with quasi-Fermi levels E_{fn} and E_{fp}, respectively.

Using (6.2), the integration term $\int_{V_a} |E_0(r)|^2\, dV$ in both the expressions of R_{st} and $R_{sp,m}$ can be rewritten as:

$$\int_{V_a} |E_0(r)|^2\, dV = \frac{\hbar\omega_m}{\frac{\varepsilon_0\varepsilon_{ga}(\omega_m)}{2}} \frac{\int_{V_a} dV\, \frac{\varepsilon_0\varepsilon_{ga}(\omega_m)}{2}|E_0(r)|^2}{\int_{\infty} dV\, \frac{\varepsilon_0\varepsilon_g(r,\omega_m)}{2}|E_0(r)|^2} \tag{6.14}$$

$\varepsilon_{ga}(r,\omega_m)$ is the material group dielectric constant of the active gain material.

The division of two integral in (6.14) is actually the same as the energy confinement factor Γ_E in (2.18). Then R_{st} and $R_{sp,m}$ are simplified to:

$$R_{st} = \frac{\pi\omega_m}{\varepsilon_0\varepsilon_{ga}(\omega_m)}|\mu_{cv}|^2\, \Gamma_E \int_{E_g}^{\infty} dE_{cv}\rho_{cv}(E_{cv})L(E_{cv},\hbar\omega_m)(f_c - f_v) \tag{6.15}$$

$$R_{sp,m} = \frac{\pi\omega_m}{\varepsilon_0\varepsilon_{ga}(\omega_m)}|\mu_{cv}|^2\, \Gamma_E \int_{E_g}^{\infty} dE_{cv}\rho_{cv}(E_{cv})L(E_{cv},\hbar\omega_m)f_c(1-f_v) \tag{6.16}$$

6.3 Models

6.3.1 Rate Equation model

The rate equations with total carrier number N and total photon number N_{ph} for a single mode nanolaser can be written as following:

$$\frac{dN}{dt} = \frac{I}{e} - R_{nr} - R_{sp} - R_{st} N_{ph} \tag{6.17}$$

$$\frac{dN_{ph}}{dt} = -\frac{N_{ph}}{\tau_{ph}} + R_{sp,m} + R_{st} N_{ph} \tag{6.18}$$

$$R_{sp} = R_{sp,m} + R_{sp,fs} \tag{6.19}$$

Here I is the injection current. R_{sp}, $R_{st}N_{ph}$, and R_{nr} are the total spontaneous emission rate, stimulated emission rate and non-radiative recombination rate respectively. τ_{ph} is photon life time, expressed as $\tau_{ph} = Q/\omega_m$ where Q is cavity quality factor and ω_m is mode resonance frequency. As shown in (6.19), R_{sp} has two parts, one is the spontaneous emission coupled to lasing mode($R_{sp,m}$), the other is the spontaneous emission coupled to leakage mode into free space $R_{sp,fs}$. R_{st} and $R_{sp,m}$ have been derived in (6.15) and (6.16).

In a cavity, the spontaneous emission to leakage mode is in general also strongly modified by the cavity, which makes the calculation of $R_{sp,fs}$ usually nontrivial[93]. Strong suppression of leakage mode spontaneous emission has been observed in ultra-small metallic cavity nanolasers[15,21]. It is reasonable to assume that the ratio of $R_{sp,fs}$ to $R_{sp,fs0}$ (spontaneous emission rate in an infinitely large bulk semiconductor) will increase with laser volume linearly and saturate to unit at a certain large laser volume. Here I assume

$$R_{sp,fs} = \begin{cases} \dfrac{V_a}{(\lambda / n_r)^3} R_{sp,fs0} & V_a < (\lambda / n_r)^3 \\ R_{sp,fs0} & V_a \geq (\lambda / n_r)^3 \end{cases} \tag{6.20}$$

Considering the bulk semiconductor photon density of state $\rho(\nu) = \frac{8\pi n_r^3}{c^3}\nu^2$, the spontaneous emission in bulk semiconductor $R_{sp,fs0}$ is:

$$R_{sp,fs0} = \frac{n_r V_a}{\pi \varepsilon_0 \hbar c^3} |\mu_{cv}|^2 \int_{E_g}^{\infty} dE_{cv} \omega^3 \rho_{cv}(E_{cv}) L_{cv}(E_{cv}, \hbar\Gamma_{cv}) f_c (1 - f_v) \tag{6.21}$$

6.3.2 Nanolaser model

I use this rate equation model to study the circular metallic cavity nanolaser supporting high Q TE_{0m} (m = 1, 2, 3…) modes that I have fabricated[94] and discussed in Chapter 5. Laser structure is shown again in Fig. 6.1a. In such the laser, the mode wavelength and Q factor are functions of pillar diameter and the TE_{0m} mode at 1.55 µm wavelength is only supported in devices with certain pillar diameters. However, in order to discuss the laser modulation over a continuous size range, I assume a TE_{0x} mode at a fixed wavelength of 1.55 µm in such a circular nanolaser with any diameter. In Fig. 6.1b, I plot the simulated Q factor and energy confinement of several TE_{0m} modes at 1.55 µm. When simulating the laser Q factor, I excluded the cavity radiation, so such Q factor only consists of absorption loss from metal. Apparently, this Q factor is linear to the cavity diameter. Therefore I assume the Q factor of TE_{0x} mode also follows this trend and can be calculated as: Q = $681d/d_0$, where $d_0 = 460$ nm.

As can be seen in (6.15) and (6.16), R_{st} and $R_{sp,m}$ only depend on mode energy confinement factor and carrier pumping level. The energy confinement factor of the TE_{0m}

modes plotted in Fig. 6.1b varies slowly with cavity size. Therefore R_{st} and $R_{sp,m}$ are actually almost independent of cavity size for this type of laser, which means the emission rate per unit volume, or R_{st}/V_a and $R_{sp,m}/V_a$, are enhanced in small lasers compared to large lasers under the same pumping level.

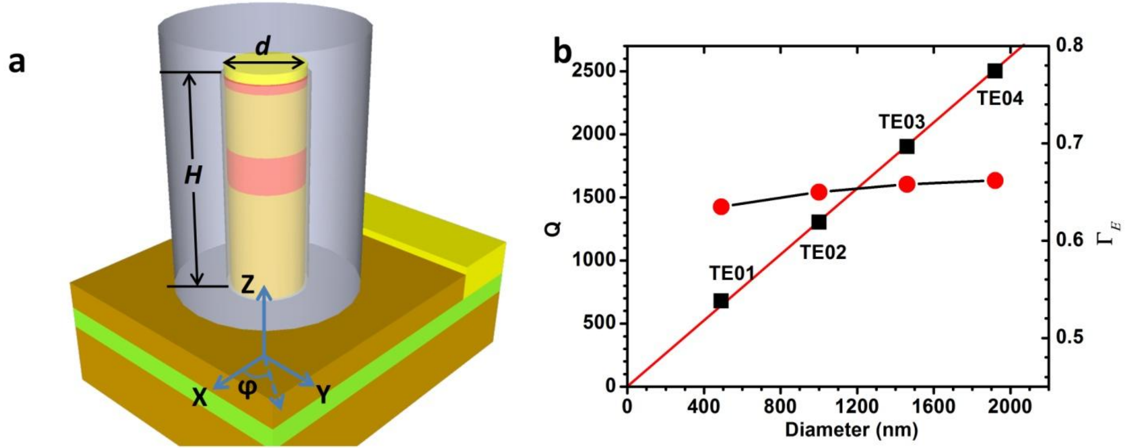

Figure 6.1 (a) Schematic of the high Q cylindrical metallic cavity nanolaser studied in this paper. (b) Q factors (black ■) and energy confinement factor (red ●) of TE_{01}, TE_{02}, TE_{03}, and TE_{04} mode.

For the non-radiative recombination in this laser, I only consider the surface recombination as:

$$R_{nr} = 4v_s N / d \tag{6.22}$$

I set the surface recombination velocity v_s to 1.5×10^4cm/s, which is the lowest surface recombination for InGaAs I found in literature[55].

I solve the steady state rate equations for this nanolaser. The calculated L-I curve and linewidth for a 460 nm diameter laser are plotted in Fig. 6.2a. The L-I curve shows a clear S shape under log-log scale. Figure 6.2b shows the spectrum of spontaneous emission coupled to lasing mode in this laser under a 25 μA injection current. The

spontaneous emission spectrum in bulk InGaAs with the same carrier density and volume is also plotted as a comparison. Spontaneous emission to lasing mode in cavity is enhanced by a factor of 3.94 compared to in bulk material. Here I define the laser threshold current as the total wasted current consumed by spontaneous emission, non-radiative recombination at the carrier density level that semiconductor optical gain can fully compensate for cavity loss[95], or more specifically $R_{st} = 1/\tau_{ph}$. Under this definition, the laser threshold current density as shown in Fig. 6.2c increases as device size shrinks due to the reduced Q factor and increased surface recombination. Actually our calculation shows that when the diameter reduces to 40 nm, the device Q factor is only 60 that the optical gain in semiconductor cannot fully compensate for the cavity loss, which means the device is only a LED, not a laser anymore. As a trade-off between threshold current density and laser cross section area, the smallest threshold current occurs in the laser with a diameter around 240 nm. The spontaneous emission factor written as $\beta = \frac{R_{sp,m}}{R_{sp}}$ is plotted in Fig. 6.2d as a function of diameter. β is approaching unit as the laser size reduces but apparently this does not result in a thresholdless laser, which is shown in Fig. 6.2c.

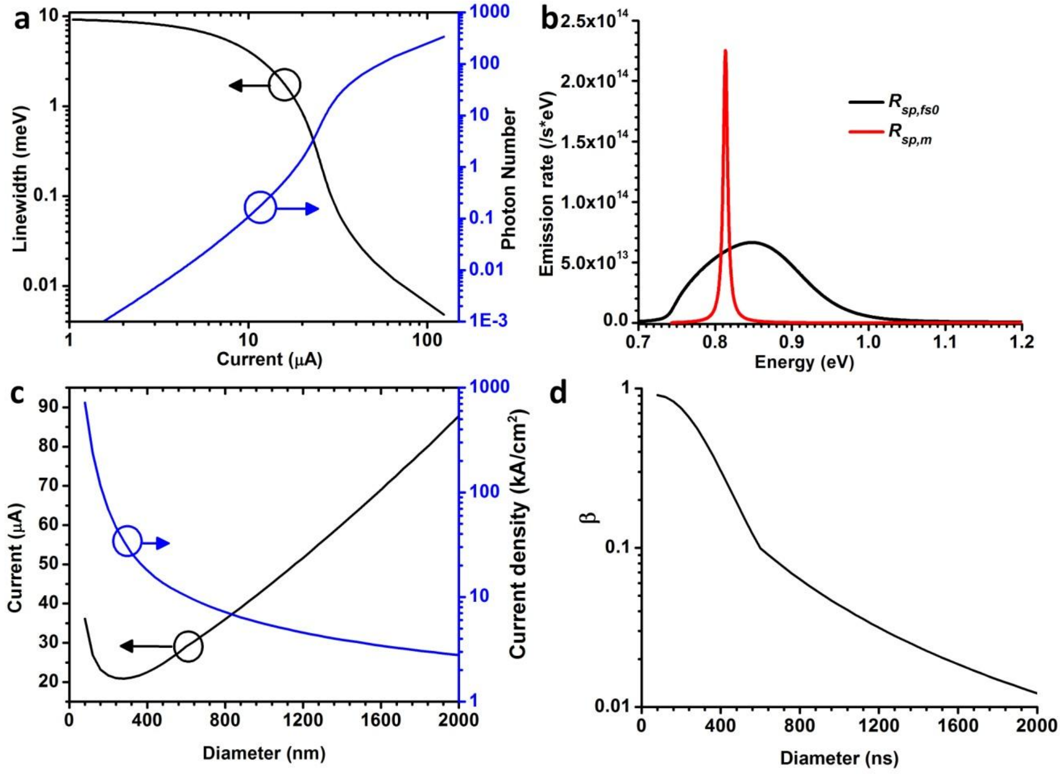

Figure 6.2 **(a)** Calculated L-I curve and linewidth for a 460 nm diameter laser. **(b)** Spectrum of spontaneous emission coupled to lasing mode ($R_{sp,m}$) in this laser under a 25 μA injection current and spontaneous emission in bulk InGaAs ($R_{sp,fs0}$) with the same carrier density. **(c)** Calculated threshold and threshold current density and **(d)** spontaneous emission factor β for TE_{0x} mode.

6.4 Laser modulation

6.4.1 Analog and digital modulation, and the energy consumption

Under small signal modulation, the laser relaxation resonance frequency ω_R and modulation transfer function $H(\omega)$ are defined by[68]

$$\omega_R^2 = \gamma_{NP}\gamma_{PN} + \gamma_{NN}\gamma_{PP} \tag{6.23}$$

$$H(\omega) = \frac{\omega_R^2}{\omega_R^2 - \omega^2 + j\omega\gamma} \tag{6.24}$$

γ is the damping factor as $\gamma = \gamma_{NN} + \gamma_{PP}$ and

$$\begin{aligned}
\gamma_{NN} &= \frac{dR_{nr}}{dN} + \frac{dR_{sp}}{dN} + N_{ph}\frac{dR_{st}}{dN} \\
\gamma_{NP} &= R_{st} \\
\gamma_{PN} &= \frac{dR_{sp,m}}{dN} + N_{ph}\frac{dR_{st}}{dN} \\
\gamma_{PP} &= -R_{st} + \frac{1}{\tau_{ph}}
\end{aligned} \tag{6.25}$$

The 3dB bandwidth is written as:

$$\begin{aligned}
\omega_{3dB}^2 &= \omega_P^2 + \sqrt{\omega_P^4 + \omega_R^4} \\
f_{3dB} &= \omega_{3dB}/2\pi
\end{aligned} \tag{6.26}$$

where $\omega_P^2 = \omega_R^2\left[1 - \frac{1}{2}(\gamma/\omega_R)^2\right]$.

For small signal modulation, modulation part of the energy can be ignored. A figure of merit to evaluate the energy consumption is the total power consumption dived by modulation bandwidth as (power bandwidth rate, *PBR*):

$$PBR = \frac{P_{in.cw}}{f_{3dB}} \tag{6.27}$$

The CW input power $P_{in.cw}$ is used as total power consumption.

$$P_{in.cw} = I(E_{fn} - E_{fp}) \tag{6.28}$$

which is the injection current multiplied by the separation between quasi-Fermi levels of electron and hole.

This 3dB bandwidth can be a good indication of how fast the nanolaser can be modulated. For digital modulation, the maximum data rate is more directly determined by the laser output turn on and turn off delay time under large digital signal modulation and the signal quality required by specific bit error rate.

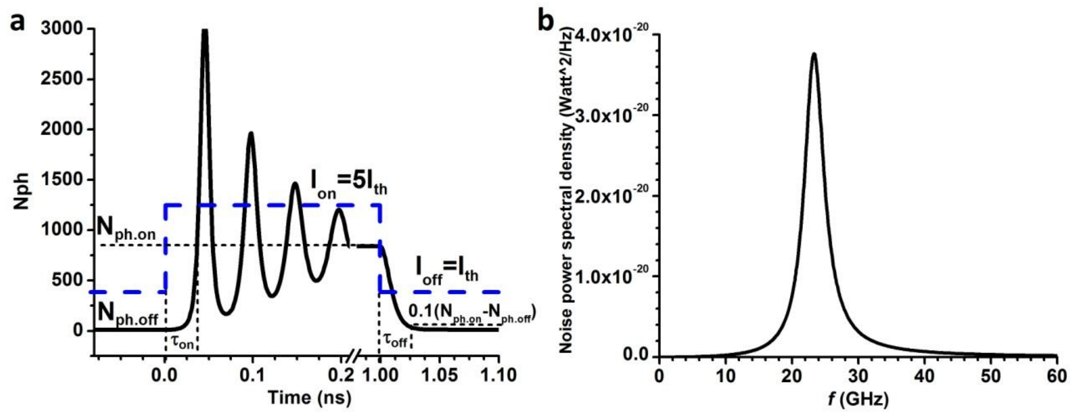

Figure 6.3 **(a)** Calculation example of photon number variation of a semiconductor laser under a 1 ns wide current pulse excitation from threshold current to 5 times threshold current. **(b)** Calculation example of output noise power spectral density of a laser.

Figure 6.3a shows the calculated photon number variation of a semiconductor laser under a 1 ns wide current pulse excitation from threshold current (off state) to 5 times threshold current (on state). At the rise edge, the photon number will over shoot first and then oscillate and stabilize to on state $N_{ph.on}$. At the falling edge, N_{ph} gradually drops to off state $N_{ph.off}$. The turn-on time τ_{on} is defined as the time for the photon number to reach on state number for the first time. The turn-off time τ_{off} is defined as the time that photon number drops to 10% of ($N_{ph.on}$-$N_{ph.off}$) above $N_{ph.off}$. For non-return to zero (NRZ) data format, there is at most only one rising or falling edge in one data period, therefore I set the longer one of τ_{on} and τ_{off} as the total delay time τ_d of a laser under digital signal modulation.

The bit error rate of NRZ format optical signal is given by Ref.96

$$P(E) = \frac{1}{2} \mathrm{erfc}(Q_s / \sqrt{2}) \qquad (6.29)$$

where Q_s is the signal quality defined as

$$Q_s = \frac{P_{on} - P_{off}}{\sigma_{on} + \sigma_{o\,f\,j}} \tag{6.30}$$

P_{on}, P_{off}, σ_{on} and σ_{off} are the output signal power and output noise power at on and off state respectively. To reach a bit error rate of 10^{-12}, Q_s has to be larger than 7.13.

To calculate the output noise power σ, the Langevin's noise source of carrier $F_n(t)$ and photon $F_p(t)$ can be introduced to the original rate equations as:

$$\begin{aligned} \frac{dN}{dt} &= \frac{I}{q} - R_{nr} - R_{sp} - R_{st}N_{ph} + F_n(t) \\ \frac{dN_{ph}}{dt} &= -\frac{N_{ph}}{\tau_p} + R_{sp,m} + R_{st}N_{ph} + F_p(t) \end{aligned} \tag{6.31}$$

Following the procedure in Ref. 68, the photon noise power spectral density is expressed as:

$$\begin{aligned} S(\omega) &= \frac{1}{2\pi}\int < N_{ph}(\omega)N_{ph}(\omega')^* > d\omega' \\ &= \frac{\left|H(\omega)\right|^2}{\omega_R^4}[(\gamma_{NN}^2 + \omega^2) < F_pF_p > + 2\gamma_{NN}\gamma_{PN} < F_pF_n > + \gamma_{PN}^2 < F_nF_n >] \end{aligned} \tag{6.32}$$

The Langevin noise source spectral densities and their cross spectral densities are defined by:

$$< F_iF_j >= \int < F_i(t)F_j(t-\tau)^* > \exp(-j\omega\tau)d\tau \tag{6.33}$$

and can be calculated by counting the rates into and out of the carrier and photon reservoirs as[97]:

$$< F_pF_p >= N_{ph}/\tau_p + R_{sp,m} + (R_{12} + R_{21})N_{ph} \tag{6.34}$$

$$< F_pF_n >= -R_{sp,m} - (R_{12} + R_{21})N_{ph} \tag{6.35}$$

$$< F_nF_n >= I/q + R_{nr} + R_{sp} + (R_{12} + R_{21})N_{ph} \tag{6.36}$$

Here R_{12} and R_{21} is the rate of electron up and down transitions between conduction band and valence band respectively.

$$R_{21} = \frac{\pi\omega_m}{\varepsilon_0 \varepsilon_{Ea}(\omega_m)} |\mu_{cv}|^2 \, \Gamma_E \int_{E_g}^{\infty} dE_{cv} \rho_{cv}(E_{cv}) L(E_{cv}, \hbar\omega_m) f_c (1 - f_v) \tag{6.37}$$

$$R_{12} = \frac{\pi\omega_m}{\varepsilon_0 \varepsilon_{Ea}(\omega_m)} |\mu_{cv}|^2 \, \Gamma_E \int_{E_g}^{\infty} dE_{cv} \rho_{cv}(E_{cv}) L(E_{cv}, \hbar\omega_m) (1 - f_c) f_v \tag{6.38}$$

$$R_{st} = R_{21} - R_{12} \tag{6.39}$$

If output partition noise is not considered, the photon density noise spectral density can be converted to the output power noise spectral density by:

$$S_P(\omega) = \left(\frac{h\upsilon}{\tau_{rad}}\right)^2 S(\omega) \tag{6.40}$$

Here τ_{rad} is the photon radiation lifetime expressed as $\tau_{rad} = Q_{rad}/\omega_m$ and Q_{rad} is the cavity radiation Q factor, which I assume is 3000 here.

Figure 6.3b shows a calculation example of semiconductor laser output noise power spectral density. Then in a $\Delta\omega$ bandwidth system, the output noise power is

$$\sigma = \frac{1}{2\pi} \int_{-\Delta\omega}^{\Delta\omega} S_p(\omega) d\omega \tag{6.41}$$

Plugging in the expression of output noise power in (6.32),(6.40) and (6.41), the maximum modulation bandwidth of a laser restricted by noise can be obtained by searching the maximum integration limit $\Delta\omega$ that keeps $Q_s \geq 7.13$. In NRZ data format, the noise limited Data rate is $D_n = 2\Delta\omega$.

The final laser data rate considering both delay time and noise can be estimated by:

$$DR = \frac{1}{\tau_d + 1/D_n} \quad (6.42)$$

Under NRZ format, if we assume half ones and half zeros in a long train of signal, the average energy consumption per bit (energy bit rate, *EBR*) is:

$$EBR = \frac{0.5(P_{in.on} + P_{in.off})}{DR} \quad (6.43)$$

$P_{in.on}$ and $P_{in.off}$ are the input power at on and off states. For simplicity, I use the CW power calculated by (6.28) as an approximation.

6.4.2 Calculation results

Figure 6.4a shows the calculated small signal 3dB bandwidth as a function of laser cavity diameter and injection current density. At a high injection current density of 900-1000 kA/cm^2, the 3dB bandwidth for an 800 nm diameter laser can be larger than 150 GHz. For very small nanolasers with a diameter smaller than 200 nm, the 3dB bandwidth is limited to 80 GHz even under high injection current density. *PBR* shown in Fig. 6.4b generally increases with laser size and injection current. Small laser with a diameter around 200 nm shows a low *PBR* around 1-2 fW/Hz. But if the laser diameter further reduces to 100 nm, *PBR* increases to 5-20 fW/Hz due to the reduce 3dB bandwidth. One reason for the speed limitation in small lasers is the increased threshold current density, and thus decreased excess current density beyond the threshold, since such excess current density determines the modulation bandwidth. Another interesting aspect can be learned from Fig. 6.4a is that the minimum current density for high-bandwidth modulation (>100

GHz) occurs around 1 micron diameter and shifts to smaller sub-micron diameter for higher bandwidth.

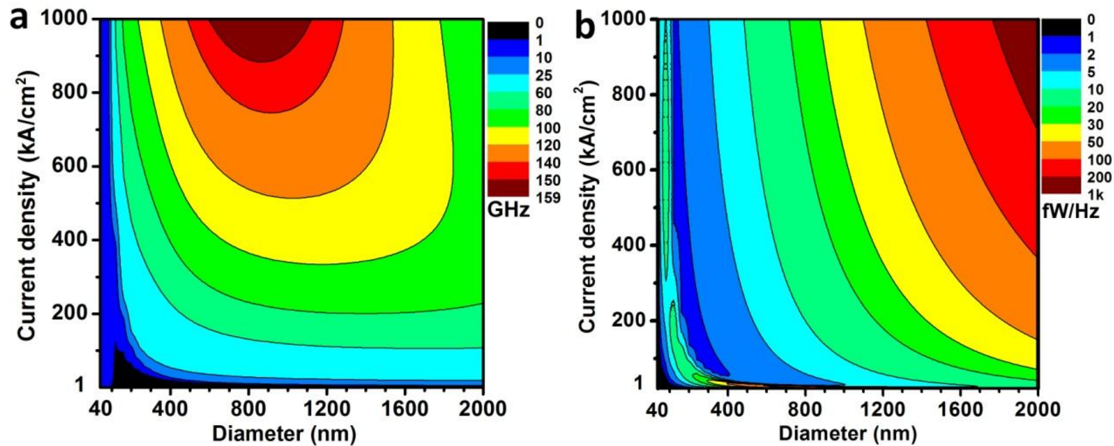

Figure 6.4 Contour plot of **(a)** Small signal 3dB bandwidth and **(b)** PBR.

When calculating the large digital signal modulation, I set the laser threshold as the off-state. Figure 6.5a shows contour plot of the reversed laser delay time under digital modulation. The trend showed in this figure is similar to Fig. 6.4a that the fastest modulation is for lasers with a diameter around 800 nm driven by a large on-state current density of 900-1000 kA/cm^2 instead of the ultra-small lasers. Figure 6.5b shows the noise limited laser data rate. At the same injection current density, the noise limited laser data rate will increase with laser size due to increased output power. Noise is apparently an important limiting factor for the modulation of smaller lasers. When the lasers diameters reduce to 400 nm, the data rate is limited to around 50 Gbit/s by noise. For nanolasers with diameters around or smaller than 200 nm, the noise limited data rate further drops to below 10 Gbit/s.

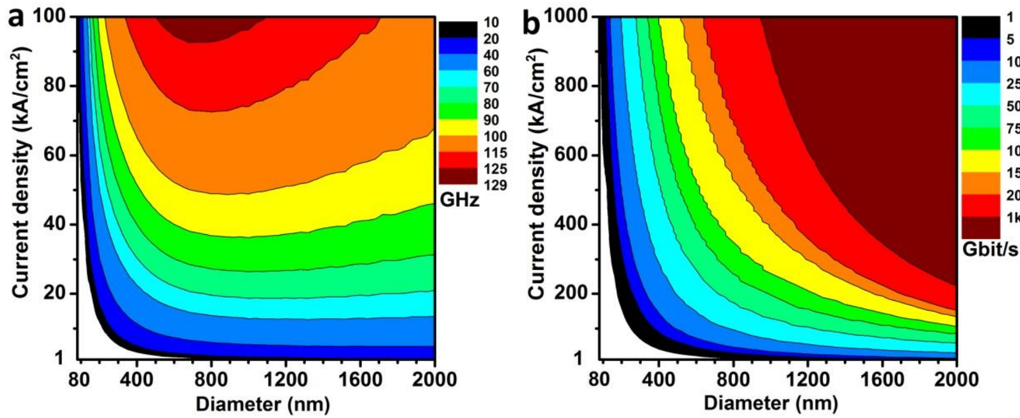

Figure 6.5 Contour plot of **(a)** $1/\tau_d$ under digital modulation and **(b)** D_n

Calculated laser data rate and energy per bit are plotted in Fig. 6.6. Due to the effect of noise, the diameter of the laser with highest data rate shifts from 800 nm in 3dB bandwidth plot to 1200 nm. For such lasers with a active region volume of 3.58 $(\lambda/n_r)^3$, the data rate can be up to around 120 Gbit/s at a large on-state current density of 900-1000 kA/cm^2 and an EBR of 30-40 fJ/bit. In terms of energy consumption, the lasers with a diameter around 400 nm ($V_a = 0.1(\lambda/n_r)^3$) show the lowest EBR below 10 fJ/bit, but *DR* is limited to 10-40 Gbit/s.

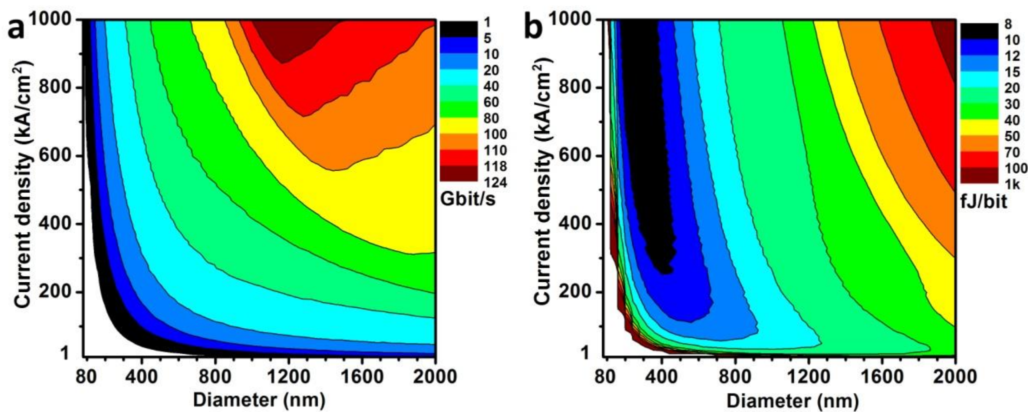

Figure 6.6 Contour plots of **(a)** *DR* and **(b)** EBR

6.5 Summary and discussion

In this chapter, I calculated the data rate and energy consumption per bit of the circular metallic nanolaser under digital modulation. Cavity Q factor and spontaneous emission factor are considered as size dependent factors to resemble a real nanolaser in practice. The size effect on the laser modulation and energy per bit is not monotonic. As we can see from the plots of small signal 3dB bandwidth in Fig. 6.4a, large signal delay time in Fig. 6.5a and digital data rate in Fig. 6.6a, the fasted operation are all achieved in a moderate cavity size which is around 800 nm diameter for the first two and shifts to 1200 nm when noise effect is included. The speed of ultra-small lasers is actually limited. The final result shows that the size of the fastest nanolaser (d = 1200 nm, *DR* ~ 120 Gbit/s) actually exceeds 1 μm to obtain an optimum combination of both low threshold and enhanced optical process. If high data rate is not a critical requirement, small active region volume is still a very important factor to achieve low energy consumption per bit. The calculation demonstrates low energy consumption below 10 fJ/bit in lasers with diameter around 400 nm though *DR* is limit to 10 - 40 Gbit/s. High data rate and low energy per bit cannot be achieved simultaneously, therefore carefully choosing the right device size to meet the application specification is required.

This speed-size trend can be attributed to several factors. First, enhanced stimulated emission and spontaneous emission as I discussed in section 6.3.2 leads to shorter carrier lifetime, which is in favor of fast speed. The large surface recombination can also help this process. But on the other hand, small device size will increase threshold current

density. Therefore modulation speed of small lasers is limited by decreased excess current density beyond the threshold which strongly affects the modulation bandwidth. Noise is another important factor the limit the modulation speed of nanolasers due to the low output power in such lasers. A straight forward strategy to achieve high data rate in small nanolaser is to reduce the threshold current density so that lasers can be operated far above threshold and obtain higher output power. As discussed in Chapter 3, well passivating the semiconductor surface to reduce surface recombination and improving silver optical quality to reduce metal loss and improve cavity Q factor are the two ways to reduced threshold current of a metallic cavity nanolaser.

CHAPTER 7

SUMMARY AND DISCUSSION

7.1 Introduction

This chapter summarizes my thesis work. In addition, prospects for future research in the area of metallic cavity nanolasers are also presented.

7.2 Advantages of metallic cavity nanolasers

There are two main driving forces behind the development of a nanolaser. First, these lasers can provide a platform to study the fundamental light-matter interaction physics in deep sub-wavelength scale. Second, an ultra-small low power laser is highly demanded in many practical applications, such as chemical and biological detection, data storage, and IC interconnects. As discussed in Chapter 1, metallic cavity nanolasers are superior to conventional dielectric cavity lasers in many respects. The metal shell can strongly confine light into deep sub-wavelength scales. This strong confinement has three benefits for photonic devices compared to dielectric photonics: large confinement factor in active core region, minimal cross talk between adjacent devices, and a reasonably large cavity Q factor. Furthermore, the high thermal conductivity metal can effectively remove heat from the active region, leading to superb laser thermal performance.

7.3 Key results in this thesis

The main goal of this project is to achieve room temperature CW operation of a sub-wavelength size metallic cavity laser under electrical injection. To this end, I

designed two types of metallic cavity nanolasers with rectangular or circular cross section. Cavity size is larger than the half wavelength diffraction limit in order to support the low loss dielectric TE mode. Device size can be shrunk down to below diffraction limit by utilizing the plasmonic mode. As discussed in Chapter 2, such miniaturization is at the cost of large cavity loss and high threshold, which are not desired in practical applications. On the other hand, slightly large lasers supporting dielectric TE mode is a good trade-off between laser size and performance. I have demonstrated CW lasing in small rectangular (400 nm (W) $\times$ 900 nm (L) $\times$ 1.5 μm (H) = 0.19 λ^3, λ = 1454 nm) and circular lasers (cavity radius 295 nm, total volume 0.146 λ^3, λ = 1416 nm) at 78 K. Eventually, room temperature CW operation is demonstrated in a large rectangular laser with total size of 1.15 (W) $\times$ 1.39 (L) $\times$ 1.7 (H) μm^3 = 0.67 λ^3, λ = 1591 nm. Circular nanolaser with azimuthal polarization has also been designed and fabricated. Azimuthally polarized laser beam has been verified experimentally. Such small cylindrical nanolasers provide a compact azimuthal polarization source which can have interesting applications in high resolution imaging and particle trapping.

7.4 Fabrication challenges

Though simulation results give us high expectation for the performance of metallic cavity nanolasers, real device performance from experiment often fall far short of the theoretical predictions. An important reason for the under-performance is imperfections in fabrication. The challenges in fabrication include how to precisely transfer the design

geometry to real device through fabrication, how to reduce semiconductor surface recombination, and how to reduce ohmic loss in silver. In this project, intensive efforts have been made to address these three primary challenges. HSQ electron beam resist is used to improve lithography resolution; dry etching process is optimized to obtain vertical and smooth etching sidewall; specific semiconductor surface cleaning and dielectric deposition process have been developed to remove surface damage and to passivate surface state which results in significant reduction of surface recombination; silver deposition and post-annealing process is refined to improve silver optical quality. Even with this progress, further technology development is needed to overcome these fabrication challenges and improve device performance so as to meet the requirement of real applications.

7.5 Future research and nanolaser-waveguide integration

One of the potential problems for using such nanolasers is the poor far-field divergence. In general, the divergence angles of the output increase dramatically when the overall lasers are shrunk down to sub-micron or deep sub-wavelength sizes. Such poor far-field pattern combined with the overall small output power renders such lasers a poor candidate for far-field application or coupling to an application interface. Thus mechanism has to be studied as to how such nanolasers will be used in a real application. Direct integration of nanolasers with other devices on the same platform is the most desired form. Silicon based optoelectronics integration offers the promise of low cost and

compact package solution for optical communications and interconnects. An electrically pumped light source on silicon is a key element needed for integrated photonic circuits on silicon. In Chapter 6, I have demonstrated the feasibility of using metallic cavity nanolasers as light sources for optical interconnect by calculating the data rate and energy consumption. Another part of research to realize this application would be to achieve the integration of nanolaser with silicon passive photonics such as waveguides. III-V-silicon hybrid lasers have been demonstrated[98]. Researchers bonded the III-V active material to pre-patterned silicon-on-insulator waveguides by direct wafer bonding and fabricate lasers on this wafer. Halioua *et al* has also demonstrated a hybrid III-V/silicon nanolaser using a similar heterogeneous integration technology[99].

A possible design to integrate the nanolaser device with silicon waveguide is shown in Fig. 7.1. A nanolaser will sit on top of a silicon waveguide in silicon on insulator (SOI) substrate. Emissions that escape from the bottom of the device will be coupled to the silicon waveguide. This design is proposed because the fabrication of such device is practical as shown in Fig. 7.2. The silicon waveguide is fabricated in SOI wafer using general photolithography and RIE process. The InGaAs and InP is first picked up by a PDMS stamp and then the InP substrate is removed via chemical wet etching. An InGaAs etching stop layer is added to facilitate this substrate removal. Finally the remaining InGaAs/InP on PDMS stamp is transferred to the SOI substrate, after which I can start the nanolaser fabrication as before. The advantage of this process is that the membrane transfer process[100] has proven to be a more effective and high yield process than wafer

bonding. It does not require the surface flatness or smoothness of the bonded wafers like direct wafer bonding technique, thus it is especially suitable for bonding membranes on substrates with pattern structures (e.g., waveguides). It does not require an extra adhesive layer either to avoid the heat dissipation problem as in the Benzocyclobutene (BCB) bonding technique[99]. The development of such integration technology will be of great importance for the final implementations of nanolasers in practical applications.

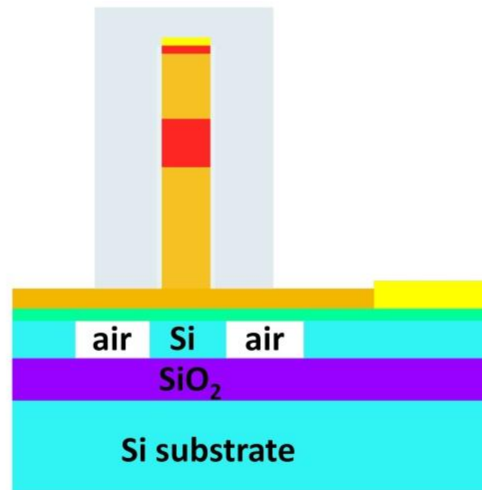

Figure 7.1 Structure of a nanolaser/silicon waveguide integration.

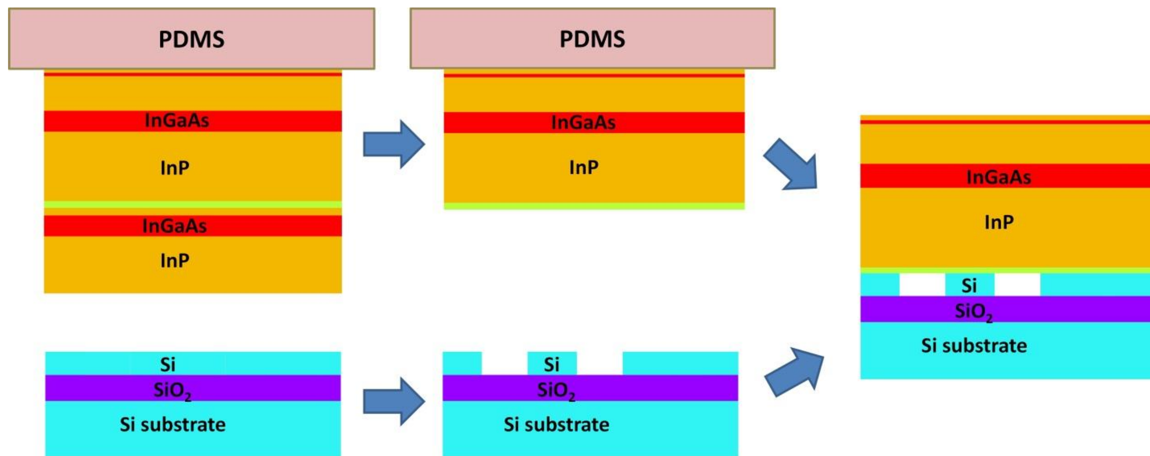

Figure 7.2 A proposed membrane transferring process for III-V/silicon waveguide integration

APPENDIX

PERTURBATION CALCULATION FOR METALLIC WAVEGUIDES

In this appendix, I will describe the perturbation method that I use in Chapter 2 to calculate the modal dispersion of MSM, MSA waveguide. The perturbation calculation for the symmetric TM mode in MSM waveguide is presented here as an example.

For the symmetric TM mode, I obtained a dispersion equation of

$$f = \frac{k_s}{\varepsilon_s}\tanh(k_s d) + \frac{k_m}{\varepsilon_m} = 0 \quad \text{(A.1)}$$

I also have

$$\beta_z - k_{s,m}^2 = \beta_{s,m}^2 \quad \text{(A.2)}$$

The metal dielectric constant ε_m is a complex number expressed as

$$\varepsilon_m = \varepsilon_{mr} + j\varepsilon_{mi} \quad \text{(A.3)}$$

Because of the imaginary part of ε_m, k_s, k_m and β_z are all complex numbers as:

$$k_s = k_{sr} + jk_{si} \quad \text{(A.4)}$$

$$k_m = k_{mr} + jk_{mi} \quad \text{(A.5)}$$

$$\beta_z = \beta_{zr} + j\beta_{zi} \quad \text{(A.6)}$$

For silver, $|\varepsilon_{mi}| \ll |\varepsilon_{mr}|$ in near infrared. Therefore, it is reasonable to assume:

$|k_{si}| \ll |k_{sr}|$, $|k_{mi}| \ll |k_{mr}|$ and $|\beta_{zi}| \ll |\beta_{zr}|$.

k_{sr}, k_{mr} and β_{zr} are obtained approximately by solving (A.1) and (A.2) with $\varepsilon_m \approx \varepsilon_{mr}$, which are:

$$\frac{k_{sr}}{\varepsilon_s}\tanh(k_{sr}d)+\frac{k_{mr}}{\varepsilon_{mr}}\approx 0 \tag{A.7}$$

$$\beta_{zr}-k_{sr,mr}^2\approx\beta_{s,mr}^2 \tag{A.8}$$

To obtain k_{si}, k_{mi} and β_{zi}, I expand (A.1) using first order Taylor series as:

$$df\approx\frac{\partial f}{\partial k_s}\cdot ik_{si}+\frac{\partial f}{\partial k_m}\cdot ik_{mi}+\frac{\partial f}{\partial \varepsilon_m}\cdot i\varepsilon_{mi}=0 \tag{A.9}$$

I substitute k_s, k_m and β_z in (A.2) with (A.4)-(A.6), ignore the small terms of k_{si}^2, k_{mi}^2 and β_{zi}^2, and consider (A.6), then I obtain

$$\beta_{zr}\cdot j\beta_{zi}-k_{sr}\cdot jk_{si}\approx 0 \tag{A.10}$$

$$\beta_{zr}\cdot j\beta_{zi}-k_{mr}\cdot jk_{mi}\approx i\varepsilon_{mi}\beta_0^2 \tag{A.11}$$

(A.9) - (A.11) are all linear equations and can be solved combined as (A.12) to obtain k_{si}, k_{mi} and β_{zi}.

$$\begin{pmatrix}\frac{\partial f}{\partial k_s} & \frac{\partial f}{\partial k_m} & 0\\ -k_{sr} & 0 & \beta_{zr}\\ 0 & -k_{mr} & \beta_{zr}\end{pmatrix}\begin{pmatrix}k_{si}\\ k_{mi}\\ \beta_{zi}\end{pmatrix}=\begin{pmatrix}-\frac{\partial f}{\partial \varepsilon_m}\cdot\varepsilon_{mi}\\ 0\\ \varepsilon_{mi}\beta_0^2\end{pmatrix} \tag{A.12}$$

For different waveguide or different modes, corresponding dispersion equations, for example (2.22) and (2.34) for TM_z and TE_z mode in MSA waveguide, can be used as (A.1) to obtain the modal dispersion with the same method discussed here.

REFERENCES

1. P. Mühlschlegel, H. -J. Eisler, O. J. F. Martin, B. Hecht, and D. W. Pohl, “Resonant optical antennas,” *Science* **308**, 1607 (2005).

2. H. A. Atwater and A. Polman, “Plasmonic for improved photovoltaic devices,” *Nat. Mater.* **9**, 205 (2010).

3. N. A. Hatab, C.-H. Hsueh, A. L. Gaddis, S. T. Retterer, J.-H. Li, G. Eres, Z. Zhang, and B. Gu, “Free-standing optical gold bowtie nanoantenna with variable gap size for enhanced Raman spectroscopy,” *Nano Lett*. **10**, 4952 (2010).

4. B. J. Roxworthy, K. D. Ko, A. Kumar, K. H. Fung, E. K. C. Chow, G. L. Liu, N. X. Fang, and K. C. Toussaint, Jr., “Application of plasmonic bowtie nanoantenna arrays for optical trapping, stacking, and sorting,” *Nano Lett*. **12**, 796 (2012).

5. A. Sundaramurthy, P. J. Schuck, N. R. Conley, D. P. Fromm, G. S. Kino, and W. E. Moerner, “Toward nanometer-scale optical photolithography: utilizing the near-field of bowtie optical nanoantennas,” *Nano Lett*. **6**, 355 (2006).

6. F. Lopez-Tejeira, S. G. Rodrigo, L. Martin-Moreno, F. J. Garcia-Vidal, E. Devaux, T. W. Ebbesen, J. R. Krenn, I. P. Radko, S. I. Bozhevolnyi, M. U. Gonzalez, J. C. Weeber, and A. Dereux, “Efficient unidirectional nanoslit couplers for surface plasmons”, *Nat. Physics* **3**, 324 (2007)

7. N. Fang, H. Lee, C. Sun, and X. Zhang, “Sub-diffraction-limited optical imaging with a silver superlens,” Science **308**, 534 (2005).

8. L. Cai, J. Zhang, W. Bai, Q. Wang, X. Wei, and G. Song, “Generation of compact radially polarized beam at 850 nm in vertical-cavity surface-emitting laser via plasmonic modulation,” *Appl. Phys. Lett.* **97**, 201101 (2010).

9. Y. Yamamoto, S. Machida, and G. Björk, “Microcavity semiconductor laser with enhanced spontaneous emission,” *Phys. Rev. A* **44**, 657 (1991).

10. A. V. Maslov and C. Z. Ning, “Size reduction of a semiconductor nanowire laser using metal coating” *Proc. SPIE* **6468**, 646801 (2007).

11. M. T. Hill, Y. -S. Oei, B. Smalbrugge, Y. Zhu, T. de Vries, P . J. van Veldhoven, F. W. M. van Otten, T. J. Eijkemans, J. P. Turkiewicz, H. de Waardt, E. J. Geluk, S. -H. Kwon, Y. -H. Lee, R. Nötzel and M. K. Smit, “Lasing metallic-coated nanocavities,” *Nat. Photonics* **1**, 589 (2007).

12. M. T. Hill, M. Marell, E. S. P. Leong, B. Smalbrugge, Y. Zhu, M. Sun, P. J. van

Veldhoven, E. J. Geluk, F. Karouta, Y. -S. Oei, R. Nötzel, C. -Z. Ning, and M. K. Smit, "Lasing in metal-insulator-metal sub-wavelength plasmonic waveguides," *Opt. Express* **17**, 11107 (2009).

13. M. P. Nezhad, A. Simic, O. Bondarenko, B. Slutsky, A. Mizrahi, L. Feng, V. Lomakin and Y. Fainman, "Room-temperature subwavelength metallo-dielectric lasers," *Nat. Photonics* **4**, 395 (2010).

14. J. H. Lee, M. Khajavikhan, A. Simic, Q. Gu, O. Bondarenko, B. Slutsky, M. P. Nezhad, and Y. Fainman, "Electrically pumped sub-wavelength metallo-dielectric pedestal pillar lasers," *Opt. Express* **19**, 21554 (2011).

15. M. Khajavikhan, A. Simic, M. Katz, J. H. Lee, B. Slutsky, A. Mizrahi, V. Lomakin, and Y. Fainman, "Thresholdless nanoscale coaxial lasers," *Nature* **482**, 204 (2012).

16. R. Perahia, T. P. Mayer Alegre. A. H. Safavi-Naeini and O. Painter, "Surface-plasmon mode hybridization in subwavelength microdisk lasers," *Appl. Phys. Lett*. **95**, 201114 (2009).

17. S. -H. Kwon, J. -H. Kang, C. Seassal, S. -K. Kim, P. Regreny, Y. -H. Lee, C. M. Lieber, and H. -G. Park, "Subwavelength plasmonic lasing from a semiconductor nanodisk with silver nanopan cavity," *Nano Lett.* **10**, 3679 (2010).

18. K. Yu, A. Lakhani, and M. C. Wu, "Subwavelength metal-optic semiconductor nanopatch lasers," *Opt. Express* **18**, 8790 (2010).

19. A. M. Lakhani, M. -K. Kim, E. K. Lau, and M. C. Wu, "Plasmonic crystal defect nanolaser," *Opt. Express* **19**, 18237 (2011).

20. C. -Y. Lu, S. -W. Chang, S. L. Chuang, T. D. Germann, and D. Bimberg, "Metal-cavity surface-emitting microlaser at room temperature," *Appl. Phys. Lett*. **96**, 251101 (2010).

21. M. J. H. Marell, B. Smalbrugge, E. J. Geluk, P. J. van Veldhoven, B. Barcones, B. Koopmans, R. Nötzel, M. K. Smit, and M. T. Hill, "Plasmonic distributed feedback lasers at telecommunication wavelengths," *Opt. Express* **19**, 15109 (2011).

22. R. F. Oulton, V. J. Sorger, T. Zentgraf, R. -M. Ma, C. Gladden, L. Dai, G. Bartal, and X. Zhang, "Plasmon lasers at deep subwavelength scale," *Nature* **461**, 629 (2009).

23. R. -M. Ma, R. F. Oulton, V. J. Sorger, G. Bartal, and X. Zhang, "Room-temperature sub-diffraction-limited plasmon laser by total internal reflection," *Nat. Mater*. **10**, 110 (2011).

24. D. J. Bergman, and M. I. Stockman, “Surface plasmon amplification by stimulated emission of radiation: quantum generation of coherent surface plasmons in nanosystems,” *Phys. Rev. Lett.* **90**, 027402 (2003).

25. M. A. Noginov, G. Zhu, A. M. Belgrave, R. Bakker, V. M. Shalaev, E. E. Narimanov, S. Stout, E. Herz, T. Suteewong and U. Wiesner, “Demonstration of a spaser-based nanolaser,” *Nature* **460**, 1110 (2009).

26. P. B. Johnson and R. W. Christy, “Optical constants of the noble metals,” *Phys. Rev. B* **6**, 4370 (1972).

27. D. B. Li and C. Z. Ning, “Peculiar features of confinement factors in a metal-semiconductor waveguide,” *Appl. Phys. Lett*. **96**, 181109 (2010).

28. Y. Liu, W. C. Ng, K. D. Choquette, and K. Hess, “Numerical investigation of self-heating effects of oxide confined vcsels,” *IEEE J. Quant. Electron*. **41**, 15 (2005).

29. E. M. Purcell, “Spontaneous emission probabilities at radio frequencies,” *Phys. Rev*. **69**, 681 (1946).

30. J. Bleuse, J. Claudon, M. Creasey, N. S. Malik, J-. M. Gérard, I. Maksymov, J-. P. Hugonin, and P. Lalanne, “Inhibition, Enhancement, and Control of Spontaneous Emissin in Photonic Nanowires,” *Phys. Rev. Lett*. **106**, 103601 (2011).

31. S. Ates, C. Gies, S. M. Ulrich, J. Wiersig, S. Reitzenstein, A. Löffler, A. Forchel, F. Jahnke, and P. Michler, “Influence of the spontaneous optical emission factor β on the first-order coherence of a semiconductor microcavity laser,” *Phys. Rev. B* **78**, 155319 (2008).

32. E. K. Lau, A. Lakhani, R. S. Tucker, and M. C. Wu, “Enhanced modulation bandwidth of nanocavity light emitting devices,” *Opt. Express* **17**, 7790 (2009).

33. T. Suhr, N. Gregersen, K. Yvind and J. Mørk, “Modulation response of nanoLEDs and nanolasers exploiting Purcell enhanced spontaneous emission,” *Opt. Express* **18**, 11230 (2010).

34. C. -Y. A. Ni and S. L. Chuang, “Theory of high-speed nanolasers and nanoLEDs,” *Opt. Express* **20**, 16450 (2012).

35. K. A. Shore, “Modulation bandwidth of metal-clad semiconductor nanolasers with cavity-enhanced spontaneous emission,” *Electron. Lett*. **46(25)**, 1688 (2010).

36. http://ab-initio.mit.edu/wiki/index.php/Dielectric_materials_in_Meep

37. B. Dold and R. Mecke, “Optische. Eigenschaften von Edelmetallen, Übergangsmetallen und deren Legierungen im Infrarot (1. Teil),” *Optik* **22**, 435 (1965).

38. P. Winsemius, H. P. Langkeek, and F. F. van Kampen, “Structure dependence of the optical properties of Cu, Ag and Au,” *Physica* **79B**, 529 (1975).

39. M. P. Nezhad, K. Tetz, and Y. Fainman, “Gain assisted propagation of surface Plasmon polaritons on planar metallic waveguides,” *Opt. Express* **12**, 4072 (2004).

40. S. A. Maier, “Gain-assisted propagation of electromagnetic energy in subwavelength surface Plasmon polariton gap waveguides,” *Opt. Communications* **258**, 295 (2006).

41. S. A. Maier, *Plasmonics Fundamental and Application*, Springer, New York 2007, Ch. 1, Page 11.

42. A. D. Rakić, A. B. Djurišić, J. M. Elazar, and M. L. Majewski, “Optical properties of metal films for vertical-cavimty optoelectronics devices,” *Appl. Optics* **37**, 5271 (1998).

43. C. A. Balanis, “Advanced Engineering Electromagnetics,” John Wiley & Son, Hoboken, NJ 1989.

44. D. B. Li and C. Z. Ning, “Giant modal gain, amplified surface plasmon-polariton, and slowing down of energy velocity in a metal-semiconductor-metal structure,” *Phys. Rev. B* **80**, 153304 (2009).

45. S. Adachi, “Optical dispersion relations for GaP, GaAs, GaSb, InP, InAs, InSb, $Al_xGa_{1-x}As$, and $In_{1-x}Ga_xAs_yP_{1-y}$,” *J. Appl. Phys.* **66 (12)**, 6030 (1989).

46. Z. I. Alferov, “The double heterostructure: concept and its application in physics electronics and technology,” Noble Lecture 2000.

47. J. C. Palais, *Fiber Optic Communications*. Prentice Hall, Englewood Cliffs, NJ 1988.

48. A. Katz ed. *Indium phosphide and related materials: processing, technology, and devices*. Artech House, Norwod, MA 1992.

49. C. Min and G. Veronis, “Theoretical investigation of fabrication-related disorders on the properties of subwavelength metal-dielectric-metal plasmonic waveguides,” *Opt. Express* **18**, 20939 (2010).

50. H. Namatsu, Y. Takahashi, K. Yamazaki, T. Yamaguchi, M. Nagase, and K. Kurihara, “Three-dimensional siloxane resist for the formation of nanopatterns with minimum linewidth fluctuations,” *J. Vac. Sci. Technol. B* **16(1)**, 69 (2010).

51. A. E. Grigorescu, M. C. van der Krogt, C. W. Hagen, and P. Kruit, "10 nm lines and spaces written in HSQ using electron beam lithography," *Microelectron. Engineering* **84**, 822 (2007).

52. B. T. Lee, T. R. Hayes, P. M. Thomas, R. Pawelek, and P. F. Sciortino, "SiO2 mask erosion and sidewall composition during CH4/H2 reactive ion etching of InGaAs/InP," *Appl. Phys. Lett.* **63**, 3170 (1993).

53. G. Beister and H. Wenzel, "Comparison of surface and bulk contributions to non-radiative currents in InGaAs/AlGaAs laser diodes," *Semicond. Sci. Technol*. **19**, 494 (2004).

54. S. Y. Hu, S. W. Corzine, K.-K. Law, D. B. Young, A.C. Gossard, L. A. Coldren and J. L. Merz, "Lateral carrier diffusion and surface recombination in InGaAs/AlGaAs quantum well ridge-waveguide lasers," *J. Appl. Phys*. **76(8)**, 4479 (1994).

55. M. Boroditsky, I. Gontijo, M. Jackson, R. Vrijen, E. Yablonovitch, T. Krauss, C. C. Cheng, A. Scherer, R. Bhat, and M. Krames, "Surface recombination measurements on III-V candidate materials for nanostructure light-emitting diodes," *J. Appl. Phys*. **87(7)**, 3497(2000).

56. J. Willamson and K. Carey, "Dopant-type selective electroless photoetching of Zn-diffused InP and InGaAs/InP heterostructures," Internal report, Instruments and Photonics Laboratory, Hewlett Packard, 1992.

57. M. J. Weber, *Handbook of optical materials*, CRC: New York 2003.

58. V. P. Drachev, U. K. Chettiar, A. V. Kildishev, H. -K. Yuan, W. Cai and V. M. Shalaev, "The Ag dielectric function in plasmonic metamaterials," *Opt. Express* **16**, 1186 (2008).

59. M. Kuttge, E. J. R. Vesseur, J. Verhoeven, H. J. Lezec, H. A. Atwater, and A. Polman, "Loss mechanisms of surface plasmon polaritons on gold probed by cathodoluminescence imaging spectroscopy," *Appl. Phys. Lett*. **93**, 113110 (2008).

60. R. Zia, M. D. Selker, P. B. Catrysse, and M. L. Brongersma, "Geometries and materials for subwavelength surface plasmon modes," *J. Opt. Soc. Am. A* **21,** 2442 (2004).

61. F. Kusunoki, T. Yotsuya, J. Takahara, and T. Kobayashi, "Propagation properties of guided waves in index-guided two-dimensional optical waveguides," *Appl. Phys. Lett.* **86,** 211101 (2005).

62. K. Tanaka, and M. Tanaka, "Simulations of nanometric optical circuits based on surface plasmon polariton gap waveguide." *Appl. Phys. Lett.* **82,** 1158 (2003).

63. N. N. Feng, M. L. Brongersma, and L. D. Negro, "Metal-dielectric slot-waveguide structures for the propagation of surface plasmon polaritons at 1.55 μm," *IEEE J. Quan. Electron.* **43**, 479-485 (2007).

64. H. T. Miyazaki and Y. Kurokawa, "Squeezing visible light waves into a 3-nm-thick and 55-nm-long plasmon cavity," *Phys. Rev. Lett.* **96**, 097401 (2006).

65. I. P. Kaminow, W. L. Mammel, and H. P. Weber, "Metal-clad optical waveguides: analytical and experimental study," *Appl. Optics* **13**, 396 (1974).

66. I. D. W. Samuel, E. B. Namdas, and G. A. Turnbull, "How to recognize lasing," *Nat. Photonics* **3**, 546 (2009).

67. B. R. Bennett, R. A. Soref, and J. A. D. Alamo, "Carrier-induced change in refractive index of InP, GaAs, and InGaAsP," *IEEE J. Quan. Electron.* **26(1)**, 113 (1990).

68. L. A. Coldren and S. W. Corzine, *Diode lasers and photonic integrated circuits* (Wiley, New York, 1995).

69. T. Baba and D. Sano, "Low-threshold lasing and Purcell effect in microdisk lasers at room temperature," *IEEE J. Sel. Top. Quan. Electron.* **9**, 1340 (2003).

70. K. Petermann, "Calculated spontaneous emission factor for double-heterostructure injection lasers with gain-induced waveguiding," *IEEE J. Quan. Electron*. **15**, 566 (1979).

71. J. C. Goodwin and B. K. Garside, "Measurement of spontaneous emission factor for injection lasers," *IEEE J. Quan. Electron.* **18**, 1264 (1982).

72. J. H. Shin, Y. G. Ju, H. E. Shin, and Y. H. Lee, "Spontaneous emission factor of oxidized vertical-cavity surface-emitting lasers from the measured below-threshold cavity loss," *Appl. Phys. Lett.* **70**, 2344 (1997).

73. M. Fujita, R. Ushigome, and T. Baba, "Large Spontaneous emission factor of 0.1 in a microdisk injection laser," *IEEE Photon. Tech. Lett.* **13**, 403 (2001).

74. H. Y. Ryu, M. Notomi, E. Kuramoti, and T. Segawa, "Large spontaneous emission factor (>0.1) in the photonic crystal monopole-mode laser," *Appl. Phys. Lett.* **84**, 1067(2004).

75. K. Ding, Z. C. Liu, L. J. Yin, M. T. Hill, M. J. H. Marell, P. J. van Veldhoven, R. Nöetzel, and C. Z. Ning, “Room-temperature continuous wave lasing in deep-subwavelength metallic cavities under electrical injection,” *Phys. Rev B* **85**, 041301(R) (2012).

76. S. Kita, K. Nozaki, and T. Baba, “Refractive index sensing utilizing a cw photonic crystal nanoalser and its array configuration,” *Opt. Express* **16**, 8174 (2008).

77. R. Chen, T. -T. D. Tran, K. W. Ng, W. S. Ko, L. C. Chuang, F. G. Sedgwick, and C. Chang-Hasnain, “Nanolasers grown on silicon,” *Nat. Photonics* **5**, 170(2010).

78. P. S. Zory, ed. *Quantum Well Lasers.* Academic Press, San Diego, CA, 1993.

79. F. Peng, B. Yao, S. Yan, W. Zhao and M. Lei, “Trapping of low-refractive-index particles with azimuthal polarized beam,” J. *Opt. Soc. Am. B* **26**, 2242 (2009).

80. Q. Zhan, “Cylindrical vector beams: from mathematical concepts to applications,” *Adv. Opt. Photon* **1**, 1 (2009).

81. R. Oron, S. Blit, N. Davidson, A. A. Friesem, Z. Bomzon, and E. Hasman, “The formation of laser beams with pure azimuthal or radial polarization,” *Appl. Phys. Lett.* **77**, 3322-3324 (2000).

82. M. P. Thirugnanasambandam, Y. Senatsky, and K. Ueda, “Generation of radially and azimuthally polarized beams in Yb:YAG laser with intra-cavity lens and birefringent crystal,” *Opt. Express* **19**, 1905 (2011).

83. T. Hirayama, Y. Kozawa, T. Nakamura and S. Sato, “Generation of a cylindrically symmetric polarized laser beam with narrow linewidth and fine tenability,” *Opt. Express* **14**, 12839-12845 (2006).

84. Z. Bomzon, G. Biener, V. Kleiner and E. Hasman, “Radially and azimuthally polarized beams generated by space-variant dielectric subwavelength gratings,” *Opt. Lett.* **27,** 285 (2002).

85. J. M. Ostermann, P. Debernardi, C. Jalics, A. Kroner, M. Feneberg, M. C. Riedl, and R. Michalzik, “Monolithic polarization control of multimode VCSELs by a dielectric surface grating,” *Proc. SPIE* **5364**, 201 (2004).

86. D. A. B. Miller, “Device requirements for optical interconnects to silicon chips,” *Proc. IEEE* **97**, 1166 (2009).

87. D. A. B. Miller, “Attojoule optoelectronics-Why and how,” IEEE Photonic Society Summer Topical Meeting Series, Waikoloa, HI, 2013.

88. K. Ding, and C. Z. Ning "Fabrication challenges of electrical injection metallic cavity semiconductor nanolasers," *Semicon. Sci. Technol*. **28**, 124002 (2013).

89. S. Matsuo, A. Shinya, C. -H. Chen, K. Nozaki, T. Sato, Y. Kawaguchi, H. Taniyama, and M. Notomi, "20-Gbit/s directly modulated photonic crystal nanocavity laser with ultra-low power comsumpation," *Opt. Express* **19**, 2242 (2011).

90. H. Altug, D. Englund, and J. Vučković, "Ultrafast photonic crystal nanocavity laser," *Nat. Physics* **2**, 484 (2006).

91. W, Chow, M. Sargent, and S. Koch, *Semiconductor-Laser Physics*, Springer, New York, 1994.

92. S. L. Chuang, *Physics of Photonic Devices*, Wiley, Hoboken, NJ, 2009.

93. A. V. Maslov, M. I. Bakunov, and C. Z. Ning, "Distribution of optical emission between guided modes and free space in a semiconductor nanowire," *J. Appl. Phys.* **99**, 024314 (2006).

94. K. Ding, L. Yin, M. T. Hill, Z. Liu, P. J. v Veldhoven, and C. Z. Ning, "An electrical injection metallic cavity nanolaser with azimuthal polarization," *Appl. Phys. Lett.* **102**, 041110(2003).

95. C. Z. Ning, "What is laser threshold?" 2013 *IEEE J. Sel. Top.Quantum Electron*. **19**, 1503604 (2013).

96. T. M. Shen, and G. P. Agrawal, "Computer simulation and noise analysis of the system performance of 1.55 μm single frequency semiconductor lasers," *J. Lightwave Tech*. **LT-5**, 653(1987).

97. C. Harder, J. Katz, S. Margalit, J. Shacham, and A. Yariv A, "Noise Equivalent circuit of a semiconductor laser diode," *IEEE J. Quant. Electron*. **18**, 333 (1982).

98. A. W. Fang, H. Park, O. Cohen, R. Jones, M. J. Paniccia, and J. E. Bowers, "Electrically pumped hybrid AlGaInAs-silicon evanescent laser," *Opt. Express* **14**, 9203 (2006).

99. Y. Halioua, A. Bazin, P. Monnier, T. J. Karle, G. Roelkens, I. Sagnes, R. Raj, and F. Raineri, "Hybrid III-V semiconductor/silicon nanolaser," *Opt. Express* **19**, 9221 (2011).

100. W. Zhou, Z. Ma, S. Chuwongin, Y. -C. Shuai, J. -H. Seo, D. Zhao, H. Yang, and W. Yang, "Semiconductor nanomembranes for integrated silicon photonics and flexible photonics," *Opt. Quant. Electron* **44**, 605 (2012).